Symmetry and asymmetry in electrocatalysis: Enhancing the electrocatalytic activity of phthalocyanines through synergy with doped graphene quantum dots

A thesis submitted in fulfilment of the requirements for the degree of

Master of Science

Of

Rhodes University

By

Reitumetse Precious Nkhahle

February 2019

Acknowledgements

"Mazithi iingqondo zethu zimbonge uYehova, kuba iinceba zaKhe zimi ngonaphakade.

Kubo bonke oothixo, akekho onjengaYe, kuba iinceba zaKhe zimi ngonaphakade.

Hosana in the highest!"

To my supervisor, Distinguished Professor Tebello Nyokong, I don't know who's responsible for giving people titles but I genuinely think that you have been robbed; you are above and beyond a distinguished professor. And although Best Distinguished or Super Distinguished Professor sounds grammatically incorrect, I think, for you Prof, it should be considered. Thank you Prof, for everything, especially for the lessons in science and the humour.

A big thank you to Dr Edward Sekhosana, Dr Gertrude Fomo, Dr John Mack and Dr Jonathan Britton. I would like to further express my gratitude to Gail, Papa Francis, labmates in S22, Marvin, Shirley and the Chemistry Department. Thank you.

To Professor Rodica-Mariana Ion and her family, Lorena Iancu and everyone else I crossed paths with at the National Research and Development Institute for Chemistry and Petrochemistry (ICECHIM), Romania, thank you for extending such great kindness to me while I was there.

My family, mom and dad, Moreheng and Thabo Nkhahle; my siblings, Thapelo, Teboho, Phetho and Lifutso, thank you for always being there and not asking me of when am I coming home.

To my friends, thank you for everything, I am grateful. I wrote your names on the cover page and changed the font colour to white because joint submissions are not allowed. Teamwork makes the dream work.

Furthermore, I would like to acknowledge the National Research Foundation (NRF) for funding.

Opinions and conclusions expressed in this work are those of the author and not the NRF.

Abstract

An exploration on the enhancement of the electrocatalytic activity of phthalocyanines (Pcs) through coupling with a series of graphene quantum dots (GQDs) is undertaken. The preliminary studies using symmetrical Pcs, a cobalt and an iron chloride tetra-substituted diethylaminophenoxy Pc (complexes **1** and **2**), for the electro-oxidation of nitrite revealed through the various sequential modifications that doped GQDs fare better than their pristine counterparts with respect to improving the electrocatalytic behaviour of Pcs, in particular, the nitrogen-doped GQDs (NGQDs).

Following up on this, a series of asymmetric Pc complexes; 2,9,16-tris-(4-*tert*-butylphenoxy) mono carboxyphenoxy phthalocyanato cobalt (II) (**3**), 2,9,16-tris-(4-*tert*-butylphenoxy) mono aminophenoxy phthalocyanato cobalt (II) (**4**), 2,9,16-tris-(3-diethylamino)phenoxy) mono carboxyphenoxy phthalocyanato cobalt (II) (**5**) and 2,9,16-tris-(3-diethylamino)phenoxy) mono aminophenoxy phthalocyanato cobalt (II) (**6**) was prepared in which push-pull systems were compared to other asymmetric complexes that lack this effect towards the electrocatalytic sensing of hydrazine. All asymmetric complexes (**3**-**6**) were π-stacked to the NGQDs while those with an NH_2 group (**4** and **6**), were also covalently linked to the NGQDs. These complexes and their corresponding conjugates were characterized accordingly and applied as electrocatalysts in the oxidation of hydrazine. The electrochemical studies revealed that π-π stacking yields better responses (higher sensitivities and lower limits of detection) than covalent linking because there are less forces acting on the graphene network. Covalent linking introduces both tensile and compressive forces which in turn results in an increase in the I_D/I_G ratio and that is unfavourable for electrocatalysis.

In comparing the electrodes composed of the π-stacked conjugates to those altered through sequential modifications, despite the conditions not being the same, it can be inferred that the magnitude of the electrostatic forces between the Pcs and the GQDs also plays a significant role in electrocatalysis. The π-stacked conjugates, owing to the manner in which they were prepared, have stronger electrostatic forces acting between the Pc and GQDs hence they were able to elicit a better electrochemical response than the sequentially modified electrodes. In addition to that, it appears that asymmetric Pcs are better electrocatalysts in comparison to the symmetric Pcs.

Table of contents

List of symbols

α	Alpha/ peripheral
ΔE_p	Anodic to cathodic peak potential separation
β	Beta/ non-peripheral
k	Catalytic rate constant
C	Concentration
I	Current
e^-	Electron
ε	Molar extinction coefficient
n	Number of replicates
I_p	Peak current
E_p	Peak potential
π	Pi
t	Time
λ	Wavelength

List of abbreviations

CCE	Carbon ceramic electrode
CNTs	Carbon nanotubes
CV	Cyclic voltammetry
DBU	1,8-Diazabicyclo[5.4.0]undec-7-ene
DMF	Dimethylformamide
DSSC	Dye-sensitized solar cell
DLS	Dynamic light scattering
EDC	1-Ethyl-3-(3-dimethylaminopropyl)-carbodiimide
FT-IR	Fourier transform-infrared
GCE	Glassy carbon electrode
GQDs	Graphene quantum dots
GSH	Glutathione
GSHGQDs	Glutathione-doped graphene quantum dots
HOMO	Highest occupied molecular orbital
LoD	Limit of detection
LUMO	Lowest unoccupied molecular orbital
MALDI-TOF	Matrix assisted laser-desorption/ionization-time of flight
Nd:YAG	Neodymium-doped yttrium aluminum garnet
NCNF	Nitrogen-doped carbon nanofibers
NGQDs	Nitrogen-doped graphene quantum dots
NHS	N-hydroxysuccinimide
NLO	Nonlinear optics
NMR	Nuclear magnetic resonance
ORR	Oxygen reduction reaction
PACT	Photo-antimicrobial chemotherapy
PDT	Photodynamic therapy
PL	Photoluminescence
Pc(s)	Phthalocyanine(s)
Redox	Reduction/oxidation
rBDGONs	Reduced boron-doped GONs

rGNs	Reduced graphene nanosheets
rNDGONs	Reduced nitrogen-doped GONs
rGONs	Reduced graphene oxide nanosheets
rPNDGONs	Reduced phosphorus and nitrogen doped GONs
rPDGONs	Reduced phosphorus-doped GONs
rGQDs	Reduced graphene quantum dots
S. C. E.	Saturated calomel electrode
SWCNTs	Single-walled carbon nanotubes
TEM	Transmission electron microscopy
UV-vis	Ultraviolet-visible
MWCNTs	Multi-walled carbon nanotubes
XRD	X-ray diffraction
XPS	X-ray photoelectron spectroscopy

Chapter 1

Introduction

This chapter provides a brief account of the literature pertaining to phthalocyanines, graphene quantum dots, combinations of the two and some of their applications in electrocatalysis.

Problem statement

Numerous sensors based on a number of different materials have been employed in the detection of nitrite and hydrazine. While these two entities are of great use in industrial processes, they also pose a risk to human and animal life once they exceed a certain quantity. Much of the techniques used consist of both historical and modern technologies with electrochemistry being one of the most favoured.

Electrochemical sensors for nitrite and hydrazine already exist however a large number of them are plagued by the fact that they are based on bulk machinery such as screen printed electrodes or they are expensive to manufacture on a large scale once they have been miniaturized. Before one even considers bulk manufacturing of electrochemical sensors such as the screen-printed electrodes, the materials that are to be used need to possess both physical and chemical stability all while being economically viable. In an attempt to provide some direction as to where the design of electrodes should be heading before bulk manufacturing is considered, in this work, an exploration on phthalocyanines in the presence of highly conductive carbon-based materials is undertaken.

1.1 Electrocatalysis

Electrocatalysis is the combination of both electrochemistry and catalysis [**1**]. Electrochemical sensing is a form of electrocatalysis in which the catalytic processes that are permitted are those based on electrochemical principles, namely oxidation and reduction [**2**]. It is based on a device's ability to convert the interaction between an electrode and the analyte into a quantitative signal [**3**]. Electrocatalysis is characterized by an increase in the catalytic current and a reduction of the potential following electrode modification. An example of this is illustrated in **Fig. 1.1** where a bare electrode is compared to a modified electrode [**4**].

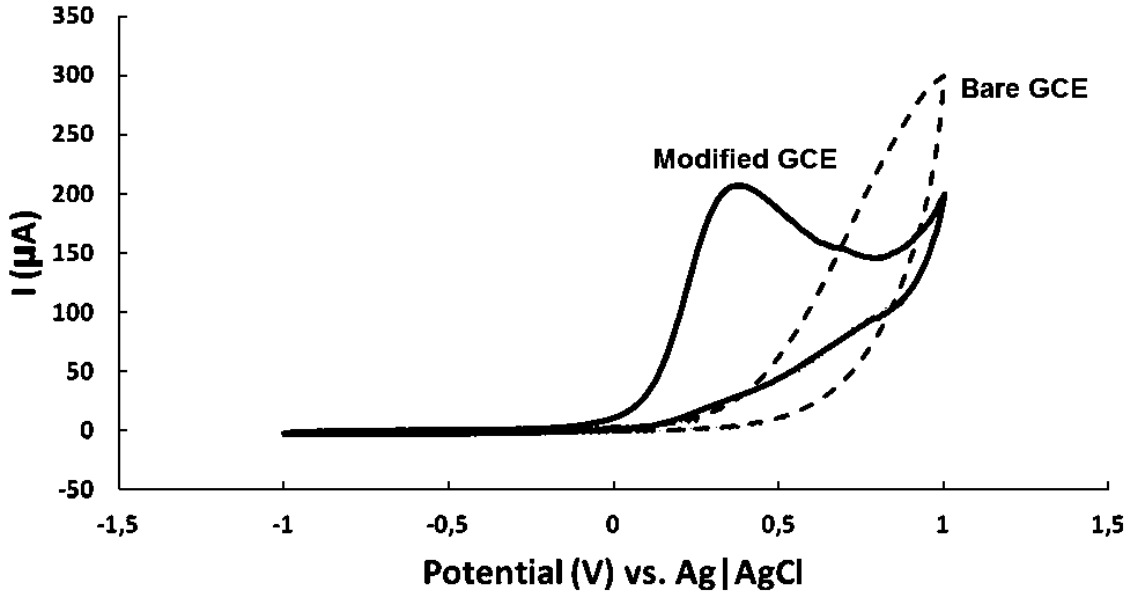

Fig. 1.1: Cyclic voltammograms for a bare GCE (dashed line) and a modified GCE (solid line) in 0.2 M NaOH containing 6 mM of hydrazine [**4**].

The general set-up for most electrochemical experiments consists of a working electrode, a reference electrode, a counter electrode, a glass cell, a potentiostat and a monitor with the working electrode being the most important (**Fig. 1.2**) [**5, 6**]. The working electrode is that which can be modified with the applicable material as it is the one that interacts with the analyte [**7**]. Working electrodes differ as they can be fabricated in various ways from noble metals such as gold and platinum to carbon-based materials [**7**]. And while some electrodes

can detect certain materials in their bare state, modification with nanomaterials and biological systems has often produced improved results in terms of lowered limits of detection and higher catalytic rates [**8-11**]. The selection criterion for working electrodes is based largely on their ability to facilitate the swift movement of electrons whilst maintaining both chemical and physical stability [**12**]. In addition to these traits, they need to possess a low noise-to-signal ratio and to some extent, provide a repeatable response [**7**].

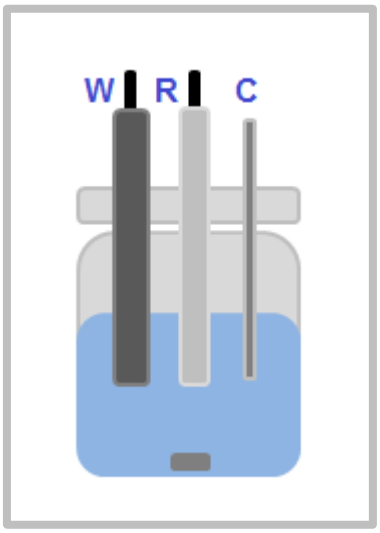

Fig. 1.2: General electrochemical cell composed of a working (**W**), reference (**R**) and a counter (**C**) electrode.

In this thesis, a glassy carbon electrode was used as a support for the electrocatalysts. The glassy carbon electrode belongs to the family of carbonaceous electrodes and unlike its carbon-based counterpart, the graphite electrode; it is not porous [**13**]. This is of great importance because the electrochemical results obtained from such an electrode are to a large extent, reproducible [**13, 14**]. In addition to being isotropic and displaying a wide potential window (-0.8 to +1.4 V vs *S.C.E.* (saturated calomel electrode)), the glassy carbon electrode is highly conductive, chemically inactive and impenetrable by gases and fluids [**13, 14**].

The manner in which electrode modification is achieved is dependent on the electrocatalyst and how it may possibly interact with the analyte and also on the type of electrode. The

most common methods of modification include adsorption, electropolymerization, and electrografting and click chemistry [**15-18**].

Despite the various methods of modification that are available, adsorption through drop-drying was the method selected for the modification of the glassy carbon electrode as it is the least complicated. This method involves the dissolution of the catalyst in the appropriate solvent and either dropping a small quantity of the solution onto the electrode surface and drying it or immersing the electrode into the solution for a short period of time and then drying it [**15**]. Along with the simplicity associated with drop-drying, the reason for choosing adsorption over the other methods is that the materials used as probes in this work are carbon-based materials and the assumption that was made is that their ability to adhere to the carbon electrode would be further stimulated by their highly conjugated systems. This method of electrode modification is fairly reproducible when using more sensitive techniques such as chronoamperometry. For less sensitive techniques such as cyclic voltammetry, much of the limitations in terms of reproducibility are witnessed through the decline in the Faradaic currents which are often the result of the electrode surface being oxidized through continuous usage.

Much of the materials that are designed for electrochemical sensing are made with their chemical and physical stability as well as ease of preparation in mind [**19**]. As a result of this, many electrode modifiers respond to a wide range of analytes. Across all possible analytes, both organic and inorganic, a high sensitivity is desirable as it is often accompanied by low limits of detection [**19, 20**]. For this particular set of work, the materials employed for sensing were electron-rich molecules, phthalocyanines and graphene quantum dots.

1.2 Phthalocyanines

1.2.1 Overview (Structure and general applications)

Phthalocyanines (Pcs) are synthetic dyes defined by their highly conjugated 18 π-electron system [**21, 22**]. As porphyrin analogues, they too have a rigid structure with much of the flexibility espoused by the dyes being due to modification on the alpha (α) and beta (β) positions as well as through the insertion of a metal or metalloid in the Pc cavity (**Fig. 1.3**)

[**21-24**]. Further modifications can be made through axial ligation provided that that is permitted by the central metal (**Fig. 1.3**) [**25, 26**].

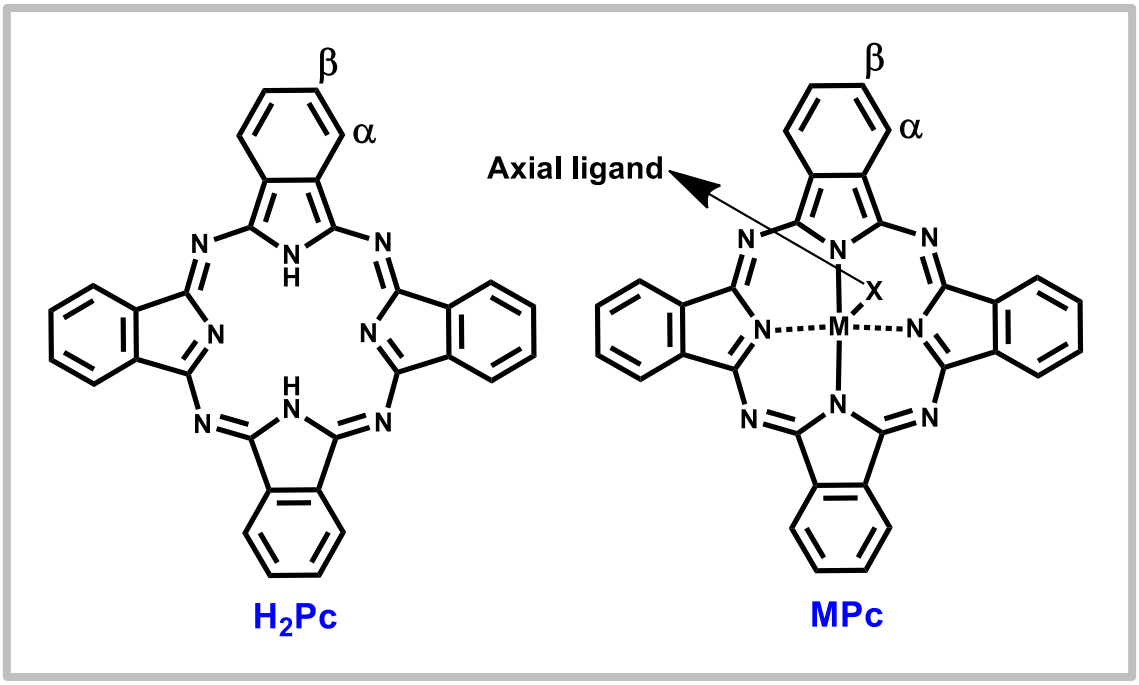

Fig. 1.3: General structure of an unmetallated Pc (H_2Pc) and a metallated Pc (MPc) with an axial ligand (where α represents the non-peripheral end, β the peripheral end, M the metal and X the axial ligand).

Much of the properties exhibited by Pcs are often discussed with respect to their original uses and that is in the textile industry [**27**]. A large majority of these greenish-blue substances are insoluble in water and exhibit different solubilities in different organic solvents. This is largely dependent on the central metal as well as the substituents on the peripheral (β) and/or non-peripheral (α) ends [**21, 27**]. In addition to either enhancing or weakening the solubility, substitution and the choice in central metal have a great impact on both the optical and electronic properties of these macrocycles [**21**]. The ability to modulate the Pcs' optoelectronic properties has opened up their uses to other fields outside of the textile industry. The advancement of their use in other fields is further supported by the fact that they are thermally stable and are not easily oxidized or reduced [**21, 22, 27**].

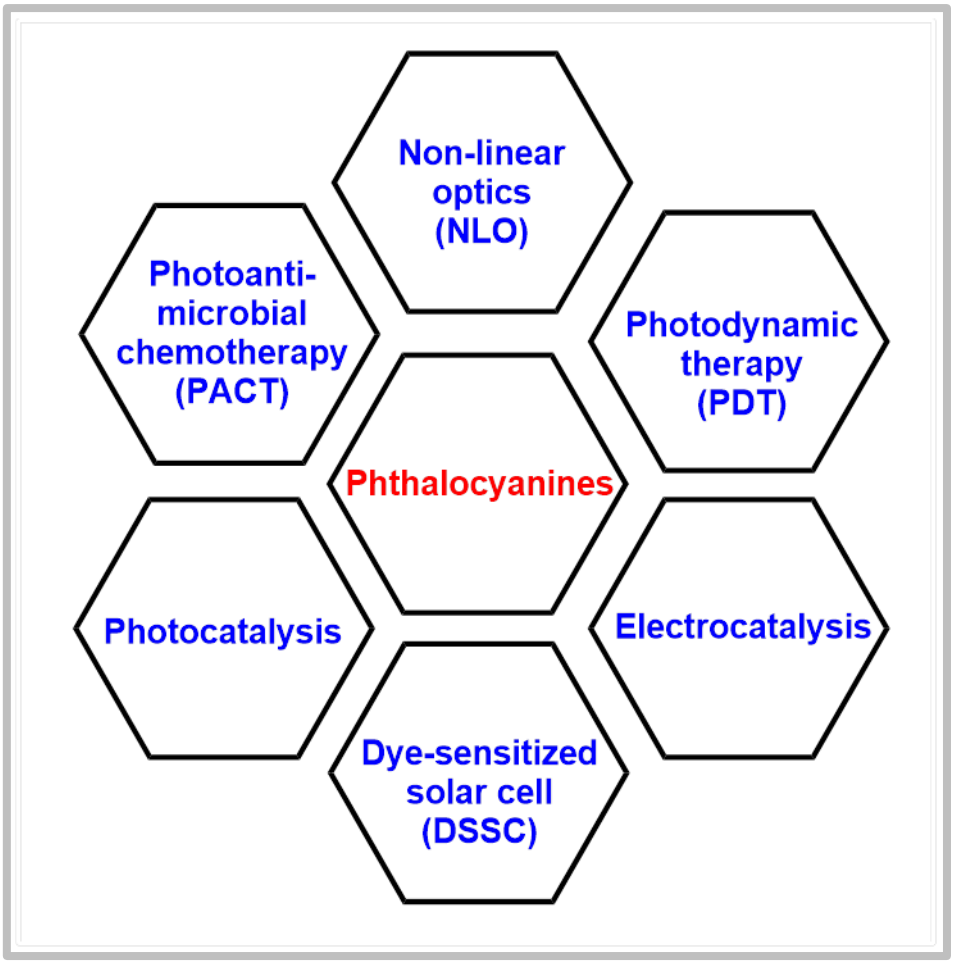

Fig. 1.4: An illustration of some phthalocyanine-based applications.

In the last few decades, phthalocyanines have been applied in various fields of science including medicine where they are used as photosensitizers in photodynamic therapy, in the energy sector for the creation of solar cells and light-emitting diodes, as sensors and in the fabrication of optical limiting material amongst others (**Fig. 1.4**) [**28-31**]. Much of these applications are based on the ability of these molecules to act as conductors or semiconductors [**22**]. In this particular set of work, Pcs are used as electrode modifiers for the electrocatalytic oxidation of hydrazine and nitrite.

1.2.2 Synthesis

The synthesis of Pcs was first reported in 1907 and since then, the search for cost-effective methods such as using accessible materials and reducing reaction times and temperatures whilst increasing yields has been an ongoing process to date [**32**]. And while great feats have

been achieved in terms of establishing various approaches towards the synthesis of symmetrical Pcs, the synthesis of asymmetrical Pcs and obtaining high yields remains a challenge.

1.2.2.1 Symmetrical phthalocyanines (tetra-substituted Pcs)

The general preparation of a phthalocyanine entails the use of a phthalonitrile, a solvent with a high boiling point, a metal and base that serves as a catalyst [**33**]. Other common Pc synthesis precursors include phthalic acid, variations thereof and *o*-disubstituted benzene derivatives (**Scheme 1.1**) [**33-35**].

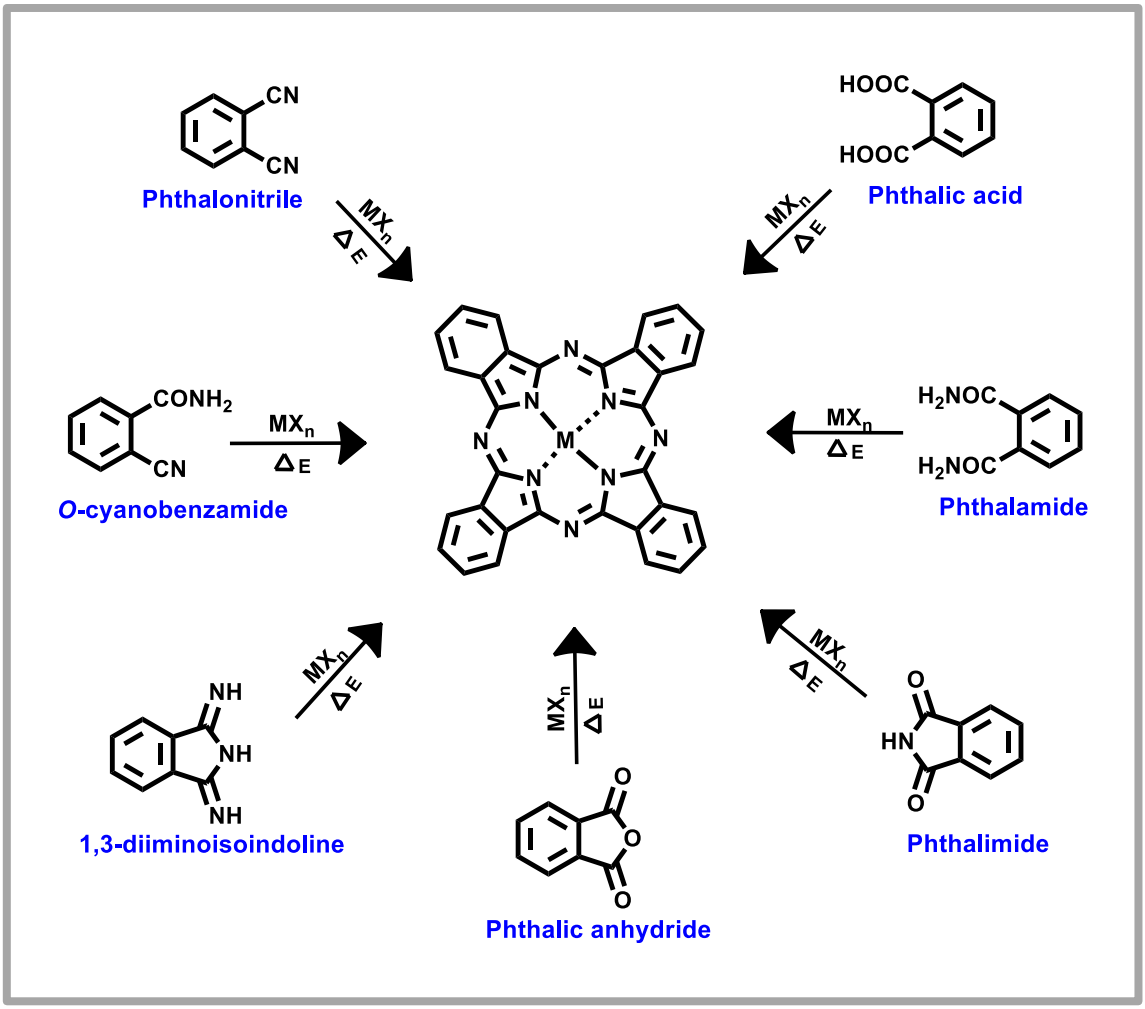

Scheme 1.1: An illustration of how a phthalocyanine can be synthesized from different precursors where M in MX_n represents the metal and X the complementary ion (e.g. Cl^-, CH_3COO^-, OH^-, etc.) and n the number of X ions which informs the oxidation state of the metal in the salt.

Tetra-substituted Pcs are derived from substituted phthalonitriles and the synthesis thereof can result in the formation of regioisomers that are difficult to separate (**Scheme 1.2**) [**21, 36, 37**]. In addition to the regioisomers enforced by the substituents, the size or absence of the metal can also have an influence on the symmetry of the molecule [**38, 39**]. Larger metals tend to result in a reduction of the symmetry as they are not in the same plane as the rest of the molecule (**Fig. 1.5**). This is seen in **Fig. 1.5** where the molecule with a C_{4v} symmetry has the metal situated outside of the Pc cavity whilst that with a D_{4h} symmetry has the metal located in the same plane as the rest of the molecule.

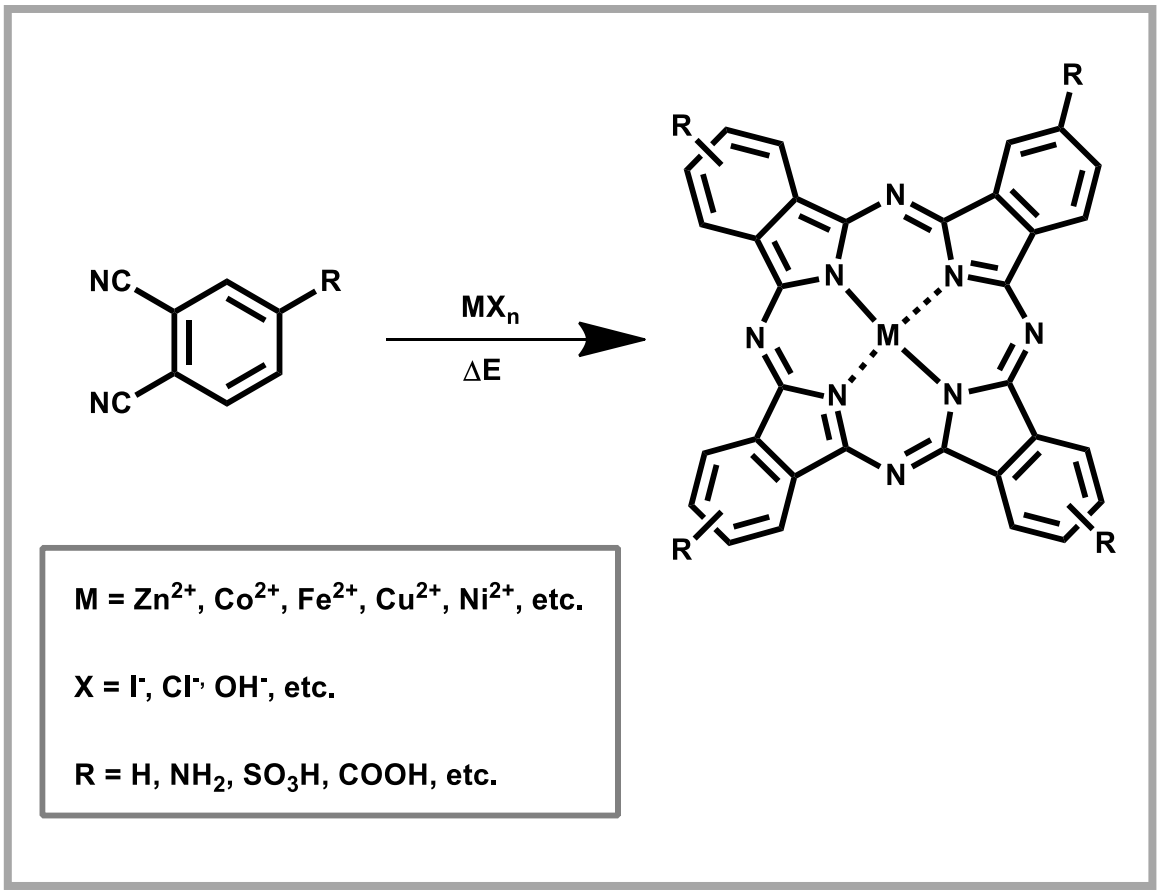

Scheme 1.2: The general synthetic route for tetra-substituted phthalocyanines resulting in various symmetries being adopted by the molecules.

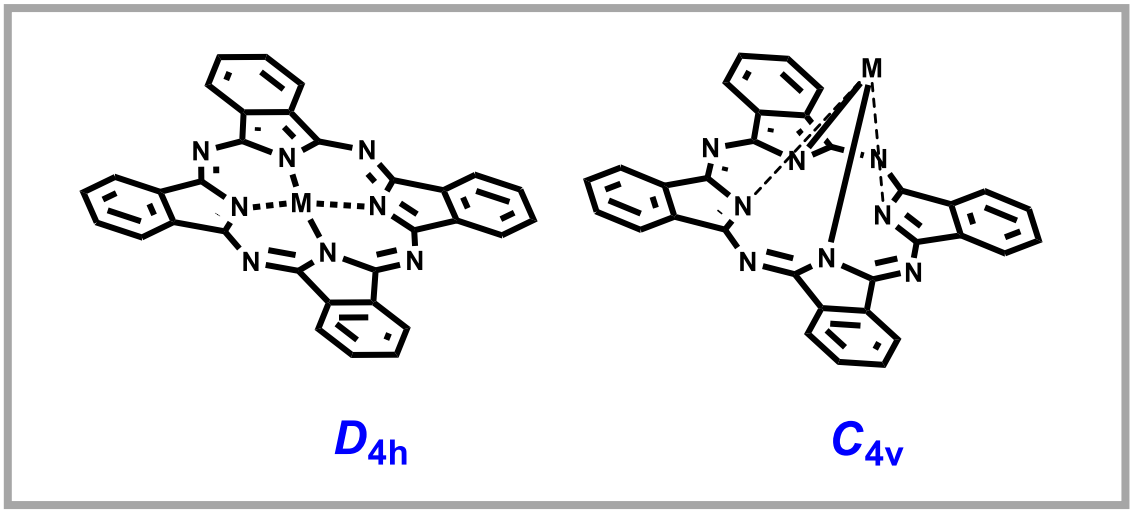

Fig. 1.5: An illustration of the different symmetries assumed by substituted Pcs.

1.2.2.2 Asymmetrical phthalocyanines (A_3B-type Pcs)

The synthesis of asymmetric Pcs is similar to that of the symmetrical Pcs in that there is a metal salt, a high boiling point solvent and a base [**33, 34**]. The difference between the two is that lower symmetry Pcs make use of two different phthalonitriles that are rationed in such a way that the production of the desired compound is maximised (**Scheme 1.3**). The most common method of synthesizing asymmetrical Pcs is the statistical condensation approach [**40**]. The optimal ratio is said to be 1:3 as this limits the production of the tetra-substituted analogue. Higher ratios such as 1:9 and 1:20 have also been reported however in this particular set of work, a 1:3 ratio served as the ideal choice. Like the symmetrical Pcs, the asymmetric synthesis is accompanied by other products which often stifle the yield of the expected product (**Scheme 1.3**) [**40**]. As illustrated in **Scheme 1.3**, at least six possible compounds can be extracted from one reaction where the desired A_3B or B_3A-type Pcs can be separated from the others through extensive chromatography. Other methods of synthesizing asymmetrical A_3B-type Pcs include that of using a sub-phthalocyanine and the polymer-support route [**40**].

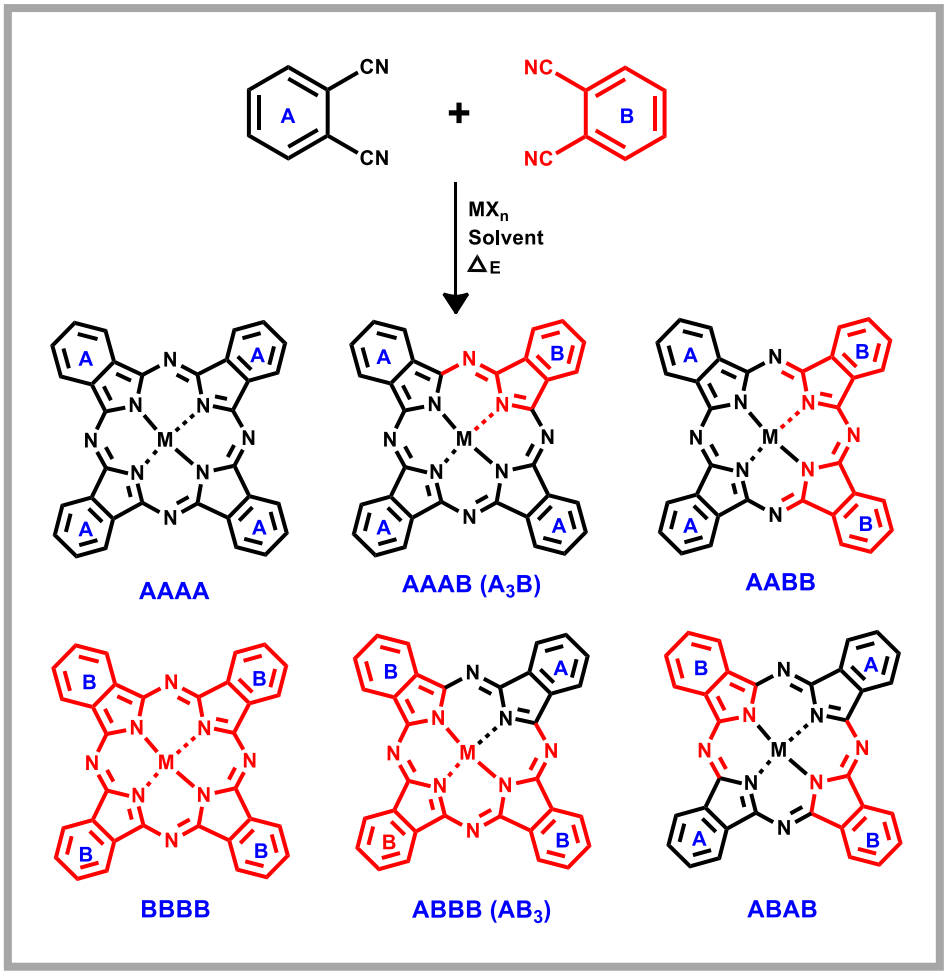

Scheme 1.3: An illustration of how asymmetrical Pcs are synthesized and the possible side-products where M in MX_n represents the metal and X the complementary ion (e.g. Cl^-, CH_3COO^-, OH^-, etc.) and n the number of X ions which informs the oxidation state of the metal in the salt.

1.2.3 Electronic spectra of phthalocyanines

The electronic absorption spectra of Pcs is characterised by a strong absorption of the Q-band (**Fig. 1.6**). The Q-band is located between 650 nm and 670 nm however; modifications on the alpha or beta positions as well as conjugation to other molecules can induce either bathochromic (blue) or hypsochromic (red) shifts (**Fig. 1.6**) [**41-43**]. In addition to altering the symmetry, the central metal's size and oxidation state can induce shifts to higher or lower wavelengths [**22**].

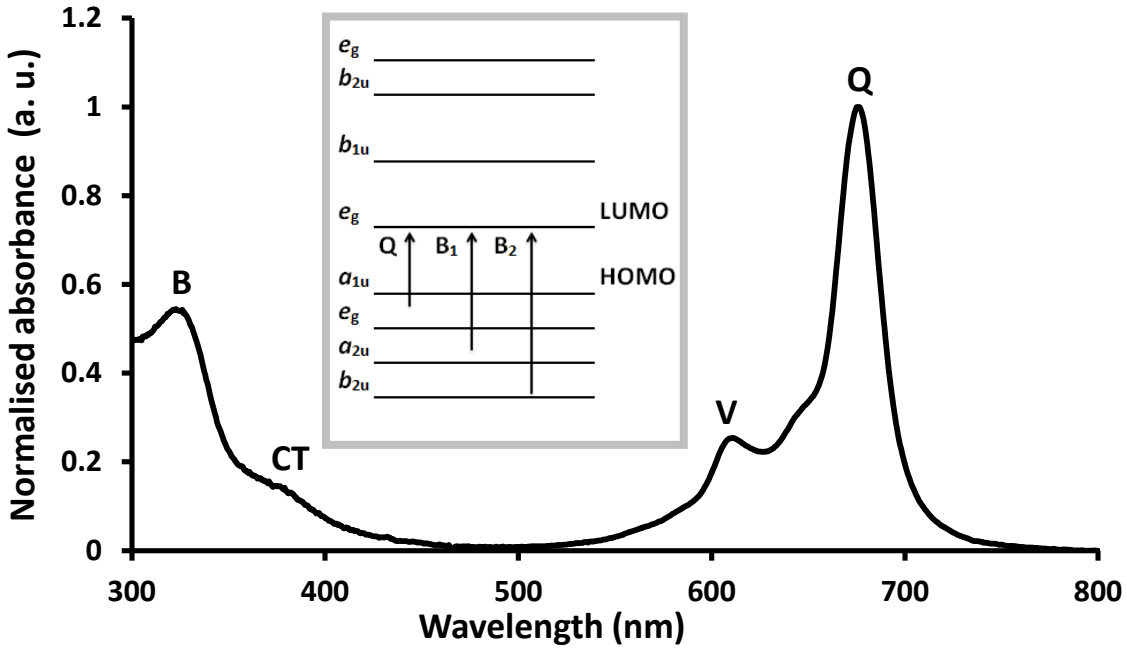

Fig. 1.6: Absorption spectra of a tetra-substituted diethylamino-phenoxy cobalt Pc in DMF where **B** is the B-band, **CT** the charge transfer band, **V** the vibronic band and **Q**, the Q-band.

The electronic spectrum of Pcs has been explained using Gouterman's four orbital model where the transitions responsible for the Q-band and the B-band are expressed pictorially in **Fig. 1.6** (Inset). The Q-band is the result of an $a_{1u} \rightarrow e_g$ transition while the B-bands are from b_{2u} and a_{2u} to e_g, which are all $\pi \rightarrow \pi^*$ transitions that occur within the benzene ring system (**Fig. 1.6 (**Inset**)**) [**44-46**]. Owing to the proximity of the energy levels in which the electronic transitions occur, sometimes there is an overlap in the B-bands hence only one broad B-band is observed (**Fig. 1.6**). In the case where the central metal is a transition metal, it may happen that the *d* orbitals of the metal reside in between the highest occupied molecular orbital (HOMO) and the lowest unoccupied molecular orbital (LUMO) of the Pc resulting in a metal to ligand or ligand to metal charge transfer, resulting in a charge transfer band in the absorption spectrum (**Fig. 1.6**) [**47-49**].

1.2.4 Electrochemistry of phthalocyanines

The conductive nature of some of these molecules has been studied extensively over the years using electrochemical techniques such as cyclic voltammetry and differential pulse voltammetry (**Fig. 1.7**) [**35, 50**]. Pcs undergo both oxidation and reduction processes and

depending on the structure as well as the central metal, each process can be assigned to a certain part of the molecule, the metal itself, the ring system or the substituents if there are any [**50, 51**].

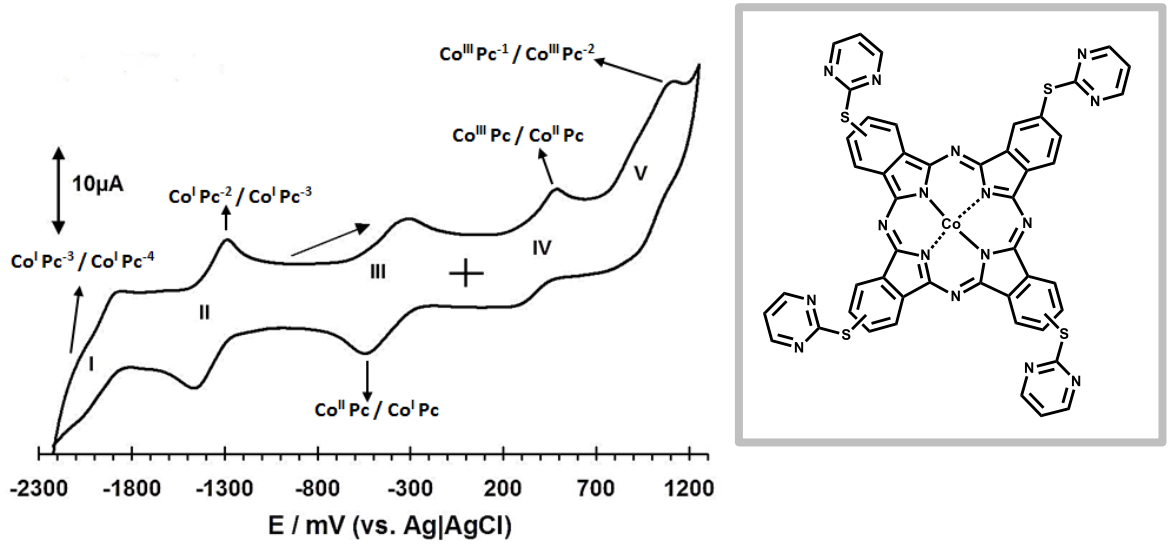

Fig. 1.7: A cyclic voltammogram of a tetramercaptopyrimidine cobalt Pc in DMF containing 0.1 M $TBABF_4$ with the structure of the Pc presented on the right-hand side [**50**].

Fig. 1.7 is an example of the electrochemical characterization of a tetra-substituted cobalt Pc. Pcs are capable of undergoing at least 6 redox processes attributed to the ring system alone with four electrons contributing to the reduction (4 electrons added to the e_g orbital) and two participating in the oxidation (2 electrons removed from the a_{1u} orbital) (**Fig. 1.6 (**Inset**)**) [**52**]. In most cases regarding metallated Pcs that contain electrochemically active central metals, oxidation of the central metal is often observed at lower potentials in comparison to those of the ring [**53**]. Other factors that may influence the redox behaviour of Pcs include the type of substituents employed, the oxidation state of the central metal as well as the solvent in which the Pc has been dissolved [**54**].

1.2.5 Phthalocyanines in electrocatalysis

The electrocatalysis of various organic and inorganic materials using Pcs is an area of research that is continuously expanding. Phthalocyanines bearing different central metals and substituents have been used in sensing a wide variety of analytes [**55-65**]. **Table 1.1** [**66-78**] provides a brief summary of the literature regarding the use of Pcs in conjunction with various carbon-based materials for electrochemical sensing and/or other electrochemical processes. **Fig. 1.8** provides a general illustration of a Pc with the point of attachment to the Pc ring highlighted on the substituent.

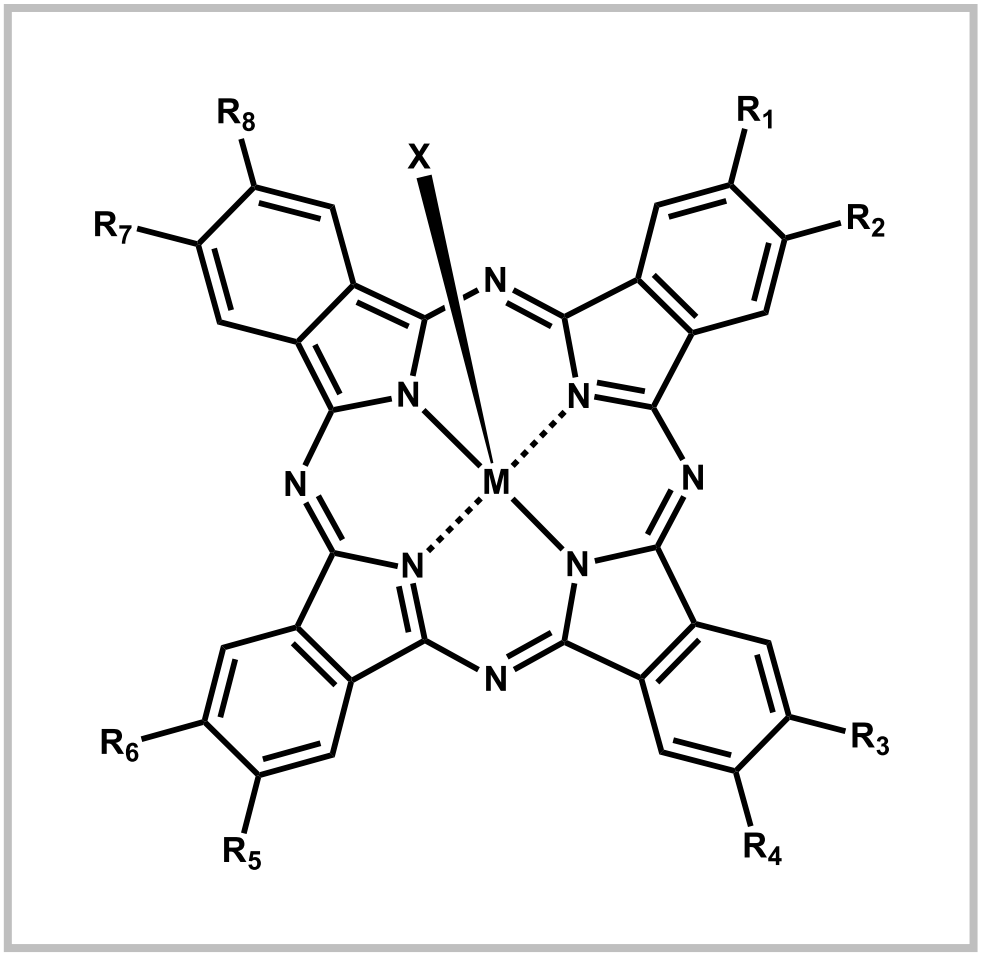

Fig. 1.8: General illustration of a Pc where R represents the substituent, M the metal and X the axial ligand.

Table 1.1: Phthalocyanines coupled with carbon-based nanomaterials for electrochemical sensing.

Pc substituents, central metal and axial ligand	**Pc/nanomaterial interaction**	**Analyte or process**	**Ref.**
M = Fe(III) X = NH_2GQDs $R_1 = R_2 = R_3 = R_4 = R_5 = R_6 = R_7 = R_8$ = H (*Unsubstituted*)	Covalent linking to NH_2GQDs	ORR	[**66**]
M = Co(II) $R_1 = R_2 = R_3 = R_4 = R_5 = R_6 = R_7 = R_8$ = H (*Unsubstituted*)	π-π stacking with Graphene	Dopamine and ascorbic acid	[**67**]
M = Co(II) $R_1 = R_2 = R_3 = R_4 = R_5 = R_6 = R_7 = R_8$ = H (*Unsubstituted*)	Mixing with SWCNTs	Hydrazine	[**68**]
M = Co(II) $R_1 = R_2 = R_3 = R_4 = R_5 = R_6 = R_7 = R_8$ = H (*Unsubstituted*)	Mixing with graphene	Glucose	[**69**]
M = Fe(II) $R_1 = R_2 = R_3 = R_4 = R_5 = R_6 = R_7 = R_8$ = H (*Unsubstituted*)	Sequential modification with CNTs	Glucose	[**70**]
M = Co(II) $R_1 = R_2 = R_3 = R_4 = R_5 = R_6 = R_7 = R_8$ = H (*Unsubstituted*)	π-π stacking to nitrogen-doped graphene	L-cysteine L-glutathione 2-mercaptoethanol	[**71**]
M = Co(II) $R_1 = R_3 = R_5 = R_7$ =H $R_2 = R_4 = R_6 = R_8 = NH_2$ (*Tetra-substituted*)	Sequential modification with MWCNTs and rGNs	Paraguat	[**72**]
M = Co(II), Fe(II) $R_1 = R_2 = R_3 = R_4 = R_5 = R_6 = R_7 = R_8$ =			

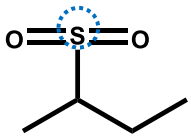 (*Octa-substituted*)	Sequential modification with MWCNTs	ORR	[**73**]
M = Co(II) $R_1 = R_3 = R_5 = R_7 = H$ $R_2 = R_4 = R_6 = R_8 =$ 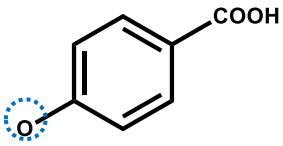 (*Tetra-substituted*)	π-π stacking to GQDs	Hydrazine	[**74**]
M = Co(II) $R_1 =$ 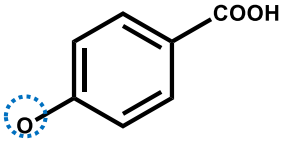 $R_2 = R_3 = R_4 = R_5 = R_6 = R_7 =$ $R_8 = H$ (*Mono-substituted*)	π-π stacking to GQDs	Hydrazine	[**74**]
M = Co(II) $R_1 = R_3 = R_5 = R_7 = H$ $R_2 =$ 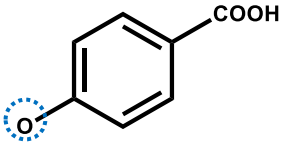 $R_4 = R_6 = R_8 =$ 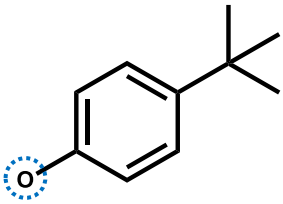 (*A_3B tetra-substituted*)	Covalent linking and π-π stacking with NH_2GQDs and reduced GQDs	Hydrazine	[**75**]

M = Co(II) $R_1 = R_3 = R_5 = R_7 = H$ $R_2 = R_4 = R_6 = R_8 =$ 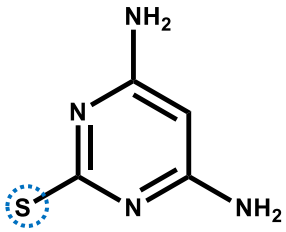 (*Tetra-substituted*)	Covalent linking and mixing with MWCNTs	L-cysteine	[**76**]
M = Co(II) $R_1 = R_3 = R_5 = R_7 = H$ $R_2 = R_4 = R_6 = R_8 =$ 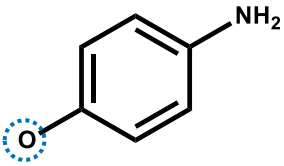 (*Pc nanoparticle*)	Sequential modification with rGONs, rBDGONs, rNDGONs, rPNDGONs, rPDGONs	Hydrogen peroxide	[**77, 78**]

ORR – oxygen reduction reaction; SWCNTs – single-walled carbon nanotubes; CNTs – carbon nanotubes; MWCNTs – multi-walled carbon nanotubes; rGNs – reduced graphene nanosheets; rGONS – reduced graphene oxide nanosheets; rBDGONs – reduced boron-doped GONs; rNDGONS – reduced nitrogen-doped GONs; rPNDGONs – reduced phosphorus and nitrogen doped GONs; rPDGONS – reduced phosphorus-doped GONs.

Various approaches using Pcs have been adopted in the inclusion of carbon nanomaterials in electrochemical sensing as expressed in **Table 1.1** with the complexity of the systems varying based on the desired outcome. Quite often, the Pcs employed are those that are commercially available [**66-71**], especially unsubstituted Pcs. Substituted Pcs are appealing as substituents not only facilitate the formation of covalent bonds but they can also enhance the general functioning of the electrocatalyst [**72-78**].

As showcased in **Table 1.1**, with the exception of two [**74, 75**], no asymmetric Pcs have been applied in conjunction with GQDs hence they are the subject of this thesis. According to literature, asymmetry improves the photophysical and chemical properties of Pcs and more so as they enable the formation of controlled conjugates with other materials through covalent linkages [**79-81**]. In this work, the electrocatalytic activities of symmetrical and asymmetrical Pcs are investigated for the first time using doped GQDs.

1.2.6 Phthalocyanines used in this work

GQDs have been paired with tetra-substituted Pcs for optical sensing [**82, 83**] while a push-pull phthalocyanine-based system has been applied in electrochemical sensing (**Table 1.1**) [**75**]. **Table 1.1** shows that very little has been done regarding push-pull systems and their use in the presence of doped GQDs in electrocatalysis.

Table 1.2: Pcs used in this work and how they were coupled with the GQDs.

Complex structure	Complex name	GQDs	Studies
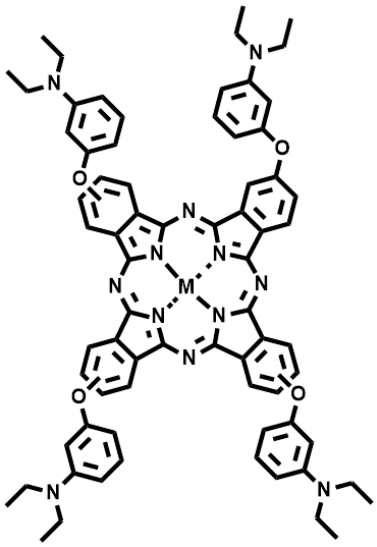	2,9,16,23-*tetrakis*-(3-(diethylamino)phenoxy) phthalocyaninato cobalt(II) (1) [**84**] And iron(III) chloride (2) (**New**)	Sequential modifications on the electrode with the following: • Pristine GQDs (GQDS) • Nitrogen-doped GQDs (NGQDs) • Glutathione-doped GQDs (GSHGQDs)	Electro-oxidation of nitrite
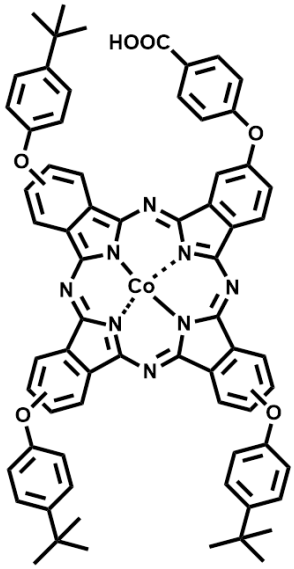	2,9,16-*tris*-(p-*tert*-butylphenoxy) mono carboxyphenoxy phthalocyaninato cobalt (II) (3) [**75**]	π-π stacking with: NGQDs	Electro-oxidation of hydrazine

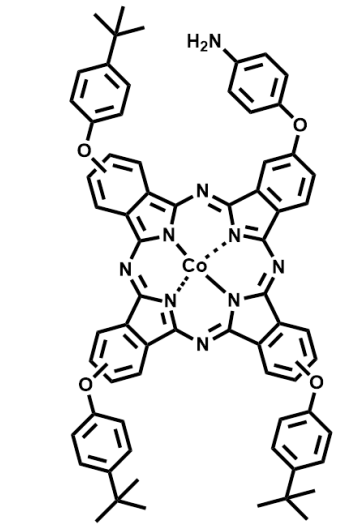	2,9,16-*tris*-(p-*tert*-butylphenoxy) mono aminophenoxy phthalocyaninato cobalt (II) (**4**) (**New**)	π-π stacking and covalent linking with: NGQDs	Electro-oxidation of hydrazine
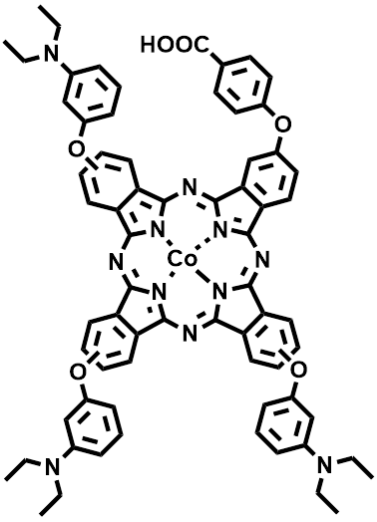	2,9,16-*tris*-(3-diethylamino)phenoxy) mono carboxyphenoxy phthalocyaninato cobalt (II) (**5**) (**New**)	π-π stacking with: NGQDs	Electro-oxidation of hydrazine
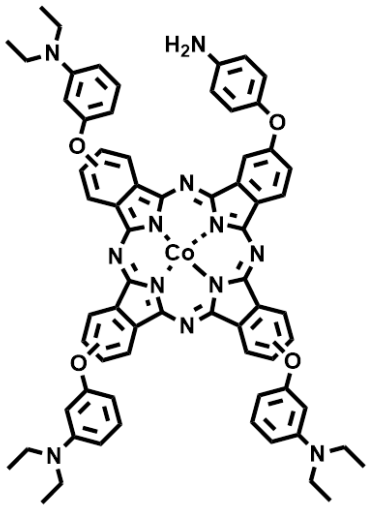	2,9,16-*tris*-(3-diethylamino)phenoxy) mono aminophenoxy phthalocyaninato cobalt (II) (**6**) (**New**)	π-π stacking and covalent linking with: NGQDs	Electro-oxidation of hydrazine

The same can be inferred for the symmetrical Pcs as **Table 1.1** consists largely of unsubstituted Pcs. This has prompted a search into designing new push-pull systems and combining them with doped GQDs. **Table 1.2** shows all the Pcs that were used in this work and how they were applied in conjunction with the GQDs for the electrocatalysis of nitrite and hydrazine.

All the Pcs that were made use of in this work (to be referred to using their assigned number from this point forward) bear bulky substituents in an attempt to reduce the likelihood of the Pc monomers forming aggregates in solution [**85, 86**]. Complexes **1** and **2** where used in the electrocatalytic oxidation of nitrite in which the activity of the central metals in the presence of the GQDs was of interest. Iron and cobalt Pcs are the most favourable central metals in electrocatalysis as witnessed in **Table 1.1** [**66-78, 87-96**]. As a preliminary study, complex **1** was investigated further in the presence of pristine, nitrogen-doped and glutathione-doped GQDs while complex **2** was only studied in the presence of the nitrogen-doped GQDs following the results obtained from the work conducted using complex **1**. Complexes **3**-**6** are all asymmetrical Pcs with **3** and **5** being push-pull systems and **4** and **5** bearing a primary amine group to enable covalent linking with the GQDs through the formation of an amide bond. These complexes (**3-6**), in conjunction with nitrogen-doped GQDs (NGQDs), were used in the electro-oxidation of hydrazine. Complex **3** has been applied before for the same study however, the nature of the GQDs employed differs in that they were functionalized with NH_2 meaning there was little to no pyridinic nitrogen atoms [**75**]. Complexes **3** and **5** were studied in an attempt to establish the best-performing push-pull system in response to the oxidation of hydrazine; independently and in the presence of NGQDs through π-π stacking. Complexes **4** and **6** were also studied comparing the predominant substituents, the *tert*-butylphenoxy and the diethylaminophenoxy groups. In addition to the Pcs alone, both the π-stacked and covalently linked conjugates of each (**4** and **6**) were studied. The symmetrical Pcs were used in the electro-oxidation of nitrite while the asymmetrical Pcs were applied for hydrazine.

1.3 Graphene quantum dots (GQDs)

1.3.1 Overview

Graphene is a highly ordered carbon framework composed of sp^2 hybridized carbon atoms [**97**]. Since its discovery through isolation from pyrolytic graphite, research pertaining to this material has ballooned significantly over the years especially in physics, material science and chemistry [**98, 99**]. While graphene in its bulk form possesses great mechanical and thermal stability, it is not fluorescent and it is plagued by poor solubility which restricts its use in other applications [**99**]. Through extensive research, these limitations have been overcome through the creation of graphene quantum dots (GQDs) [**97, 98**].

Graphene quantum dots are nanoparticles with a diameter of 20 nm or less and unlike their parent material, graphene; they are highly fluorescent and exhibit great solubility in various solvents [**98**]. These carbon-based nanoparticles have received a considerable amount of attention largely because unlike their semiconductor counterparts derived from tellurium, selenium and cadmium, are not known to be toxic [**100, 101**]. In addition to being chemically stable, displaying high photostability and biocompatibility, the luminescence properties of GQDs can be tailored to fit the desired application by altering the size of the nanoparticles. And along with changing the size, because they constitute of hydroxyls, carbonyls and epoxides as common functional groups, the surfaces thereof can be altered through reduction, passivation or the insertion of heteroatoms into the graphene network. These changes are achieved through varying the methods of synthesis [**97-102**].

1.3.2 Synthesis

The uses of GQDs in various fields of application have been driven by the synthetic routes adopted as they enable tailoring of the photoluminescence (PL) and chemical properties of GQDs. The conventional way of categorizing the manner in which GQDs are prepared has been divided into two groups, top-down methods and bottom-up methods [**98**].

1.3.2.1 Top-down

The top-down approach towards the synthesis of GQDs entails the use of bulk materials that are subjected to harsh chemical and/or mechanical treatment as a means of getting them to the nanoscale. The common materials that are used in top-down synthesis include coal, graphene, graphene oxide, graphite, single-walled carbon nanotubes (SWCNTs) and multi-walled carbon nanotubes (MWCNTs) [**102-106**]. These materials can be treated hydrothermally, solvothermally and electrochemically to produce the desired nanoparticles. Other methods include chemical exfoliation and laser ablation [**98**].

Hydrothermal and solvothermal methods of preparing GQDs differ in the sense that the hydrothermal route makes use of water while in the solvothermal route, organic solvents are employed [**98, 102, 107**]. Both methods involve the inclusion of the suitable/desired carbon material and heating in high pressure systems at elevated temperatures of 160 – 200 °C [**102, 107**]. Cyclic voltammetry has also been used in conjunction with a graphene oxide film used as the working electrode to produce GQDs [**108**]. Electrolyzing of a graphite rod in aqueous media at a constant current density has also been reported to produce GQDs [**102**]. A harsher top-down method is that of chemically exfoliating the carbon material such as SWCNTs with a strong oxidising agent such as potassium permanganate [**109**]. This method often includes the use of an acid (**Scheme 1.4**).

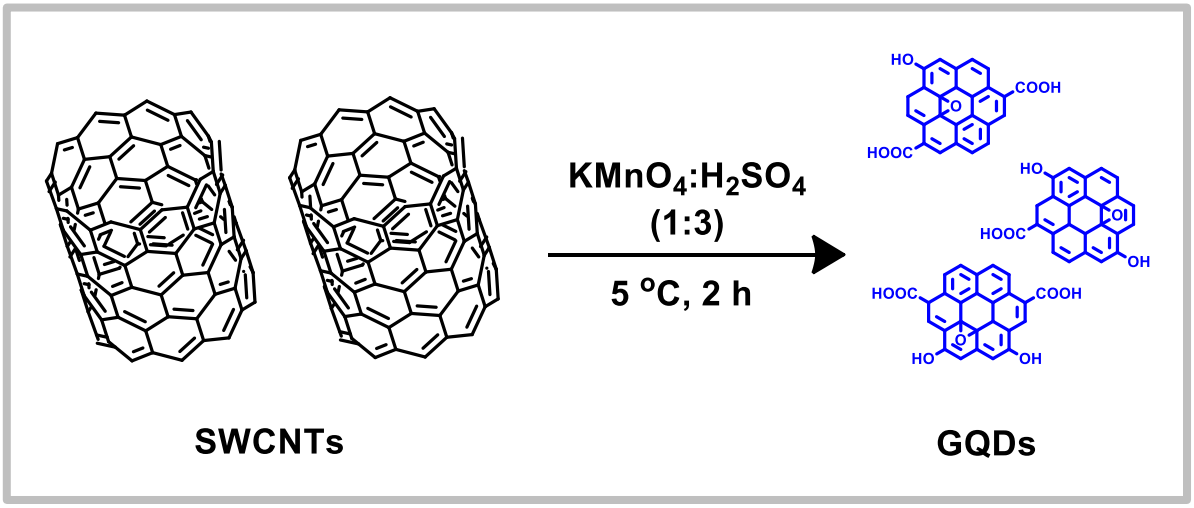

Scheme 1.4: An example of a top-down synthesis technique where SWCNTs are treated with a strong oxidising agent and a strong acid to produce graphene quantum dots (GQDs).

The use of laser ablation using an Nd:Yag laser has also been reported where irradiation of graphite powder in benzene resulted in the successful production of GQDs [**110**]. Highly orientated pyrolytic graphite has also been subjected to the laser power of a femtosecond laser to produce GQDs [**111**]. Top-down methods although useful, are often overshadowed by the fact that they are expensive and to a large degree, very difficult to control in terms of the size of the particles and limiting the number of side-products which is indirectly proportional to the yield of the desired product. This in turn makes them unsuitable for mass production [**98**].

1.3.2.2 Bottom-up

Because the methods of synthesis are classified based on the nature of the starting materials, in the case where small molecules are the starting materials, the method constitutes as a bottom-up approach. Bottom-up synthesis supersedes top-down methods because it is accompanied by fewer defects on the nanoparticles and enables better control over the size and functionalization of the GQDs [**98, 112, 113**]. The ability to achieve such control is further driven by the use of more specific precursors allowing for less stringent reaction conditions to be applied. The simplest methods of synthesizing GQDs that have been reported include microwave heating and/or pyrolysis of fructose, glucose and sucrose; all of which are naturally occurring sugars. Citric acid has also been used as a precursor in most bottom-up approaches [**98**] (**Scheme 1.5**). The use of lasers to create GQDs is not limited to top-down syntheses procedures and as a result of this, the acquisition of GQDs from laser ablation where the carbon source was chlorobenzene or dichlorobenzene has been witnessed [**114**]. Owing to the fact that this approach enables better size control and requires less stringent conditions, the bottom up approach was used in synthesizing the GQDs used in this work and in doing so, citric acid along with D-glucose were the sources of carbon.

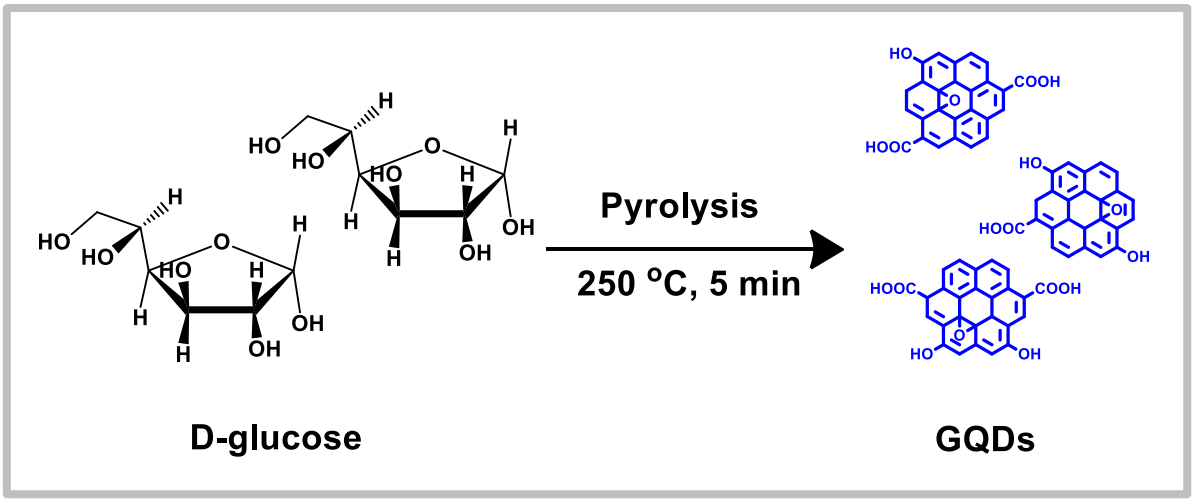

Scheme 1.5: A schematic view of how GQDs are obtained from glucose.

1.3.2.3 Doped and functionalized GQDs

The large similarity that GQDs have with graphene oxide is of great importance as it means that GQDs too bear a variety of oxygen-containing functional groups. The presence of these functional groups enables reduction and/or oxidation of the nanoparticle surface which in turn changes the photoluminescence (PL) properties and their optical behaviour [**115**]. Along with improving their properties, surface modification also facilitates the formation of complexes with other nanomaterials such as phthalocyanines through covalent bonding [**75**]. In addition to surface reduction and oxidation, the insertion of heteroatoms within the graphene matrix, referred to as doping, has resulted in enhanced PL and electrochemical activity of the GQDs [**115**]. The most favoured atom in terms of doping is nitrogen as it is very similar in size and behaviour to carbon. The fact that nitrogen induces minor defects is also important in the formation of nanocomposites through non-covalent linkages as the pi-conjugated system in the graphene network remains uncompromised. Other heteroatoms that have been explored include sulphur, boron and fluoride [**116-120**]. Doping of GQDs can be performed *in situ* or post-synthesis regardless of whether the approach is top-down or bottom-up one. Functionalization of pristine GQDs with NH_2 groups is one of the most common routes adopted in acquiring nitrogen-containing GQDs (**Table 1.1**) [**75**] however in this work; doping with nitrogen during the synthesis was the preferred option. This was done in order to produce GQDs that are rich in pyridinic-based nitrogen atoms as this form

is known to enhance the electrocatalytic activity of the material in which it is embedded [**121**]. Glutathione-doped GQDs were also prepared and compared to the pristine and nitrogen-doped GQDs. Glutathione enables co-doping with two different heteroatoms, sulphur and nitrogen without the inclusion of multiple steps.

1.3.3 Applications of GQDs

Since their inception, a large majority of the applications pertaining to GQDs have been fluorescent-based because that has been the distinction between them and graphene, fluorescence [**98**]. However, upon discovering that their optical and electronic properties are tuneable through surface modification and size-control, their uses have expanded towards photovoltaics, solar cells, biomedicine, photocatalysis and sensors [**97-99**]. And while they have extensive applications, for this thesis, the primary focus was their ability to enhance the electrocatalytic properties of Pcs. **Table 1.3** [**74, 75, 122-124**] provides information on some of the electrochemical sensors based on GQDs and the analytes that were detected.

Table 1.3: GQD-based electrochemical sensors that have been reported.

Electrode	Analyte	Reference
GQDs/GCE	Hydrazine	[**74**]
rGQDs/GCE, NH_2GQDs/GCE	Hydrazine	[**75**]
GQDs/Au	Hydrogen peroxide	[**122**]
GQDs/CCE	Glucose	[**123**]
NGQDs@NCNF/GCE	Nitrite	[**124**]

rGQDs – reduced graphene quantum dots; Au – gold electrode; CCE – carbon ceramic electrode; NCNF – n-doped carbon nanofibers.

1.3.4 Pc-GQD composites

Both phthalocyanines and GQDs have been found to be extremely useful independently as well as in the presence of other molecules. The combination of phthalocyanines with metal-based nanoparticles has resulted in improved systems for cancer treatment strategies as

well as photocatalytic degradation of water pollutants [**125, 126**]. Similarly, GQDs in conjunction with biological materials have yielded the creation of sophisticated bioimaging devices [**127**].

The discovery of GQDs has further driven modern research towards less harmful Pc-nanoparticle conjugates. Phthalocyanines and GQDs have been used together as complementary materials in photodynamic therapy as well as in the fabrication of solar cells [**125, 128**]. In fluorescence sensing, they often function as antagonists where the Pc quenches the fluorescence of the GQDs only to have it restored by the addition of a different molecule that serves as the analyte [**82, 83**]. Examples of Pc-GQD complexes and their use in electrochemistry are presented in **Table 1.1** [**66, 74, 75**]. As it has been shown in **Table 1.1**, only one asymmetrical Pc is linked to the GQDs by covalent means [**75**] with the other being π-stacked as the functional groups on both Pc and GQDs do not allow conjugation through an amide bond [**74**].

Despite the high preference for non-covalent (π-π stacking) and covalently linked Pc-GQD conjugates, the simplest way of preparing a working electrode using the two nanomaterials is that of sequentially modifying the electrodes. This method entails altering the order in which the electrode modifiers are applied and resembles π-π stacking to some degree with the difference being the strength of the electrostatic forces between the nanomaterials [**74**]. All three strategies of creating Pc-GQD systems are explored in this work where the sequential modifications with the tetra-substituted Pcs are studied in the presence of the pristine and doped GQDs, NGQDs and GSHGQDs while the NGQDs were the most favourable choice concerning the asymmetrical Pc complexes for both covalent (complexes **4** and **6**) and non-covalent (complexes **3**-**6**) linked Pc-GQD conjugates.

1.4 Analytes

The test analytes used in this work are inorganic materials, nitrite and hydrazine. Nitrites are common pollutants found in water and food [**129**]. Their classification into organic and inorganic forms is determined largely by their chemical structure with the inorganic forms being more water soluble than the organic forms [**130**]. A large majority of the inorganic

nitrites occur naturally in wells, food and are produced through the nitrogen cycle. Organic nitrites are mostly man-made for medical purposes but they too have proven to be harmful in the past [**130, 131**].

Hydrazine, although useful in various industries such as pharmaceutics as well as in the production of pesticides, has proven to be dangerous upon exceeding certain levels. And seeing that industrial processes are unable to find an alternative for it, the most ideal way to deal with it is to create efficient monitoring systems for it [**132**]. Nitrite and hydrazine were both selected as test analytes as CoPc derivatives have been successfully used in the electrocatalytic oxidation of the two [**68, 74, 75, 133, 134**].

1.5 Aims and objectives

In this work, exploration of doped GQDs is undertaken and in doing so, these doped GQDs are coupled with a few original Pc molecules. These nano-based complexes are then applied as electrochemical sensors with the hope of establishing sensors that are stable, non-toxic and can register low limits of detection.

The aims of the thesis are as follows:

- Synthesize symmetrical Pcs
    - Cobalt(II) and iron(III) Pcs
    - Characterize accordingly
    - Apply in the electro-oxidation of nitrite (independently and in conjunction with the GQDs)
- Synthesize GQDs
    - Pristine, nitrogen-doped (NGQDs) and glutathione-doped (GSHGQDs)
    - Characterize accordingly
    - Couple GQDs to Pcs through sequential modifications on the electrode with the intention of improving the electrocatalytic activity of the Pcs towards the oxidation of nitrite

Upon establishing the best-performing GQDs, the following was done:

- Synthesis of three original asymmetrical cobalt (II) phthalocyanines
    - Characterization of the molecules
    - A contemporary study on push-pull systems and other asymmetrical Pcs
        - Electro-oxidation of hydrazine
- Coupling of asymmetrical Pcs to NGQDs
    - π-π stacking and covalent linking
    - Characterization of nanoconjugates
    - Electro-oxidation of hydrazine

Chapter 2

Experimental

This chapter provides an outline on the synthetic procedures applied and lists of the materials and equipment used.

2.1 Materials

Sodium nitrite was purchased from Analar. Sodium hydroxide pellets were obtained from Minema. Iron(III) chloride was obtained from Merck. Hydrazine monohydrate, 1,8-diazabicyclo[5.4.0]undec-7-ene (DBU), cobalt (II) chloride anhydrous, 1-ethyl-3-(3-dimethylaminopropyl)-carbodiimide (EDC) and N-hydroxysuccinimide (NHS) were obtained from Sigma-Aldrich. All the other chemicals were of analytical grade and were used without further purification. All experiments were conducted using Millipore water from Milli-Q Water Systems (Millipore Corp. Bedford, MA, USA). The pristine GQDs [**135**], nitrogen-doped GQDs (NGQDs) [**136**] and glutathione-doped GQDs (GSHGQDs) [**137**] were synthesised as reported in literature. The syntheses of the 2,9,16,23-tetrakis-(3-(diethylamino)phenoxy) phthalocyaninato (**7**) [**84**], 2,9,16,23-tetrakis-(3-(diethylamino) phenoxy) phthalocyaninato cobalt (II) (**1**) [**84**] and 2,9,16-tris-(p-*tert*-butylphenoxy) mono carboxyphenoxy phthalocyaninato cobalt (II) (**3**) [**75**], 4-(4-aminophenoxy) phthalonitrile (**8**) [**138**], 4-(p-*tert*-butylphenoxy) phthalonitrile (**9**) [**139**], 4-(4-carboxyphenoxy) phthalonitrile (**10**) [**140**], and 4-(3-diethylamino phenoxy) phthalonitrile (**11**) [**84**] have been reported.

2.2 Equipment

1. Absorption spectra were recorded using a Shimadzu UV–Vis 2550 spectrophotometer.
2. Infra-red spectra were collected using a Bruker Alpha model FT-IR Spectrometer with a platinum universal attenuated total reflectance (ATR) sampling accessory.
3. The emission spectra were obtained using a Varian Cary Eclipse fluorescence spectrofluorimeter.
4. Raman spectra were obtained from a Bruker Vertex 70-Ram II Raman spectrometer fitted with a 1064 nm Nd:YAG laser and a liquid nitrogen cooled germanium detector.
5. The mass spectral data was acquired from a Bruker AutoFLEXIII smart-beam TOF/TOF mass spectrometer using α-cyano-4-hydrocinnamic acid as the matrix.

6. The elemental analysis was conducted using a Vario-Elementar Microcube ELIII.

7. X-ray diffraction patterns were obtained using a Bruker D8, Discover equipped with a Lynx Eye Detector using Cu Kα radiation (1 = 1.5405 Å, nickel filter).

8. X-ray photoelectron spectroscopy (XPS) spectral analyses were conducted using an AXIS Ultra DLD (supplied by Kratos Analytical) using Al (monochromatic) anode equipped with a charge neutralizer.

9. Transmission electron microscopy (TEM) images were obtained using a Zeiss Libra 120 TEM operating at 120 kV with a Megaview Olympus camera.

10. Size determination using dynamic light scattering (DLS) was performed using a Malvern Zetasizer nanoseries, Nano-ZS90.

11. Scanning electrochemical microscopy (SECM) experiments were conducted using a Uniscan Model 370 and a 25 mm Pt microelectrode (Uniscan) as the tip, a Pt counter electrode and Ag|AgCl wire as the pseudo-reference electrode.

12. Thermogravimetric analysis was conducted using a PerkinElmer TGA 8000^{TM} thermogravimetric analyser.

All electrochemical experiments were conducted on a Bioanalytical Systems 100W Electrochemical Analyzer using a three electrode setup, where the glassy carbon electrode (GCE, 3 mm diameter) served as the working electrode, a platinum wire as the counter electrode and a silver/silver chloride (in 3.0 M KCl) wire as the reference electrode. Solutions were deaerated by bubbling argon gas prior to the experiments and the electrochemical cell was kept under an argon atmosphere throughout the experiments.

2.3 Syntheses

2.3.1 Synthesis of the 2,9,16,23-Tetrakis-(3-(diethylamino)phenoxy) phthalocyanato) iron(III) chloride (2), Scheme 3.1A

The iron(III) chloride Pc (**2**) was obtained through dissolving the unmetallated Pc analogue (0.100 g, 0.086 mmol) and $FeCl_3$, 0.013 g (0.086 mmol) in dimethylformamide(DMF, 8 mL) in the presence of DBU (0.5 mL). The solution was refluxed in an inert atmosphere for 4 h. Upon cooling, the product was precipitated with water and methanol (1/1), dried in an oven at 70 °C and purified further through column chromatography with chloroform as the eluent to give complex **2**. Yield: 71% (w/w); UV/vis (DMF): λ_{max}/nm (log Ɛ): 688 (3.60), 315 (4.19). IR [(KBr), ν_{max}/cm^{-1}]: 821, 746, 683 (aromatic C-H_{str}), 2916, 2855 (aliphatic C-H_{str}), 1598 (C=C), 1460 (C=C-H), 1356, (C-H), 1268 (C-N), 1215 (C-O), 1129, 1078 (C-O-C). Anal. calc. for $C_{72}H_{68}ClFeN_{12}O_4$: C, 68.8; H, 5.45; N, 13.4. Found: C, 67.8; H, 5.54; N, 12.3. MS (MALDI-TOF) (*m/z*): calc.: 1255.45 amu; found: 1221.53 amu $[M - Cl + H]^+$ and 1241.02 amu $[M - CH_3]^+$.

2.3.2 Synthesis 2,9,16-tris-(4-*tert*-butylphenoxy) mono aminophenoxy phthalocyanato cobalt (II) (4), Scheme 3.1B

The synthesis of complex **4** was achieved through dissolving 4-(p-*tert*-butylphenoxy) phthalonitrile (**9**) (0.300 g, 1.09 mmol), 4-(4-aminophenoxy) phthalonitrile (**8**) (0.085 g, 0.362 mmol) and cobalt (II) chloride (0.200 g, 1.54 mmol) in 8 mL of 1-hexanol in the presence of 0.5 mL of DBU. The solution was refluxed in an inert atmosphere for 5 h. Upon cooling, the product was precipitated with water and ethanol (1:1 v/v), vacuum dried and purified further through column chromatography in which Si_{60} served as the stationary phase while tetrahydrofuran (first fraction) and chloroform (second fraction) acted as the mobile phase. The desired product which was the second fraction was purified further with dichloromethane and ethyl acetate to give complex **4**. Yield: 13% (w/w); UV/vis (dimethylformamide, DMF): λ_{max}/nm (log Ɛ): 673 (4.84), 607 (4.22), 335 (4.40). IR [(KBr), ν_{max}/cm^{-1}]: 2917, 2849 (aliphatic C-H_{str}), 1599 (C=C), 1460 (C=C-H), 1231 (C-N), 1165, 1055 (C-O-C), 826, 748 (aromatic C-H_{str}). Anal. calc. for $C_{68}H_{57}CoN_9O_4$: C, 72.2; H, 5.12; N, 11.2.

Found: C, 73.4; H, 5.61; N, 10.2. MS (MALDI-TOF) (*m/z*): calc.: 1122.39 amu; found: 1123.11 amu $[M + H]^+$.

2.3.3 Synthesis of 2,9,16-tris-(3-diethylamino)phenoxy) mono carboxyphenoxy phthalocyanato cobalt (II) (5), Scheme 3.1C

Complex **5** was obtained through dissolving 4-(3-diethylamino phenoxy) phthalonitrile (**11**) (0.300 g, 1.03 mmol), 4-(4-carboxyphenoxy) phthalonitrile (**10**) (0.091 g, 0.343 mmol), and cobalt (II) chloride (0.200 g, 1.54 mmol) in 8 mL of DMF in the presence of 0.5 mL of DBU. The solution was refluxed in an inert atmosphere for 12 h, cooled to room temperature, precipitated with water and ethanol (1:1 v/v) and washed further with ethanol. The crude product was dried under vacuum and purified through silica-based (Si_{60}) column chromatography. The symmetrical analogues were eluted with chloroform and hexane (9:1) and the desired product which was the last fraction was eluted with DMF. Following its acquisition with DMF, the final product was precipitated in ice, sedimented through centrifugation, washed with water and dried in an oven at 70 °C. Yield: 65% (w/w); UV/vis (DMF): λ_{max}/nm (log Ɛ): 667 (4.97), 610 (4.48), 328 (4.94). IR [(KBr), ν_{max}/cm^{-1}]: 2965 (aliphatic C-H_{str}), 1598 (C=C), 1463 (C=C-H), 1223 (C-O), 1222 (C-N), 1085 (C-O-C), 820, 743 (aromatic C-H_{str}). Anal. calc. for $C_{69}H_{59}CoN_{11}O_6.2H_2O$: C, 67.21; H, 5.11; N, 12.50. Found: C, 67.11; H, 5.60; N, 12.50. MS (MALDI-TOF) (*m/z*): calc.: 1196.40 amu; found: 1198.50 amu $[M + 2H]^+$.

2.3.4 Synthesis of 2,9,16-tris-(3-diethylamino)phenoxy) mono aminophenoxy phthalocyanato cobalt (II) (6), Scheme 3.1D

Complex **6** was obtained through dissolving 4-(3-diethylamino phenoxy) phthalonitrile (**11**) (0.300 g, 1.03 mmol), 4-(4-aminophenoxy) phthalonitrile (**8**) (0.081 g, 0.343 mmol) and cobalt (II) chloride (0.200 g, 1.54 mmol) in 8 mL of 1-hexanol in the presence of 0.5 mL of DBU. The solution was refluxed in an inert atmosphere for 12 h, cooled to room temperature and precipitated with water and ethanol (1:1 v/v). After drying under vacuum, the product was eluted from a silica column with chloroform and methanol as the eluents

(9:1). Yield: 19% (w/w); UV/vis (DMF): λ_{max}/nm (log Ɛ): 676 (4.40), 614 (3.95), 316 (4.37). IR [(KBr), ν_{max}/cm^{-1}]: 2916 (aliphatic C-H_{str}), 1601 (C=C), 1464 (C=C-H), 1268 (C-N), 1225 (C-O), 1088, 1078 (C-O-C), 827, 745 (aromatic C-H_{str}). Anal. calc. for $C_{68}H_{60}CoN_{12}O_4$: C, 69.9; H, 5.18; N, 14.4. Found: C, 69.9; H, 5.75; N, 14.9. MS (MALDI-TOF) (*m/z*): calc.: 1167.42 amu; found: 1150.97 amu $[M - NH_2]^+$ and 1123.03 amu $[M - NH_2 - 2CH_3]^+$.

2.4 Formation of conjugates

2.4.1 Conjugation through π-π stacking, Scheme 3.2A

Each CoPc derivative (3 mg, 2.60×10^{-6} mol for **3**, 2.67×10^{-6} mol for **4**, 2.51×10^{-6} mol for **5**, and 2.57×10^{-6} mol for **6**) was dissolved in 2 mL of DMF, followed by mixing with 2 mg of the NGQDs in 1 mL of water (complex **5** is used as an example in **Scheme 3.2A**). The mixtures were then sonicated at room temperature for 1 h. Following that, the mixtures were left to stir at room temperature for 24 h. The newly formed conjugates were precipitated and washed in ethanol and dried under vacuum (**Scheme 3.2A**). The conjugates are represented as **3**πNGQDs, **4**πNGQDs, **5**πNGQDs and **6**πNGQDs.

2.4.2 Conjugation through amide bond, Scheme 3.2B

Covalent linking of complexes **4** and **6** to GQDs was achieved through the formation of an amide bond between the primary amine on the Pc (complex **6** used as an example in **Scheme 3.2B**) and the carboxylic acid groups from the GQDs. The manner in which this was carried out was through dissolving 4 mg of the GQDs in 2 mL water. To this solution, NHS (0.10 g, 8.69×10^{-4} mol) and EDC (0.10 g, 5.22×10^{-4} mol) were added and the mixture was sonicated until all the solid particles had dissolved. Then, 4 mg of each Pc (3.56×10^{-6} mol for **4** and 3.42×10^{-6} mol for **6**) was dissolved in 1 mL of DMF and added separately to GQDs mixtures, followed by sonication for 1 h. The resulting mixtures were then left to stir at room temperature for 24 h after which they were precipitated in ethanol and dried under vacuum (**Scheme 3.2B**). It is important to note that π-π stacking is also possible during the

formation of the covalently linked conjugates. The covalently linked conjugates are represented as **4**@NGQDs and **6**@NGQDs.

2.5 Electrode modification

Electrode modification was achieved through the drop-dry method. However, before modification, the GCE was cleaned by polishing in a slurry of alumina nanopowder (Sigma-Aldrich) on a SiC-emery paper and rinsed with Millipore water several times. The electrode was further treated to ultra-sonication in 1.0 M of HCl and rinsed with Millipore water again.

In the studies concerning nitrite, electro-oxidation was carried out using complex **1** and **2**, pristine GQDs, NGQDs and the GSHGQDs. Sequential modifications where also performed in which the order of modification between the complexes **1** and **2** and the different GQDs was varied. In preparing the GQDs, 2 mg of each kind was dissolved in 1 mL Millipore upon which 5 µL of the solution was placed on the GCE, followed by drying in an oven at 60 °C overnight. The electrodes are represented as GCE-GQDs, GCE-NGQDs, and GCE-GSHGQDs for pristine, N-doped and GSH-functionalized GQDs, respectively. Complexes **1** and **2** (1.0 mg) were dissolved separately in 1.0 mL DMF. Electrode modification using complexes **1** and **2** independently was the same as that of the GQDs, 5 µL of the complex was dropped onto the electrode surface and dried in an oven at 60 °C. These electrodes are presented as GCE-**1** and GCE-**2** in **Table 4.1**.

Experiments where both complex **1** and the GQDs were used to modify the electrodes were also conducted. The same solutions applied for the single electrode modifications were used and the quantities thereof remained unchanged, 5 µL from each solution. In the case were the GQDs are followed by the placement of complex **1** on top, the electrodes are presented as GCE-GQDs/**1**, GCE-NGQDs/**1** and GCE-GSHGQDs/**1**.

Placement of complex **1** before the GQDs solutions resulted in the acquisition of the following electrodes: GCE-**1**/GQDs, GCE-**1**/NGQDs and GCE-**1**/GSHGQDs. In all cases following the modification of the GCE with the nanomaterials, the electrodes were left to dry overnight in an oven set at 60 °C. The same protocol was followed in the application of complex **2** as an electrode modifier except this was only done for the NGQDs. The complete

list of modified electrodes used in the electrocatalytic oxidation of nitrite is presented in **Table 4.1**.

Following up on the information obtained in the nitrite studies, new complexes were designed for the detection of hydrazine. These complexes were used in conjunction with the NGQDs through forming nanocomposites by means of π-π stacking and covalent linking where applicable. As it was for nitrite, the same approach regarding preparing the GQDs was taken in which 2 mg of the NGQDs was dissolved in 1 mL Millipore water. Following this, 5 µL of the NGQDs solution was placed on the GCE and dried in an oven at 60 °C overnight. The electrode is represented as GCE-NGQDs (**Table 4.1**). The Pc complexes and conjugates were prepared in the same manner as it was concerning the nitrite studies. Again, 1 mg of complexes **3**-**6** and their respective conjugates were dissolved in 1 mL DMF, 5 µL of each solution was dropped onto the electrode and dried in an oven at 60 °C overnight. The electrodes which contain the Pc complexes only are referred to as GCE-**3**, GCE-**4**, GCE-**5** and GCE-**6**. The electrodes modified with the conjugates are represented as: GCE-**3**πNGQDs, GCE-**4**πNGQDs, GCE-**5**πNGQDs, GCE-**6**πNGQDs, GCE-**4**@NGQDs, and GCE-**6**@NGQDs where the ones with the "π" sign are the π-π stacked conjugates and the ones with "@" sign represent the covalently linked conjugates. The complete list of the electrodes used in the electro-oxidation of hydrazine is presented in **Table 4.1**.

The results discussed in the following chapters (3 – 5) have been submitted to peer-reviewed journals for publication.

- **R. Nkhahle**, K. E. Sekhosana, G. Fomo, T. Nyokong, The electrocatalytic activity of a cobalt phthalocyanine in the presence of doped graphene quantum dots. [*Submitted, 19 August 2018*]

- **R. Nkhahle**, K. E. Sekhosana, S. Centane, T. Nyokong, Electrocatalytic activity of asymmetrical cobalt phthalocyanines in the presence of N doped graphene quantum dots: the push-pull effects of substituents. In *Electroanalysis* **2019**, 31, 891-904.

Other publications not related to the thesis:

- N. Nwahara, **R. Nkhahle**, B. P. Ngoy, J. Mack, T. Nyokong, Synthesis and photophysical properties of BODIPY-decorated graphene quantum dot-phthalocyanine conjugates in *New Journal of Chemistry* **2018**, 42, 6051-6061.

- K. E. Sekhosana, **R. Nkhahle**, T. Nyokong, The primary demonstration of exciton coupling effects on optical limiting properties of blue double- decker lanthanide phthalocyanine salts in *ChemistrySelect* **2018**, 3, 6671-6682.

Chapter 3

Results and discussion

Detailed discussions related to the synthesis and characterization of the GQDs, the complexes and their corresponding conjugates are carried out in this chapter.

3.1 Characterization of GQDs

The synthesized GQDs, despite having been reported before [**135-137**], were all characterised using various spectroscopic techniques to showcase the differences that doping endows upon them. These GQDs are displayed in **Fig. 3.1**.

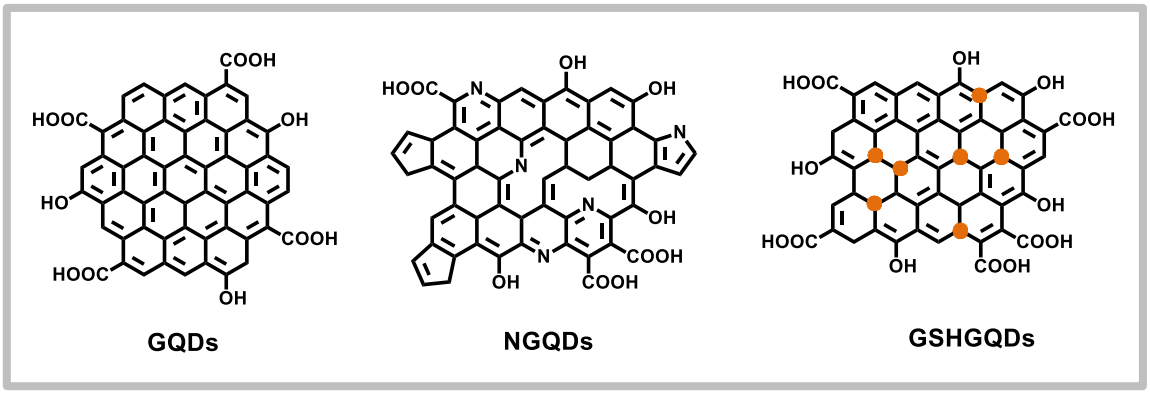

Fig. 3.1: An illustration of the GQDs synthesised where the orange dot in GSHGQDs represents the glutathione.

3.1.1 UV-vis spectroscopy

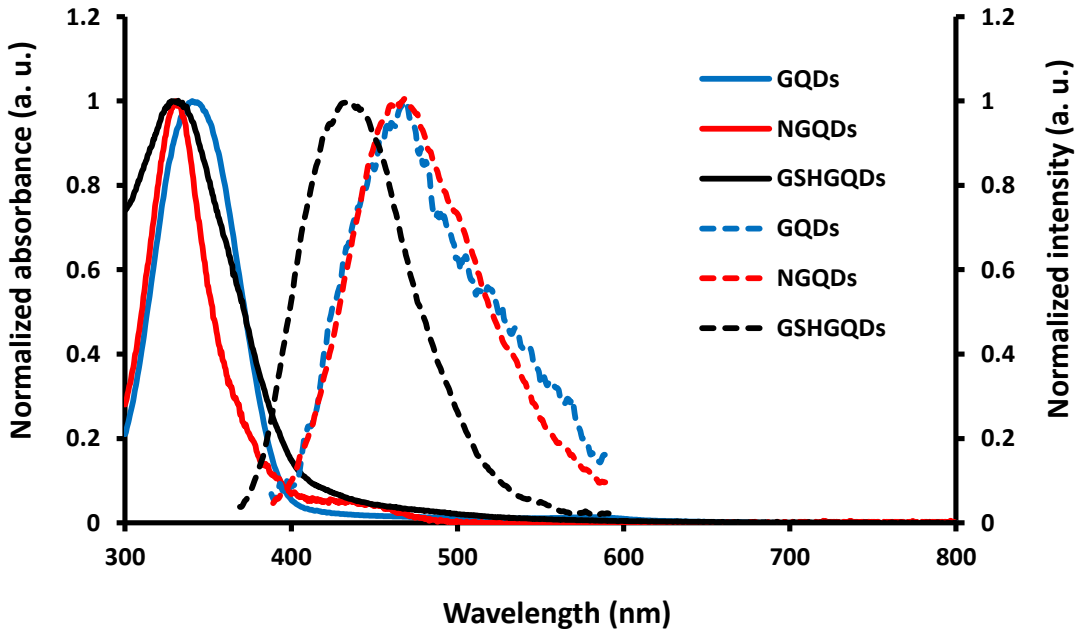

Fig. 3.2: The absorption spectra of the GQDs (solid lines) together with their emission spectra (dashed lines) in water.

The absorption spectra of the GQDs are shown in **Fig. 3.2** where maximum absorption is observed at 328 nm for the GSHGQDs and at 331 nm for the NGQDs. The absorption spectra of NGQDs and GSHGQDs are blue shifted compared to the pristine GQDs reaching their maxima at 340 nm (**Fig. 3.2, Table 3.1**). The introduction of nitrogen and GSH into the graphene network to produce NGQDs and GSHGQDs results in a reduction of oxygen functionalities, hence the blue shifting in spectra for the doped GQDs [**141**].

The emission spectra of the GQDs adhere to the same trend observed in the absorption spectra where the pristine GQDs are red shifted compared to the doped GQDs. A blue shift of 33 nm was observed for the GSHGQDs which is quite extreme in comparison to the blue shift of 4 nm observed for the NGQDs. A larger blue shift of 54 nm has been reported for SN-doped GQDs (compared to NGQDs) but even so, the reasons as to why this may be the case remain unknown with the most plausible argument being put forth being that of the S atom transforming the surface states of the GQDs [**142, 143**]. The main contributing factor to the blue shift in the emission of the GSHGQDs is the reduction in sp^2 hybridized entities. Co-doping with S and N, as brought about by the GSH, reduces the sp^2 domains which are responsible for the fluorescence of the GQDs. A small quantity of sp^2 hybridized centres results in emission being observed at lower wavelengths [**142**]. Maximum emission for the pristine GQDs is observed at 468 nm, at 464 nm for the NGQDs and at 435 nm for the GSHGQDs respectively (**Fig. 3.2, Table 3.1**).

3.1.2 FT-IR

Another standard technique employed in the characterizing of GQDs is Fourier transform infrared (FT-IR) spectroscopy. Due to the fact that graphene is composed largely of sp^2 and sp^3 hybridized carbon atoms arranged in a honeycomb-like manner, stretching frequencies associated with C=C and C-C are expected to appear in the IR spectrum of GQDs. A C=C stretch at 1562 cm^{-1} for the pristine GQDs, 1547 cm^{-1} for the NGQDs and 1543 cm^{-1} for the GSHGQDs are observed (**Fig. 3.3**). Upon doping, new bonds are formed and other stretching frequencies associated with the resultant functional groups appear. In the spectrum for the NGQDs, a weak stretch attributed to a C-N bond appears at approximately 1103 cm^{-1} while a sharper peak assigned to an N-H bond appears at 1715 cm^{-1}. The broad stretch from 3000

cm^{-1} to 3500 cm^{-1} in the case of the pristine GQDs is attributed mainly to the O-H bonds due to the presence of the carboxylic acid groups on the terminal ends of the graphene (**Fig. 3.3**). Regarding the GSHGQDs, an N-H stretch is observed at 1699 cm^{-1} while a weak peak attributed to the thiol group in the glutathione appears at 2533 – 2633 cm^{-1}. From this, it can be inferred that not all the glutathione molecules are part of the graphene network but some are rather adsorbed onto the surface while the others interact with the framework through other functional groups. Furthermore, exposure of the thiol group from the adsorbed glutathione may result in the formation of disulfide bonds which in turn may enhance or inhibit the activity of the GSHGQDs [**144**].

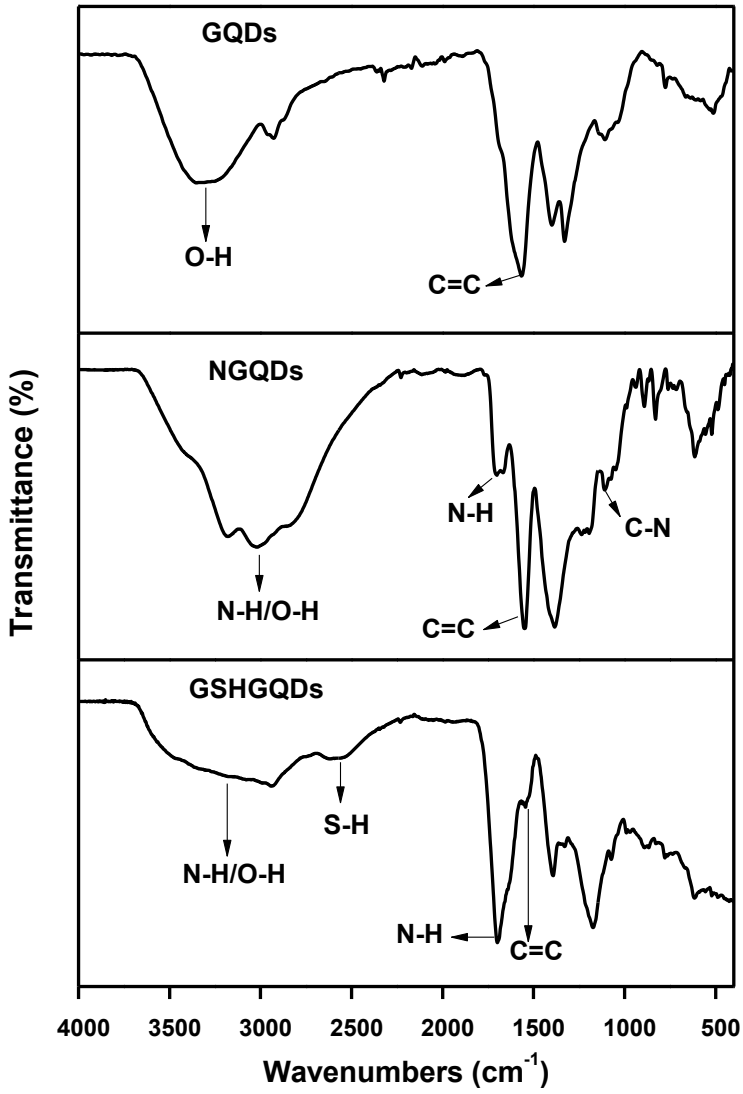

Fig. 3.3: Infrared spectra of the synthesized GQDs.

3.1.3 Raman spectroscopy

Graphene-based materials are characterised by the presence of two distinct peaks in the Raman spectra. These bands known as the D and the G bands appear at approximately 1100 cm^{-1} and 1600 cm^{-1} (**Fig. 3.4**) [**145**]. The G band is the result of in-plane vibrations of sp^2 bonded carbon atoms whereas the D band is caused by out-of-plane vibrations attributed to the presence of structural defects (sp^3 carbons) [**145**]. In relation to the pristine GQDs, the Raman spectra of the NGQDs and GSHGQDs are similar in that the D bands for each shift to higher Raman frequencies while the opposite occurs for the G bands (**Fig. 3.4**). Shifts in the Raman spectra towards lower or higher wavenumbers are related to the chemical bond length of the atoms that make up the graphene network [**141**]. Shifts in the G band, particularly those regarding NGQDs, have been attributed to the structural distortion caused by the different bond distances of C-N and C-C bonds [**141**]. The same may apply to the GSHGQDs as glutathione introduces both nitrogen and sulphur to the graphene core.

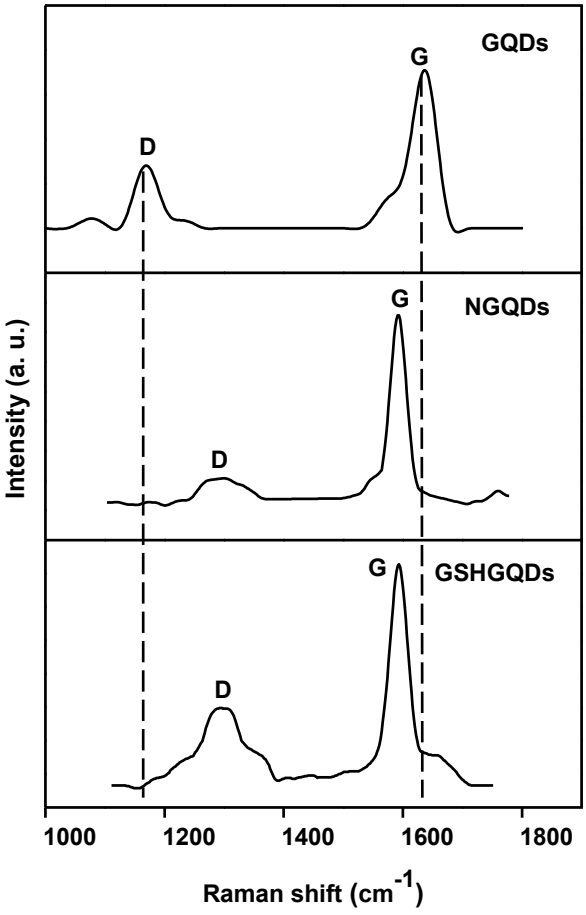

Fig. 3.4: Raman spectra of the synthesized GQDs.

The extent of defects or quality of the graphene core in GQDs can be determined by measuring the ratio of the intensities of the D and G bands (I_D/I_G).The calculated I_D/I_G ratio for the pristine GQDs was 0.42. Although doping is known to introduce surface defects which in turn results in higher I_D/I_G ratios, the opposite was observed for the NGQDs with an I_D/I_G ratio of 0.16 being recorded (**Table 3.1**). This may be attributed to nitrogen having a lower valency than carbon therefore prohibiting the existence of additional surface-based functional groups such as epoxides as it forms part of the graphene framework. In addition to a possible decline in surface functional groups, the method of synthesis as well as the drying temperature may have induced lower defects through an increment in the graphiticity of the graphene sheets that make up the NGQDs. An increased ratio of 0.58 was observed for the GSHGQDs (**Table 3.1**). This, to some extent further confirmed the FT-IR findings that some of the GSH was indeed adsorbed onto the surface. The adsorbed GSH may have put additional strain onto the graphene sheets not only through tensile forces but through the general position of the atoms in space of the GSH itself; some may have assumed positions that stretched the C-C/C=C bonds that make up the graphene matrix.

3.1.4 Transmission electron microscopy (TEM)

The TEM micrographs obtained show monodispersed particles (**Fig. 3.5**). Using the Image J software, the average particle sizes for each of the GQDs were approximated and the general observation was an increase in the particle size upon doping (**Table 3.1**). The GSHGQDs are slightly larger than the NGQDs because GSH enables co-doping with both sulphur and nitrogen. Overall, all the particles have a diameter of less than 10 nm with average sizes ranging from 1.4 to 2.8 nm (**Fig. 3.5, Table 3.1**).

Table 3.1: Spectral data and sizes of the GQDs. Absorption and emission spectra in water.

Type of GQDs	Absorption (nm)	Emission (nm)	Size (nm) (TEM)	I_D/I_G ratio
Pristine GQDs	340	468	1.4	0.42
NGQDs	331	464	2.4	0.16
GSHGQDs	328	435	2.8	0.58

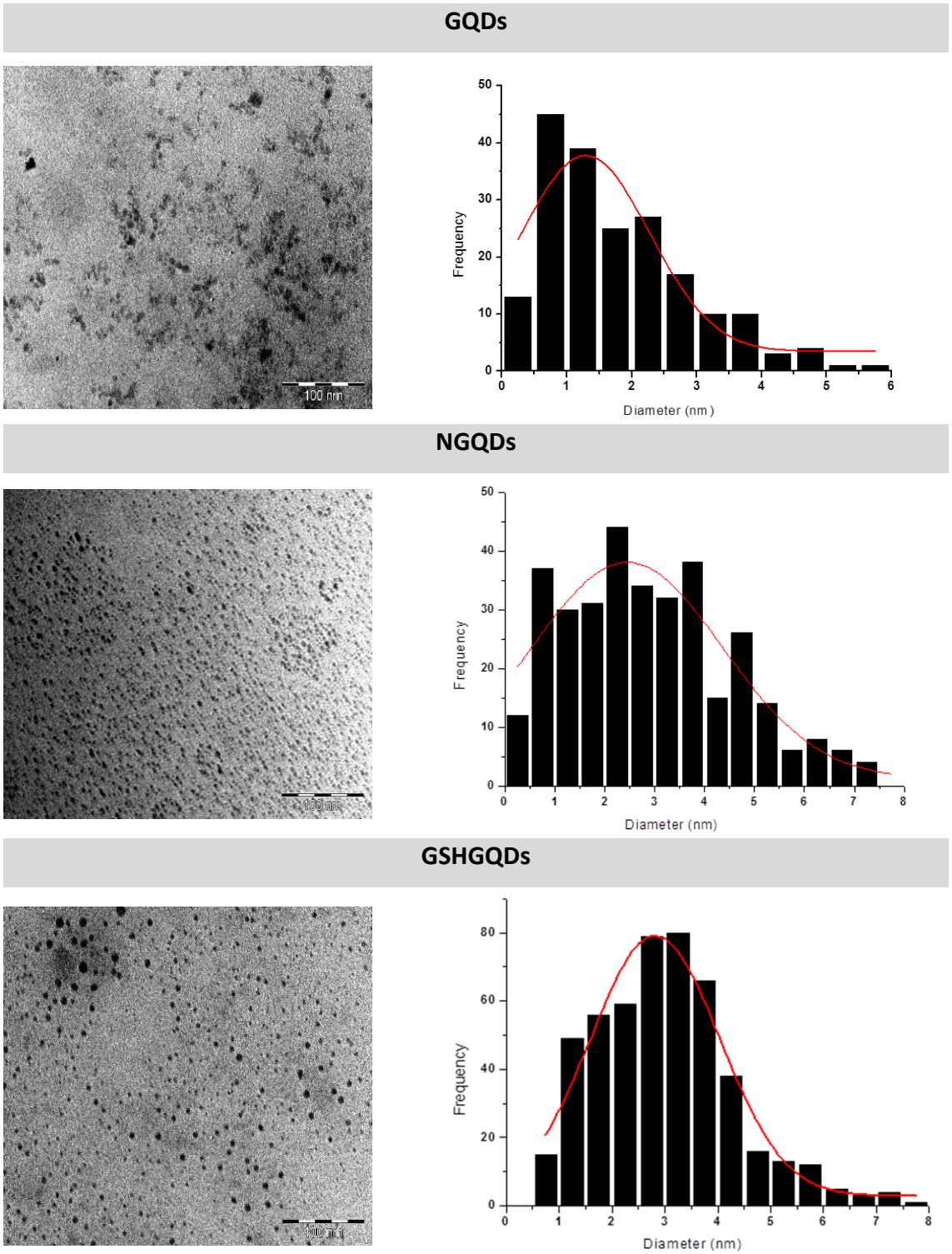

Fig. 3.5: TEM images of GQDs dispersed in water. (Scale: 100 nm)

3.1.5 X-ray diffraction (XRD)

X-ray diffractograms of the prepared GQDs are presented in **Fig. 3.6**. The patterns illustrated where broad peaks arise at 2θ = 15 – 45° are attributed to the graphitic nature of the materials which is bear a strong reflection in the 002 plane [**146, 147**].

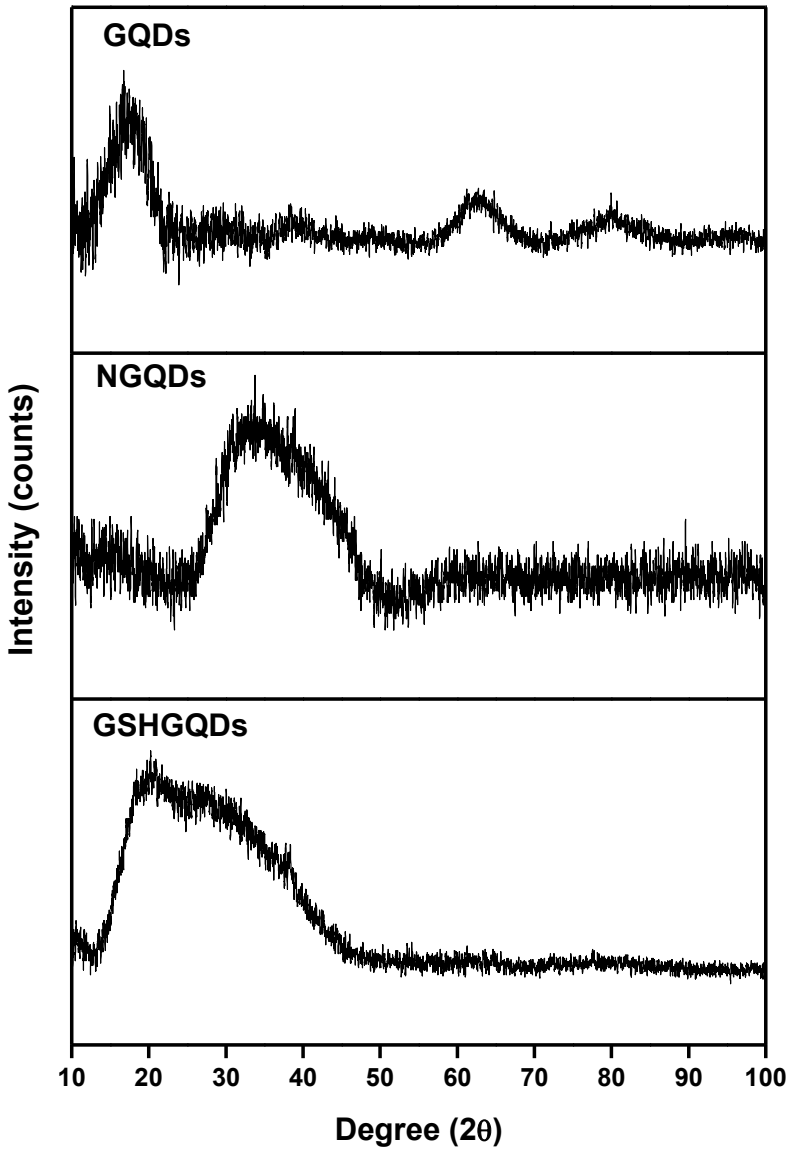

Fig. 3.6: Diffractograms of the synthesized GQDs.

A value reaching its maximum at 2θ = 16.7° in the 002 plane is registered for the pristine GQDs. Shifts in the peak positions to higher 2θ values for the NGQDs (2θ = 33.7°) and the GSHGQDs (2θ = 20.3°) may be attributed to a higher content of elemental carbon as they are slightly larger in size compared to the pristine GQDs [**148**]. The broadness of the peaks

corresponds to the miniscule size and the amorphous morphology assumed by GQDs (**Fig. 3.6**) [**149, 150**].

3.2 Synthesis and characterization of Pcs

Complexes **1** and **3** are known while **2**, **4**, **5** and **6** are reported for the first time in this thesis and their syntheses is described accordingly. The synthesis of complex **2** was completed in a manner slightly different from that which has been reported for complex **1** [**84**]. Quite often, metallation is conducted during cyclotetramerization of the phthalonitrile however in this instance, metallation was carried out post-synthesis of the H_2Pc (**7**) [**Scheme 3.1A**]. And although *in situ* metallation is preferred as it is often accompanied by greater yields, post-cyclotetramerization metallation is also acceptable as *in situ* metallation is not always completely successful with unmetallated analogues being observed during the purification process.

Complexes **4**-**6** were synthesized using the statistical condensation approach where the stoichiometric ratio of 1:3 of phthalonitriles was maintained throughout the syntheses (**Schemes 3.1B, 3.1C and 3.1D**) with the progression of the reactions being monitored using mass spectrometry. Although higher ratios such as 9:1 have resulted in the successful production of asymmetric Pcs, these are often plagued by the excessive formation of the tetra-substituted analogues which compromises the yield of the desired A_3B-type Pcs [**40**]. The complexes bearing the primary amine group on one end, complexes **4** and **6**, were synthesized using 1-hexanol while the synthesis of complex **5**, that with a carboxylic acid group, was carried out using DMF because the use of 1-hexanol was accompanied by a low yield unsuitable for further characterizing and application. For all the complexes, the condensation reaction was performed in an inert atmosphere, in the presence of the metal salt with DBU as the base. Despite longer reaction times being more favourable as they ensure that the reaction runs to completion with a minimum amount of the reactants remaining at the end, lengthy reaction times at elevated temperatures may result in degradation of the product hence the variations in the times employed during the synthesis of complexes **4-6**. The progression of the reactions was monitored using mass spectrometry.

A

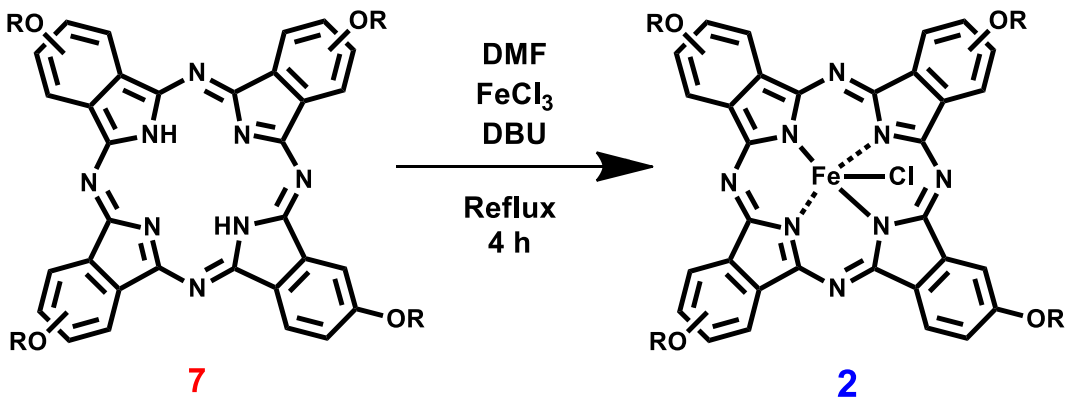
RO
OR
NH
N
HN
RO
OR
DMF
FeCl3
DBU
Reflux
4 h
Fe
Cl
RO
OR
7
2

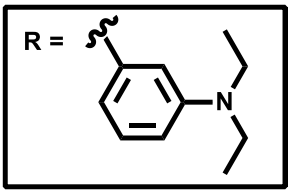
R =
N

B

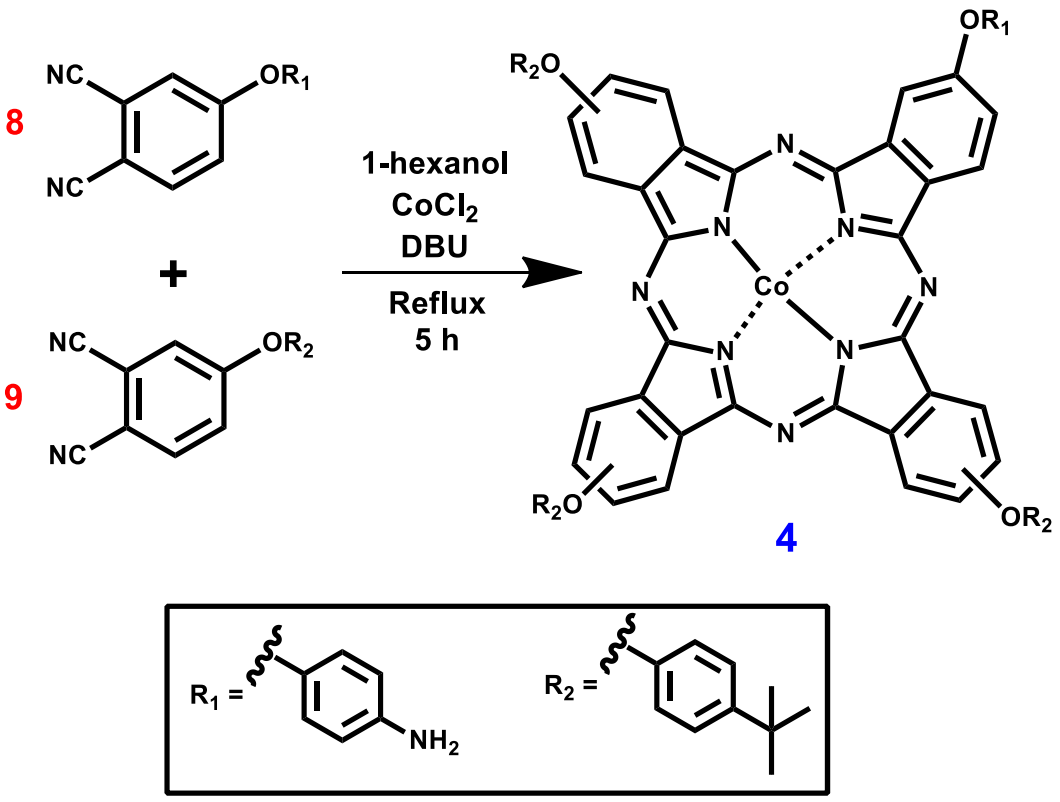
NC
OR1
NC
8
+
NC
OR2
NC
9
1-hexanol
CoCl2
DBU
Reflux
5 h
R2O
OR1
Co
R2O
OR2
4
R1 =
NH2
R2 =

C

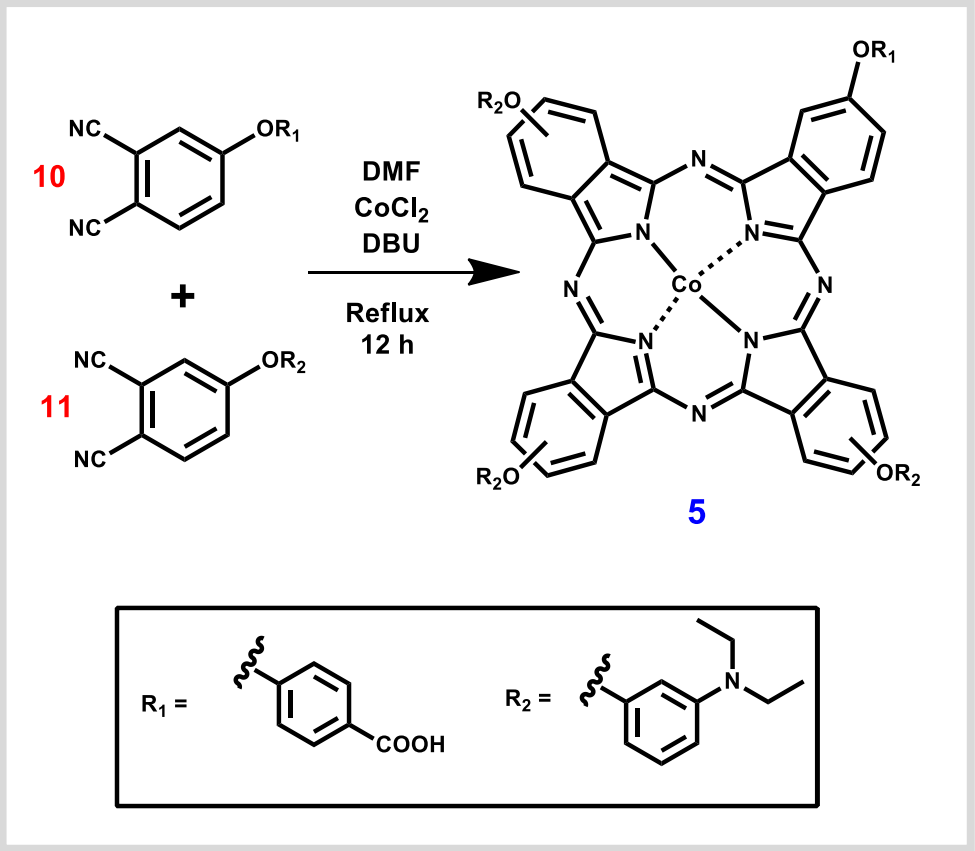

D

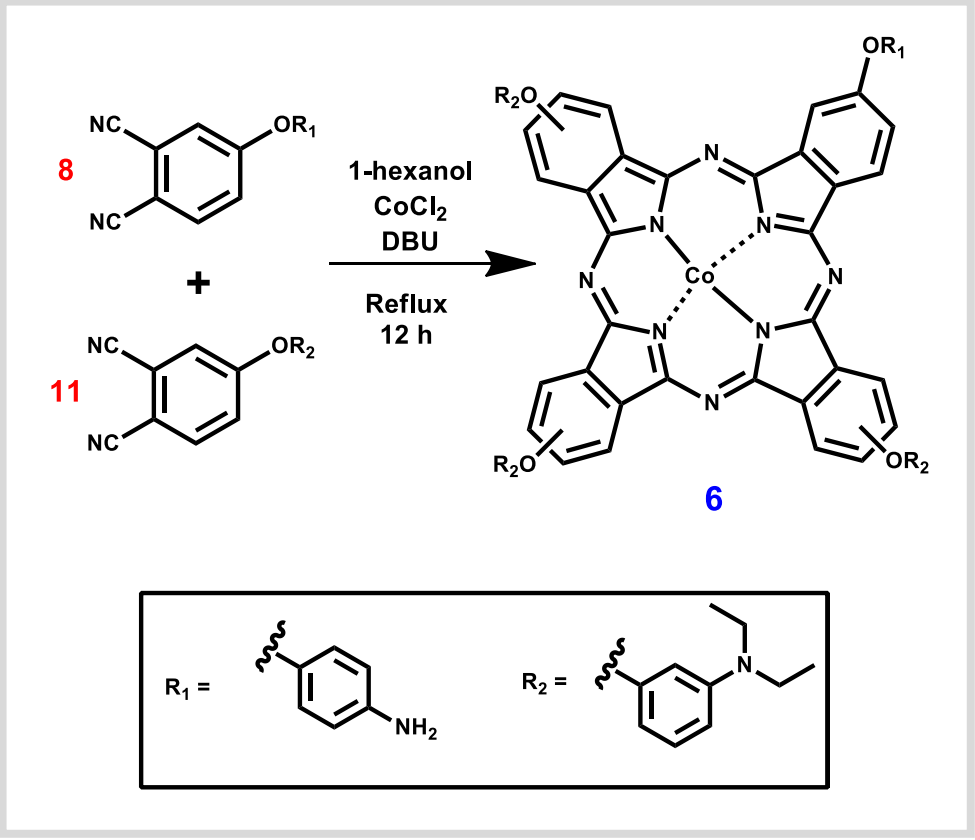

Scheme 3.1: Syntheses of complexes **2**, **4**, **5** and **6**.

In the mass spectrum for complex **2**, molecular ion peaks were observed at 1221.53 and at 1241.02 $[M]^+$. The peak appearing at 1221.53 is assigned to the Pc without the chloride axial ligand, while the less prominent one appearing at 1241.02 is ascribed to the molecule without one methyl group on one of the substituents, all of which may have been caused by fragmentation of the Pc during ionization (**See appendix, Fig. A1**). For complex **4**, a molecular ion peak which corresponds to the expected mass with the addition of one proton was observed at 1123.11 $[M]^+$ (**Fig. A2**). The mass obtained for complex **5** was 1198.50 $[M]^+$ which is consistent with the expected mass and two additional protons (**Fig. A3**). Regarding complex **6**, two peaks appearing at 1150.97 and 1123.03 were observed with the former being assigned to the Pc molecule without the NH_2 group while the latter was ascribed to the Pc without two methyl groups as well as the amine. The expected mass for complex **6** was 1167.42 however this was not observed as the molecule may have suffered the same fate as complex **2**, cleavage during the ionization process hence the acquisition of the two signals explained above (**Fig. A4**).

FT-IR further confirmed the acquisition of complexes **2**, **4**, **5** and **6** through the display of frequencies associated with the anticipated functional groups (**Fig. 3.7**). For complexes **2**, **5** and **6** the stretching frequencies are almost identical as the structures of the Pcs are not too different with the exception of the substituents that are responsible for the asymmetry of the molecules. Regarding complex **2**, C-H stretches associated with the aromatic and aliphatic regions are seen at 2916, 2855, 821, 746 and 683 cm^{-1}. The C-O-C and C-O stretches which stem from the phenoxy substituent appear at 1215 and 1129 cm^{-1} respectively whilst the IR frequency associated with the C-N bond appears at 1268 cm^{-1} (**Fig. 3.7**). For complex **5**, the C-H stretches related to the aromatic and aliphatic regions are seen at 2965, 820 and 743 cm^{-1} while for complex **6**, they appear at 2916, 827 and 745 cm^{-1}. The C-O-C stretch which stems from the phenoxy substituent appear at 1085 and 1088 cm^{-1} for complex **5** and **6** respectively whilst the IR frequency associated with the C-N bond appears at 1222 and 1268 cm^{-1} for the two complexes, respectively (**Fig. 3.7**). Peaks at 2917, 2849, 826 and 748 cm^{-1} that are due to the C-H stretches associated with the aromatic and aliphatic regions are observed for complex **4** (**Fig. 3.7**). The C-O-C stretch which is the result of the phenoxy substituent in complex **4** appears at 1165 cm^{-1} whilst the IR frequency associated with the C-N bond appears at 1231 cm^{-1} (**Fig. 3.7**).

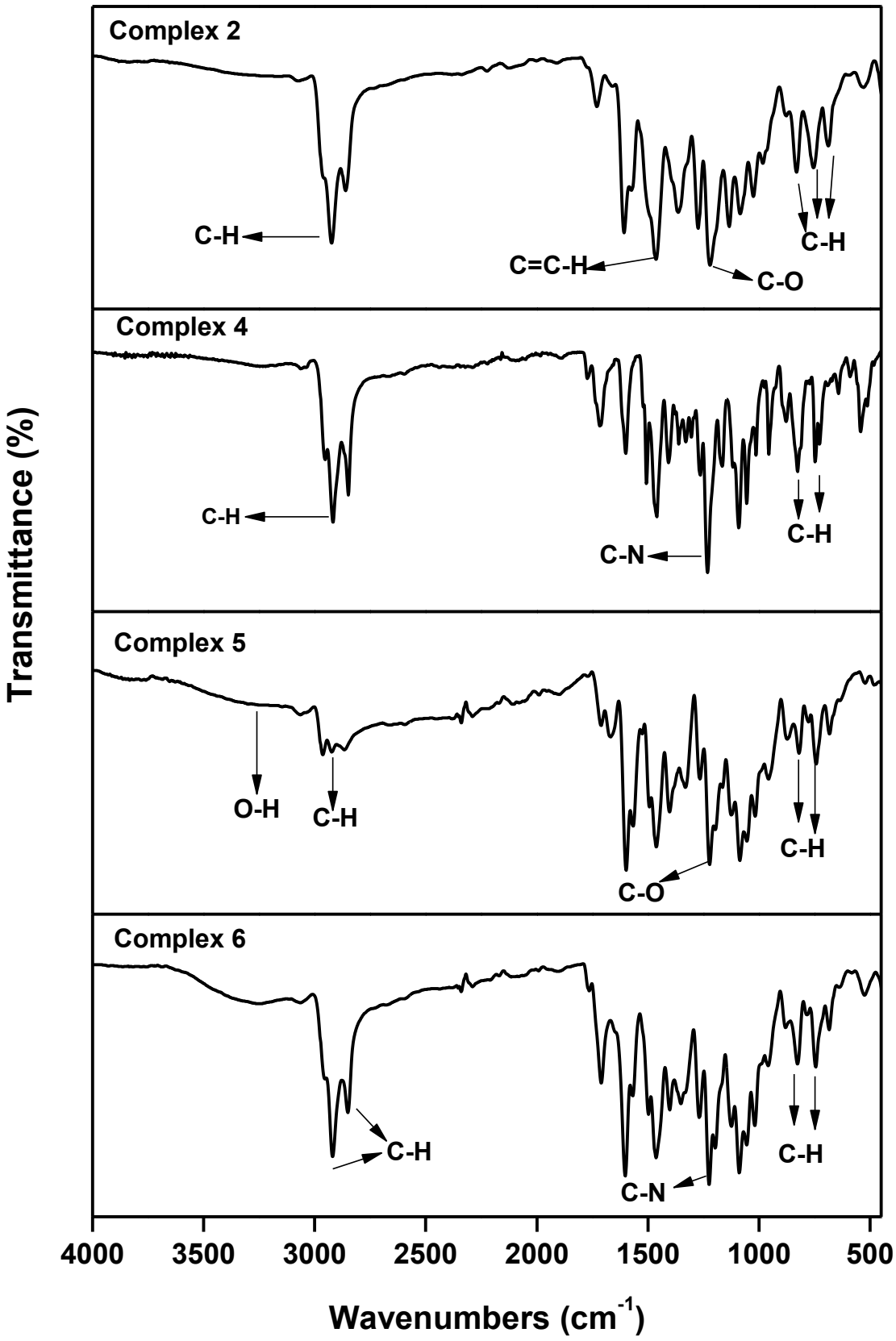

Fig. 3.7: FT-IR spectra of the newly synthesized complexes.

Fig. 3.8A provides the UV–Vis spectra of complexes **3-6** as examples. A monomeric Q band assigned to metallated Pcs is observed in all the complexes (**1-6**, **Table 3.2**). The Q bands appear at 676, 688, 670, 673, 667 and 676 nm for complexes **1**, **2**, **3**, **4**, **5** and **6** respectively (see **Table 3.2** for Q band maxima).

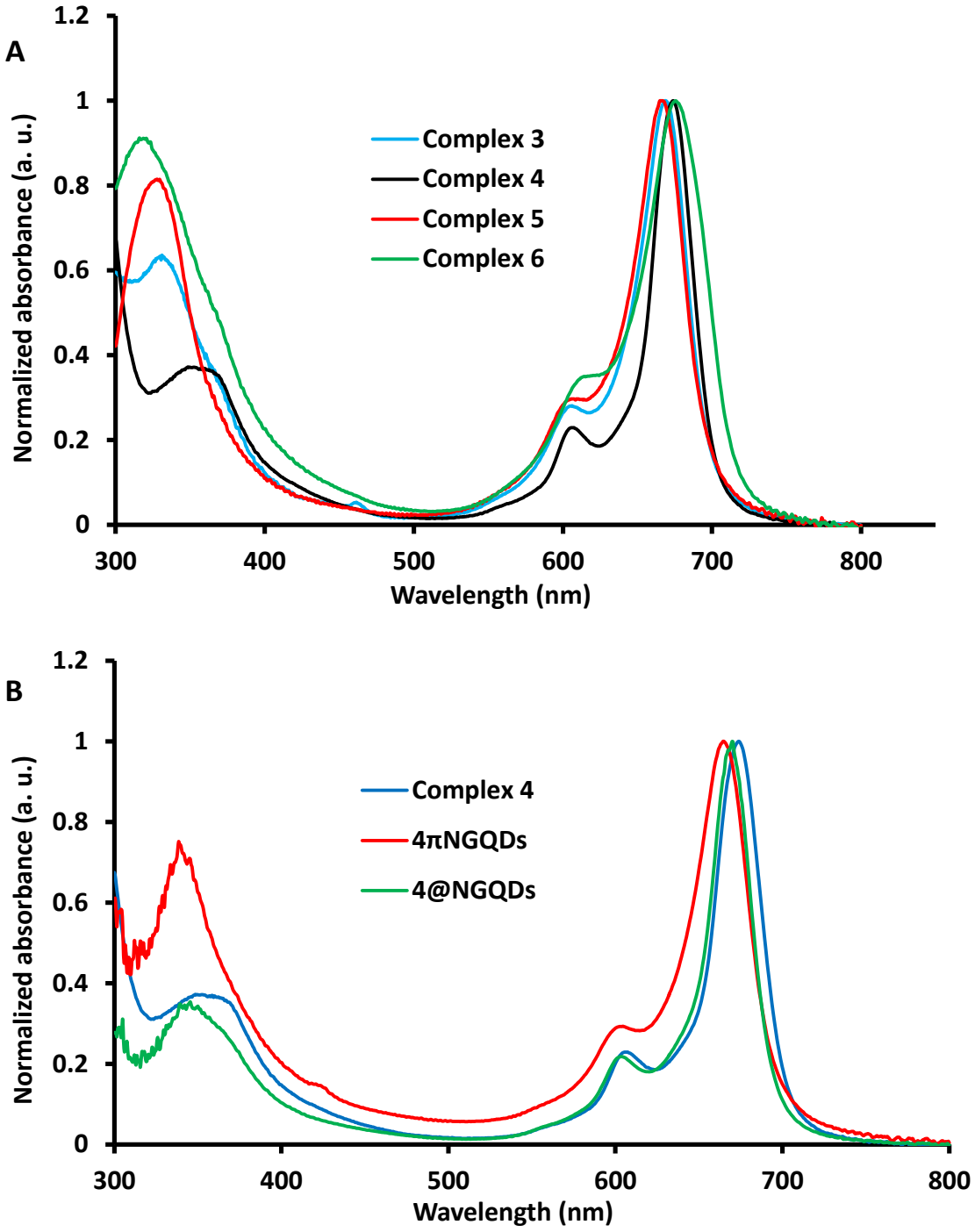

Fig. 3.8: Absorption spectra of the asymmetric complexes (**A**) and that of complex **4** with its π-stacked and covalently linked conjugates (**B**). All in DMF (~10^{-6} M).

In comparing all six complexes, it can be seen from **Fig. 3.8A** (**3**-**6** shown as examples) and **Table 3.2** that the Q bands for complexes **3** and **5** are the least redshifted in comparison to complexes **1, 2, 4** and **6**. Notably so, complexes **3** and **5** are those that consist of a COOH-bearing substituent. With respect to the asymmetric complexes, this observation may lend to the theory that electron donating groups such as a primary amine induces redshifts in the Q band hence complexes **4** and **6** are more redshifted compared to complexes **3** and **5** [**47**]. Complex **2** exhibits the greatest redshift of all which may be attributed to the central metal, iron.

The thermogravimetric analysis of the complexes (**1**-**6**) was carried out in a nitrogen atmosphere from 50 °C to 800 °C. From the results obtained, with the exception of complex **3**, the asymmetrical complexes (**4**-**6**) exhibit greater thermal stability than the symmetrical Pcs, complexes **1** and **2**. An initial mass loss of 1 – 2 % attributed to the loss of free moisture was observed at 80 – 190 °C while the complexes lost approximately 50% of their starting mass at 380 – 623 °C. From the thermograms obtained (Complexes **1**-**4** used as examples in **Fig. A5**), the order of thermal stability is as follows: **6**>**5**>**4**>**1**>**2**>**3** where complexes **1**-**6** recorded initial decomposition temperatures of 273, 226, 200, 352, 366 and 395 °C respectively. All complexes lost more than 80 % of their initial mass upon completion of the analysis.

The elemental analyses (CHN) conducted were in good agreement regarding the calculated percentages of carbon, hydrogen and nitrogen in the samples presented. Furthermore, for complex **5**, it was consistent with other findings where some Pcs are isolated as hydrates [**151**]. Nuclear magnetic resonance (NMR) spectroscopic studies were not performed due to the paramagnetic nature of the central metals, cobalt and iron.

3.3 Characterization of conjugates

The binding of Pcs to the GQDs through π-π stacking is achieved with great ease since GQDs contain planar monolayer sheets of graphene; hence the complexes (**3**-**6**) were π-π stacked onto the GQDs as shown in **Scheme 3.2A**. The covalently linked conjugates were obtained

by activating the carboxylic acid on the GQDs using EDC and NHS (**Scheme 3.2B**), followed by linking to the NH_2 group of complexes **4** and **6**.

A

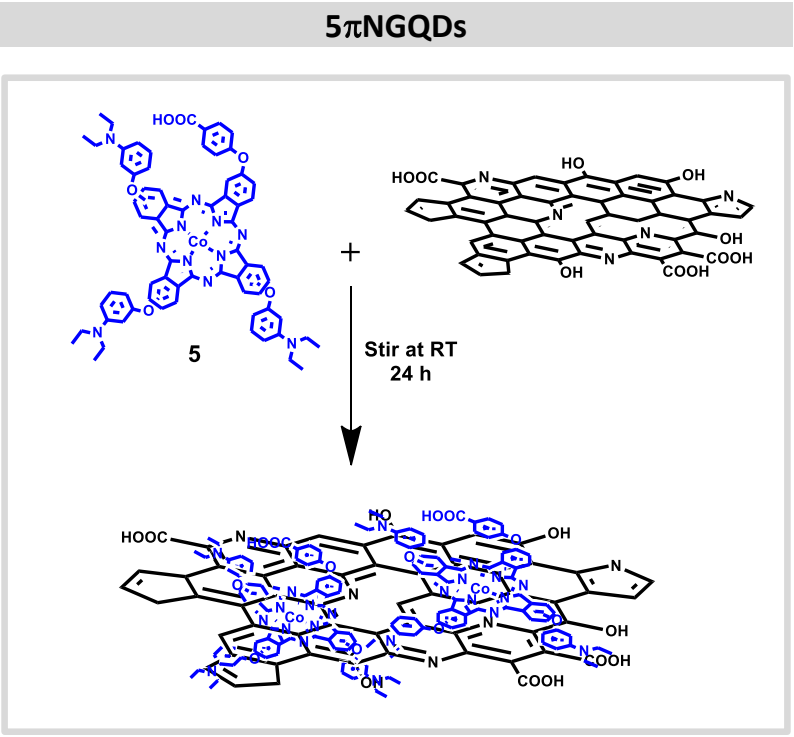

B

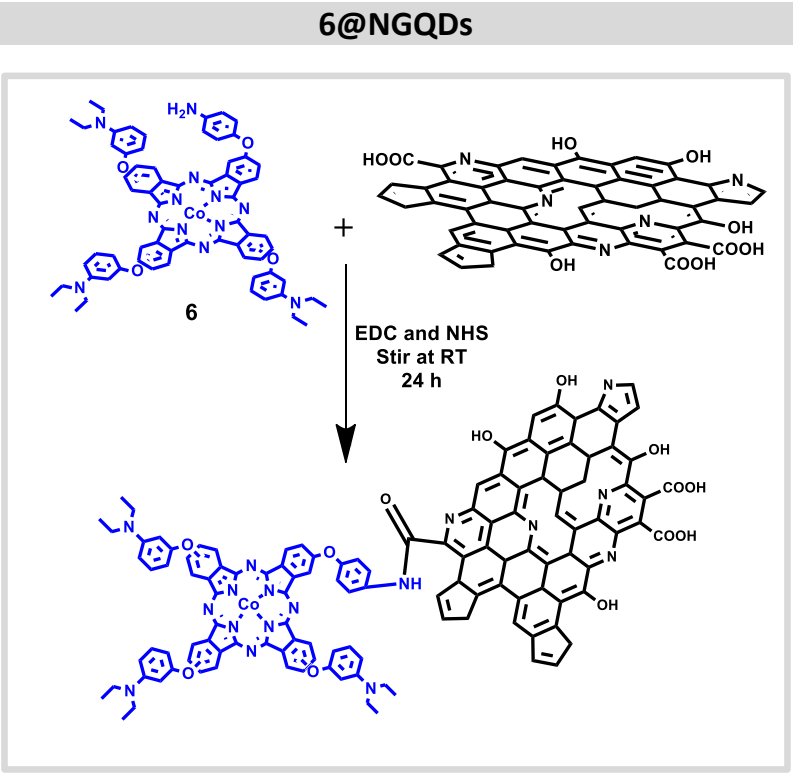

Scheme 3.2: An illustration of how the π-π stacked conjugates and the covalently linked conjugates were prepared. (**A** – π-π stacking; **B** – covalent linking).

3.3.1 UV-vis spectroscopy

The loading of the Pc onto the GQDs was estimated following literature methods [**152**] using the absorption spectra. This involves comparing the Q band absorbance intensity of the Pc in the conjugate with that of the initial Pc before the conjugation. The loading of Pc onto GQDs is shown in **Table 3.2**. Covalently linked complexes **4** and **6** show slightly smaller loading compared to their corresponding non-covalently linked derivatives. The lowest loading is obtained for **3**πNGQDs.

Table 3.2 shows a general blue shift in the Q band of the Pcs following conjugation to GQDs. The Q band absorption of Pcs is sensitive to π-π interactions. It has been reported that the strong π-π attraction leads to the formation of ground state complexes between Pcs and carbon nanomaterials, resulting in spectral shifts [**153**]. Apart from the blue shifting, there were no changes in the Q band (except for broadening for **4**πGQDs), **Fig. 3.8B**. This shows that the Pc remains intact in the conjugate. There was also no change in the oxidation state of the central metal since a sharp band associated with Co^{I}Pc derivatives was not observed in the region lying between the Q and B bands, nor was there a redshift in the Q band which is often ascribed to Co^{III} [**154**]. Thus the central metal remains in the Co^{II} state for the electrocatalytic oxidation studies.

Red shifts and flattening of similar macrocycles such as porphyrins have been observed in porphyrins-graphene oxide nanoconjugates [**155**]. Blue shifts in UV-Vis spectra have also been reported for porphyrin-graphene oxide conjugates and were attributed to strong interactions between the two layers [**156**]. Thus the blue shifts observed for the CoPc derivatives in the presence of GQDs suggest strong interaction between the two. There is a higher blue shift for the π-π conjugated composites than for covalently linked in **Table 3.2**, thus suggesting interaction and formation of layers for the former. Covalent linking occurs mainly on the edges with possible π-π interaction depending on the orientation, hence less interaction between Pcs and GQDs.

3.3.2 Raman spectroscopy

Raman spectroscopy suggests that there have been changes made to the graphene framework. The D band shifts while the G band remains constant following conjugation (**Fig. 3.9)**. Shifts in the D band have been reported to indicate a strong interaction between the porphyrins and the graphitic sheets due to a charge transfer [**157**]. It has been reported that tensile strain induces red shift in graphene (as observed for **6**πGQDs) and compression causes blue shifts (observed for **6**@GQDs) [**158**]. Thus, different types of coordination affect the GQDs differently, but the CoPcs remain intact.

An assumption that can be made by looking at the changes of the D and G bands in the non-covalently linked conjugates is that the changes are a result of the substituents assuming positions that result in strain being placed onto the bonds that make up the graphene network.

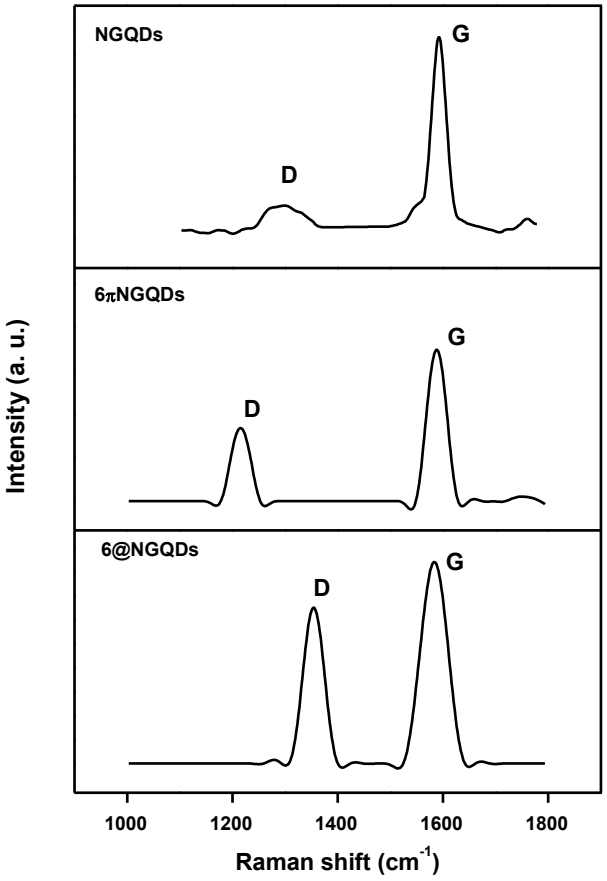

Fig. 3.9: Raman spectra illustrating the changes in the D and G bands of NGQDs, **6**πNGQDs, and **6**@NGQDs.

The I_D/I_G ratios calculated further support the discussion above where increments in the ratios are observed. The NGQDs on their own are highly ordered with an I_D/I_G ratio of 0.16. Upon conjugating through π-π stacking, the general order of the graphene framework is disrupted hence an increase in the I_D/I_G ratio, **Table 3.2**. There is an increase in I_D/I_G ratio of NGQDs in the presence of Pcs in all cases (**Table 3.2**). It is generally expected that π-π conjugation will result in a lower I_D/I_G ratio since it is not affecting the GQDs structure as much as covalent bonding. This is the case for **6**@NGQDs compared to **6**πNGQDs where the I_D/I_G ratio is higher for the covalently linked conjugate. For **4**@NGQDs compared to **4**πNGQDs, the former surprisingly shows a higher I_D/I_G ratio compared to the latter. A decrease in the I_D/I_G ratio suggests reduction in defects, or enhanced order [**157**].

3.3.3 Dynamic light scattering/TEM

The average particle size for the NGQDs and their respective conjugates was determined through dynamic light scattering (DLS). The NGQDs on their own had an average diameter of 1.7 nm and upon conjugation; there was approximately a thirty-fold increase in the particle size. The sizes of both the covalently linked and π-π stacked conjugates ranged from between 25 and 40 nm (**Fig. 3.10**). These values however, are not a true representation of one individual conjugate as such complexes are prone to forming clusters because of the high electron density the materials possess. The increase in size may be due to aggregation caused by the interactions between the Pcs on adjacent NPs via π-π stacking as Pcs are known to π-π stack resulting in the formation of H aggregates [**154**]. In addition to that, DLS sizes are known to be larger than those obtained by other techniques due to interference of the dispersant into the hydrodynamic diameter, resulting in shifts to higher values [**159**]. The TEM images (not shown) also exhibited aggregated particles.

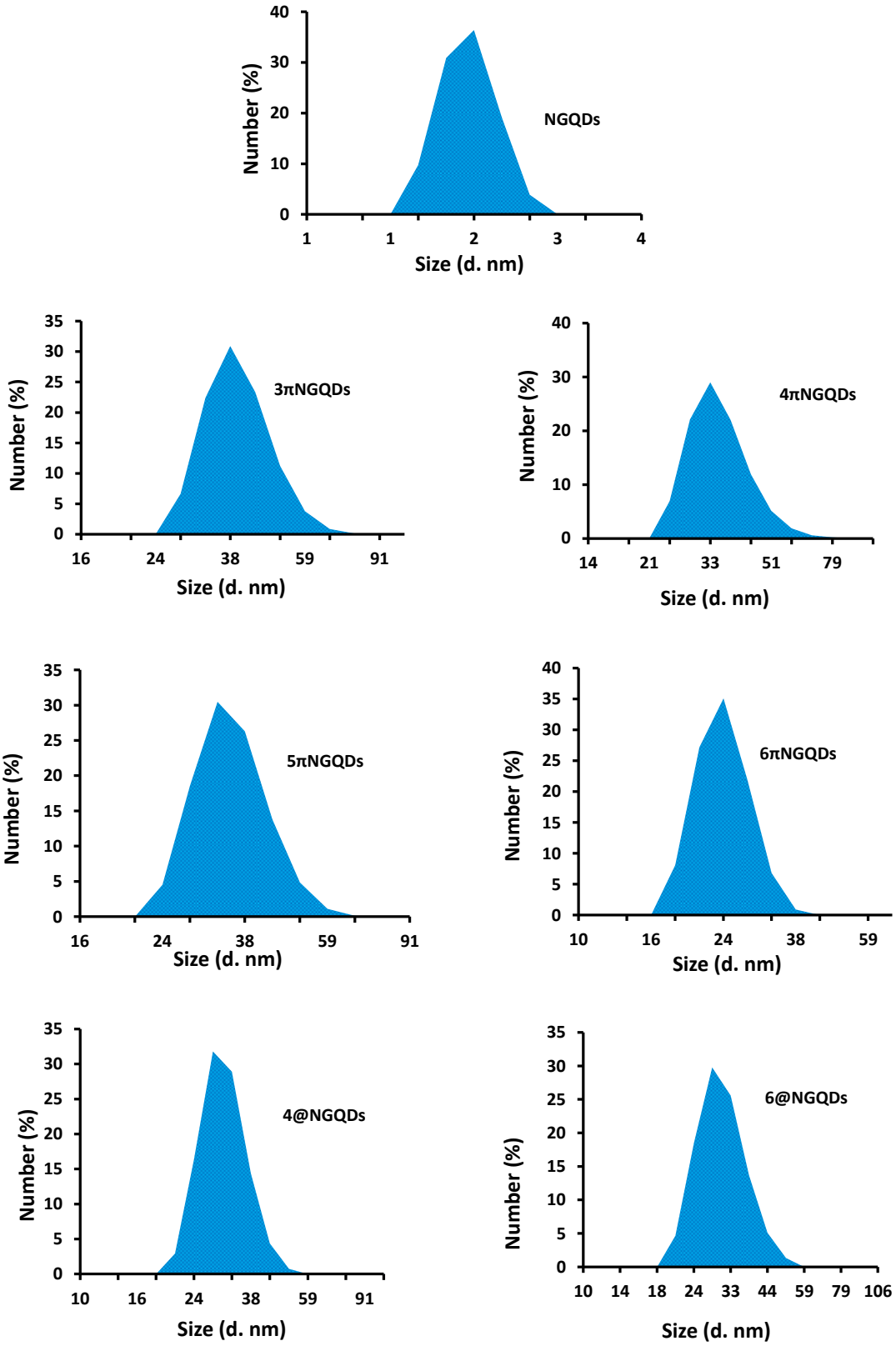

Fig. 3.10: DLS area plots illustrating the average particle sizes for the NGQDs and their conjugates with the asymmetrical complexes.

Table 3.2: A summary of the changes observed following conjugation between the NGQDs and the complexes. (*All absorption spectra in DMF*).

Complex/ nanomaterial	Q band (nm)	DLS size (nm)	Pc loading (mg Pc /mg GQDs)	Raman I_D/I_G ratio
NGQDs	-	1.7	-	0.16
1[a]	676	-	-	-
2[a]	688	-	-	-
3	670	-	-	-
3πNGQDs	664	40	0.62	0.63
4	673	-	-	-
4πNGQDs	665	36	0.88	0.75
4@NGQDs	669	31	0.83	0.33
5	667	-	-	-
5πNGQDs	665	36	0.84	0.81
6	676	-	-	-
6πNGQDs	669	25	0.84	0.52
6@NGQDs	675	31	0.78	0.91

[a] sequential modifications, no loading.

3.3.4 FT-IR

Fourier transform infrared spectroscopy revealed the changes brought by the conjugation through shifts in wavenumbers of associated functional groups, particularly the non-covalently linked conjugates as well as the emergence of new stretching frequencies in the covalently linked conjugates illustrating that new bonds (-N-(C=O)-) have been formed between the two nanomaterials (**Fig. 3.11**).

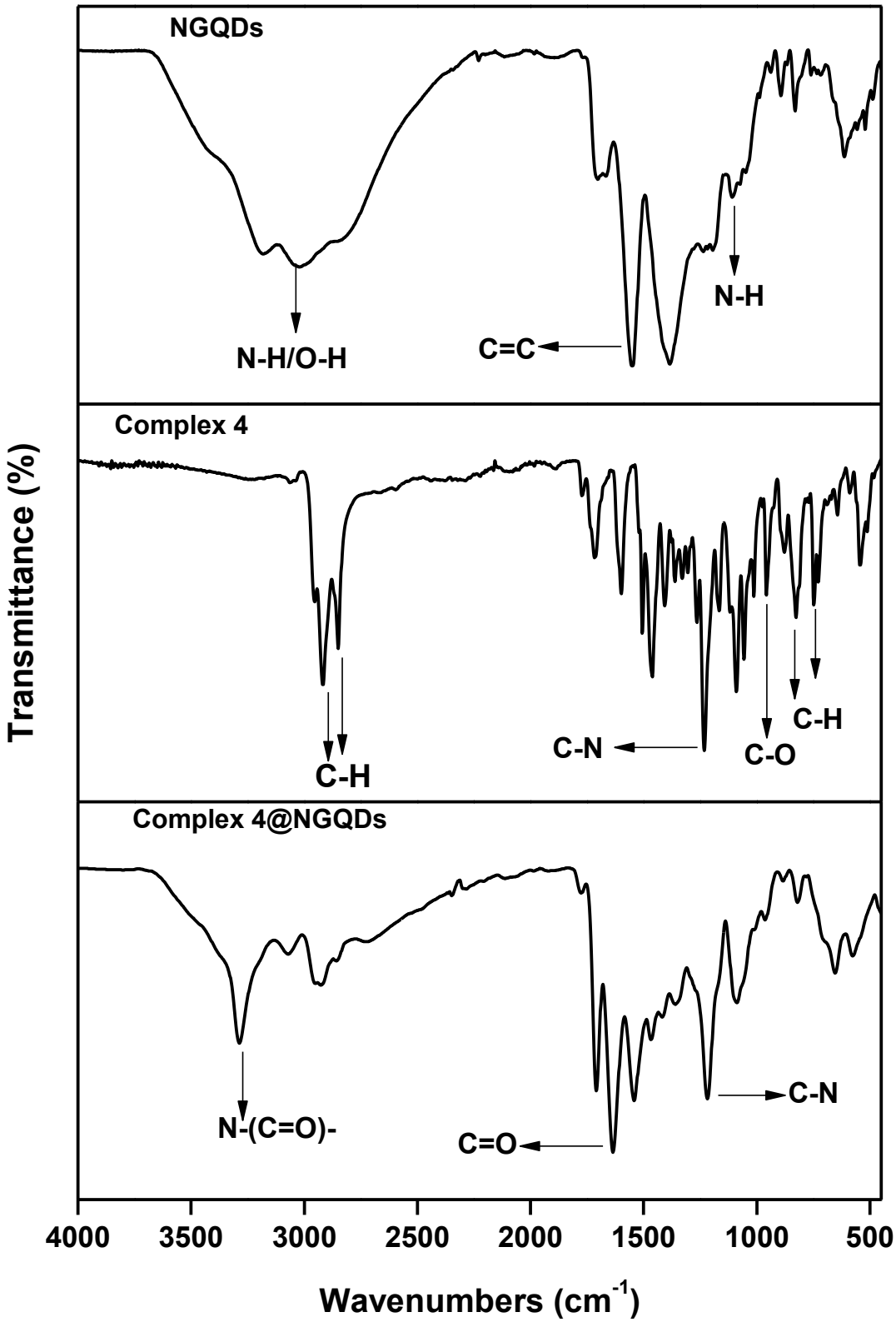

Fig. 3.11: FT-IR illustrating the emergence of new stretching frequencies upon linking the NGQDs to complex **4** with the use of an amide bond.

3.3.5 X-ray photoelectron spectroscopy (XPS)

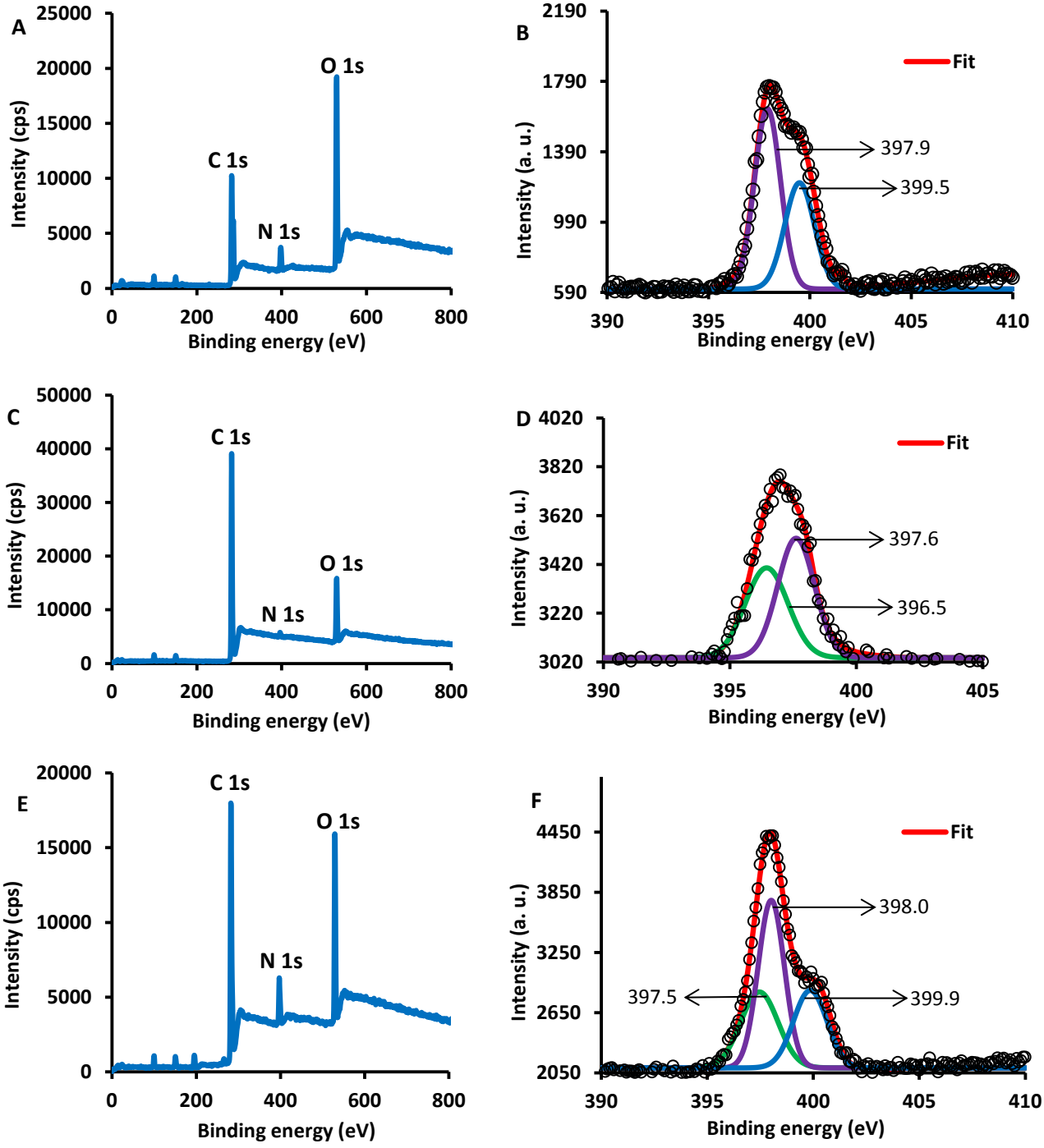

Fig. 3.12: XPS wide scans for the NGQDs (**A**), complex **6** (**C**) and **6**@NGQDs (**E**). High resolution N 1s XPS spectra for NGQDs (**B**), complex **6** (**D**) and **6**@NGQDs (**F**).

In order to supplement the IR data, XPS was used to further confirm the formation of the amide bond between the NGQDs and the complexes. **Fig. 3.12A** and **3.12C** are the wide

scans for NGQDs and complex **6**, respectively, while **Fig. 3.12E** is that of the composite formed through covalent linking. NGQDs and complex **6** contain both carbon and oxygen in seemingly large quantities as implied by the wide scan. With respect to the atomic concentration of nitrogen within the molecules, the quantitative analysis revealed that complex **6** has 1.13%, NGQDs have 6.94% and **6**@NGQDs has a slightly higher value of 7.51%, due to the presence of both NGQDs and the Pc in the latter.

The high resolution spectrum of the NGQDs was deconvoluted to two peaks with that giving its maxima at a binding energy of 397.9 eV being assigned to the pyridinic nitrogen atoms and the other producing its peak intensity at 399.5 eV being assigned to the pyrrolic nitrogen atoms (**Fig. 3.12B**). The deconvolution of complex **6** also yielded two peaks at 396.5 eV and 397.6 eV with the former being attributed to pyridinic nitrogen atoms and the latter to graphitic nitrogen (**Fig. 3.12D**). **Fig. 3.12F** was resolved to three peaks with the one appearing at 397.5 eV being assigned to the pyridinic nitrogen, the one at 398.0 eV attributed to the graphitic N and the occurrence of one at a binding energy of 399.9 eV being assigned to that of a nitrogen bound to a carbonyl confirming the formation of the amide bond.

3.4 Summary of chapter

Various spectroscopic and non-spectroscopic techniques were involved in the characterization of the synthesized complexes and their corresponding conjugates. All the techniques employed complemented each other in confirming that indeed the desired complexes and their respective nanocomposites through both covalent and non-covalent interactions had been formed.

Chapter 4

Electrode characterization

Characterization of the modified electrodes in a redox probe and in the buffers employed is discussed in this chapter.

4.1 Characterization in ferrocyanide-ferricyanide

4.1.1 Cyclic voltammetry (CV)

The manner in which the electrodes were modified is described in chapter 2. Following modification, the prepared electrodes were characterized using cyclic voltammetry (CV) with a ferrocyanide-ferricyanide ($[Fe(CN)_6]^{3-/4-}$) solution as the redox mediator. The aforementioned redox probe was not only selected entirely based on availability and cost but mostly because it is stable and highly reversible [**160**]. In addition to these traits, this particular probe is highly sensitive to the surface kinetics of the glassy carbon electrode which was employed in this work [**161**].

Inferences on the electron-transferring abilities of an electrode can be made by looking at the cathodic and anodic peak potential separation (ΔE_p) where a value of 60 mV or close to the Nernstian value implies exceptional movement of electrons. However, it cannot be deduced from large ΔE_p values or the absence of a redox signal as to how an analyte will respond towards the electrocatalyst as the $Fe^{3+/2+}$ redox process is highly affected by oxides on the electrode surface and responds poorly in their absence (i.e. electrode modification) [**161**]. **Table 4.1** provides a summary of the ΔE_p values of the probes that were studied with an assortment of the corresponding cyclic voltammograms in 1 mM $[Fe(CN)_6]^{3-/4-}$ in 0.1 M KCl presented in **Fig. 4.1**.

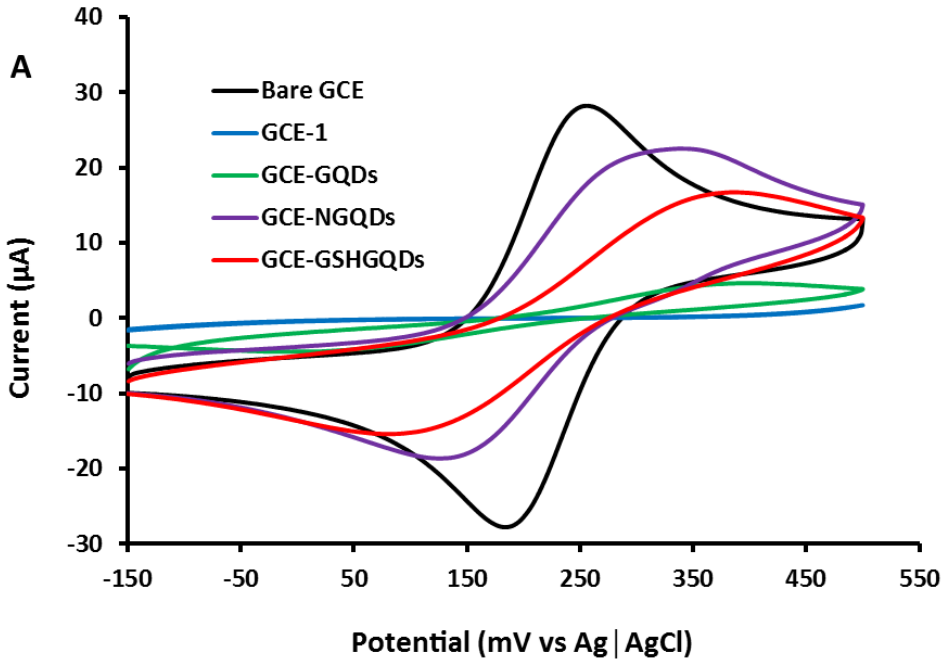

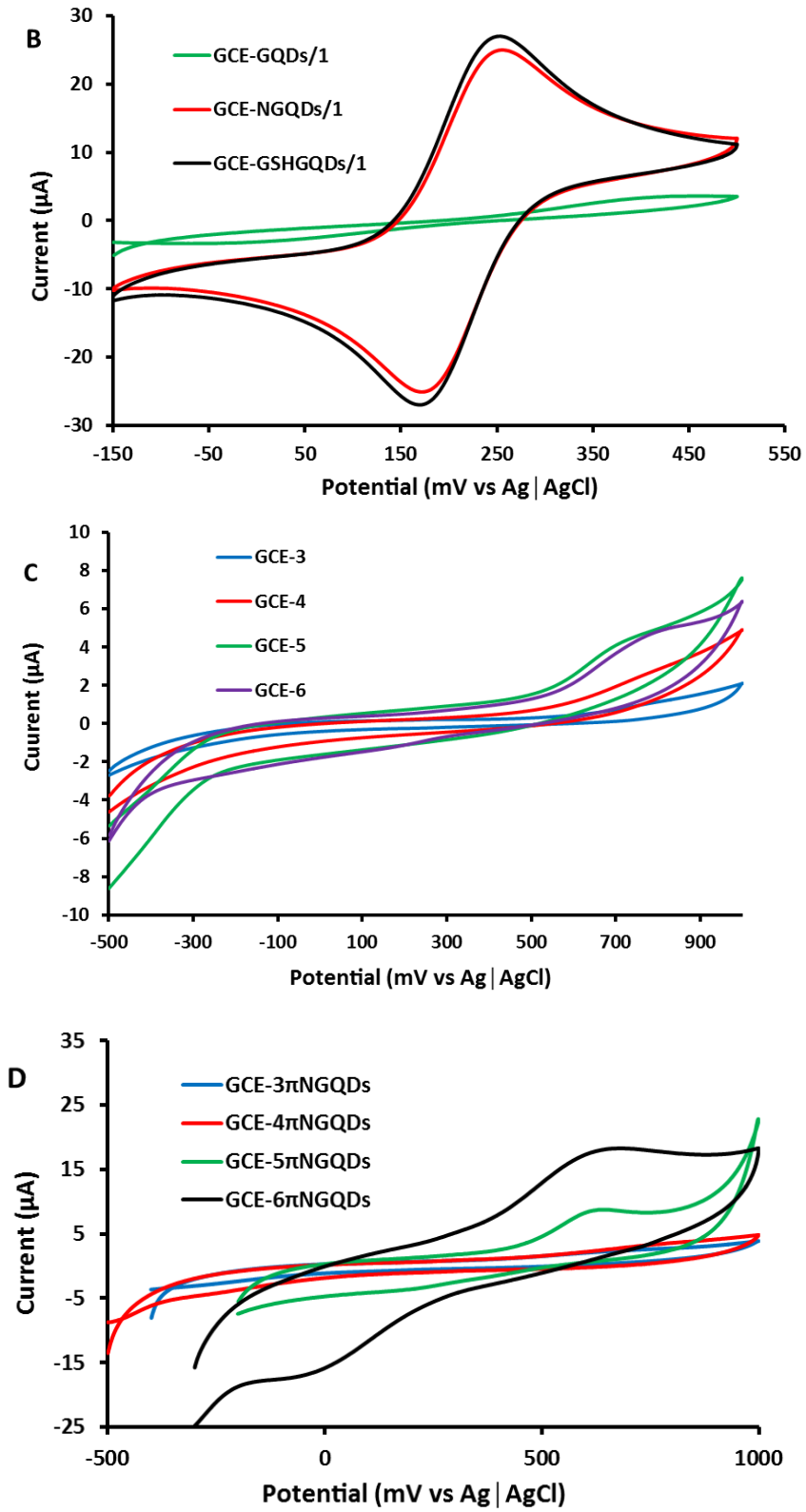

Fig. 4.1: Cyclic voltammograms of the bare and modified electrodes in 1 mM $Fe(CN)_6^{3-/4-}$ (in 0.1 M KCl). (**A** and **C** – single modifications; **B** – sequential modifications; **D** – π-π stacked conjugates).

Table 4.1: ΔE_p values for all modified electrodes in a ferrocyanide-ferricyanide solution.

Probe[a]	**ΔE_p (mV) (vs Ag|AgCl) $Fe(CN)_6^{3-/4-}$**
Bare GCE	66
GCE-GQDs	365
GCE-NGQDs	187
GCE-GSHGQDs	289
GCE-**1**	a
GCE-**1**/GQDs	a
GCE-**1**/NGQDs	84
GCE-**1**/GSHGQDs	89
GCE-GQDs/**1**	395
GCE-NGQDs/**1**	80
GCE-GSHGQDs/**1**	78
GCE-NGQDs/**2**	a
GCE-**3**	a
GCE-**3**πNGQDs	422
GCE-**4**	a
GCE-**4**πNGQDs	523
GCE-**4**@NGQDs	471
GCE-**5**	717
GCE-**5**πNGQDs	435
GCE-**6**	641
GCE-**6**πNGQDs	620
GCE-**6**@NGQDs	74

a – no redox response

From **Table 4.1**, with respect to the symmetrical complexes and their combination with the GQDs through sequential modifications, the following can be outlined:

- The bare GCE gave a value of ΔE_p = 66 mV close to the Nernstian value corresponding with good electron transfer kinetics for the $[Fe(CN)_6]^{3-/4-}$ redox couple. This is also indicative of a clean GCE.

- Considering the GQDs alone, GCE-NGQDs shows better electron transfer kinetics with the lowest ΔE_p value.

- In terms of the sequential modifications where complex **1** is placed on top of the GQDs, there is better electron transfer than when **1** is placed first on the electrode.

    - A redox signal was not observed for GCE-NGQDs/**2**.

- In the presence of GSHGQDs or NGQDs whether **1** is placed first or not, low ΔE_p values (which are close to the Nernstian value) are obtained indicating good electron transfer kinetics for the $[Fe(CN)_6]^{3-/4}$.

- Complex **1** in the presence of pristine (undoped) GQDs results in very large ΔE_p value (~400 mV, GCE-NGQDs/**1**), showing that undoped GQDs hinder electron transfer.

- GCE-**1** alone gave no peaks suggesting poor electron transfer behaviour.

The observations made are proof that the combination of NGQDs and GSHGQDs with a Pc results in good electron transfer ability at the electrode surface. To further support this statement, asymmetrical Pc complexes were prepared and coupled with the NGQDs through π-π stacking and covalent linking as the NGQDs produced the most favourable results in comparison to the other GQDs. Following characterization with CV, the following summary can be made regarding the asymmetrical complexes and their respective conjugates (**Table 4.1**):

- Overall, GCE-**6**@NGQDs has the best electron transferring ability, close to that of the bare GCE.

- Looking at the CoPc complexes alone, GCE-**6** is the best followed by GCE-**5**. No redox peaks were obtained for GCE-**3** and GCE-**4** even at lower scan rates.

- For the non-covalently linked conjugates, the electron transfer abilities improve as follows: GCE-**3**πNGQDs > GCE-**5**πNGQDs > GCE-**4**πNGQDs > GCE-**6**πNGQDs. The best performing electrodes are those containing complexes **3** and **5** (GCE-**3**πNGQDs and

GCE-**5**πNGQDs) containing push-pull substituents. As stated above push-pull substituents enhance electron transfer properties of complexes.

- For the covalently linked conjugates, GCE-NGQDs@**6** is better than GCE-NGQDs@**4** and the reason for that may be that *tert*-butyl groups in GCE-NGQDS@**4** make it more difficult for the Pc ring to rest closer to the electrode surface in comparison to the diethylamino groups in GCE-NGQDs@**6**.

The nature of the substituents and how they are positioned on the electrode surface may be the cause for such high ΔE_p values hence the decline upon conjugation to the NGQDs as they are of a planar nature.

4.1.2 Scanning electrochemical microscopy (SECM)

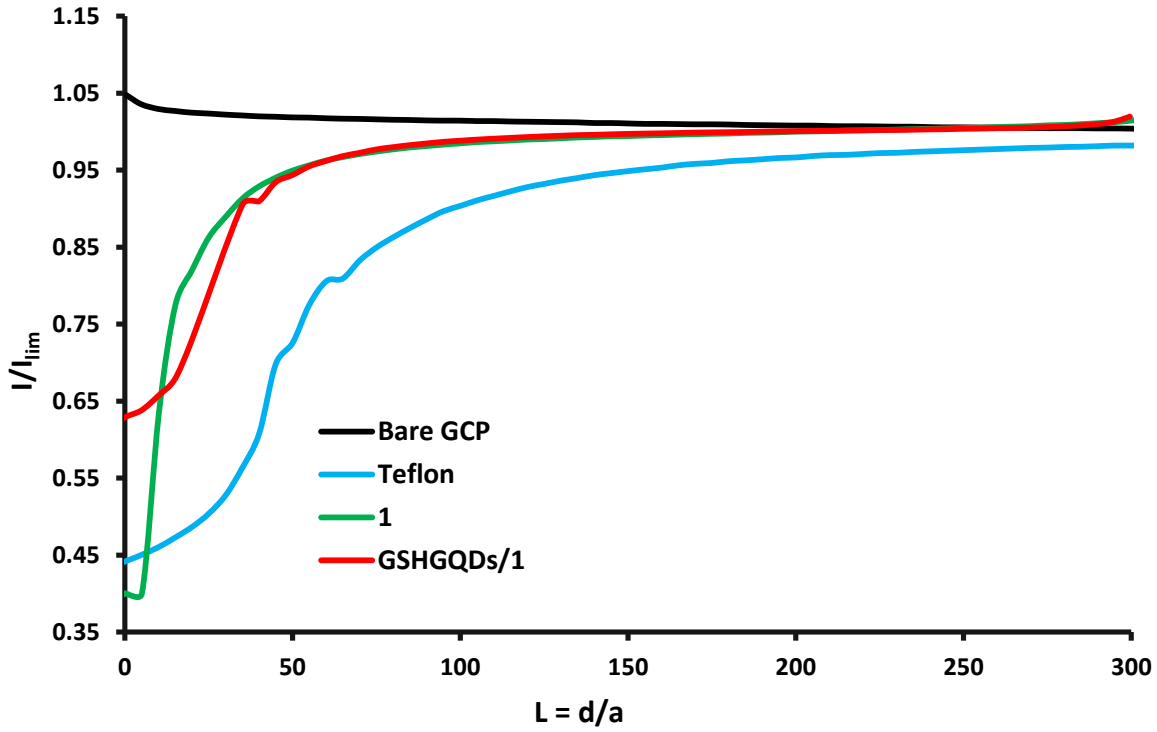

Fig. 4.2: Approach curves of probes investigated in 5mM $[Fe(CN)6]^{3-}/^{4-}$ in 0.1 M KCl. Inset: Resolved Bare glassy carbon plate approach curve. (L = d/a represents the ratio of tip-substrate to UME tip radius).

The approach curves in SECM show changes in tip current as the ultra-micro electrode (UME) tip approaches the surface in a feedback mode experiment facilitated by a Fe^{3+}/Fe^{2+}

redox mediator. The approach curves obtained through SECM indicate that the probes are insulators based on the general progression of the curves (**Fig. 4.2**), as is the case for Teflon. Similar observations have been made before where GQDs and a phthalocyanine were combined [**74**]. The lowest current is registered for the Teflon while the differences between the probes on the modified glassy carbon plates are of a small magnitude. The bare glassy carbon plate (GCP) is of a conductive nature hence the trajectory of the approach curve (**Fig. 4.2 inset**).

4.2 Characterization in the blank solution

Blank scans in the buffer solution/aqueous medium employed were recorded to aid in discerning how the modified electrodes behave in the absence/presence of the analyte. This was done to ensure that the signals observed are correctly assigned to the analyte and that the buffer solutions/aqueous media themselves are free of contaminants which may interfere with the signal produced upon the addition of the analyte. **Fig. 4.3A** consists of voltammograms in a phosphate buffer solution (PBS, pH 7) while **Fig. 4.3B** are the blank voltammograms in 0.1 M NaOH. Two different media are illustrated because one was used to facilitate the electrochemical sensing of nitrite (PBS) while the other was used for hydrazine (0.1 M NaOH).

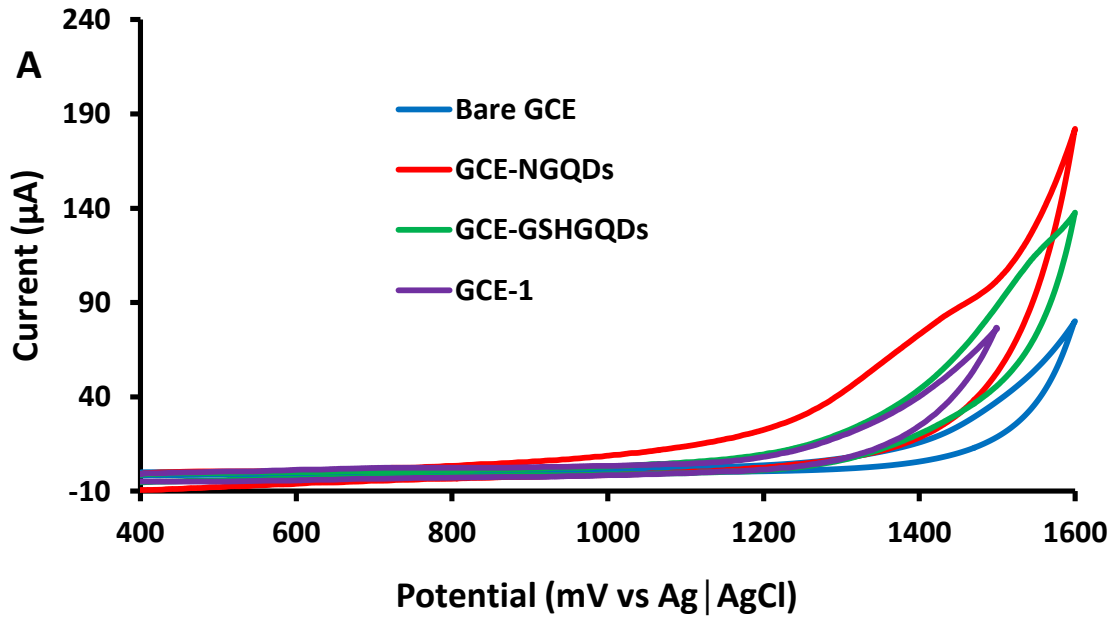

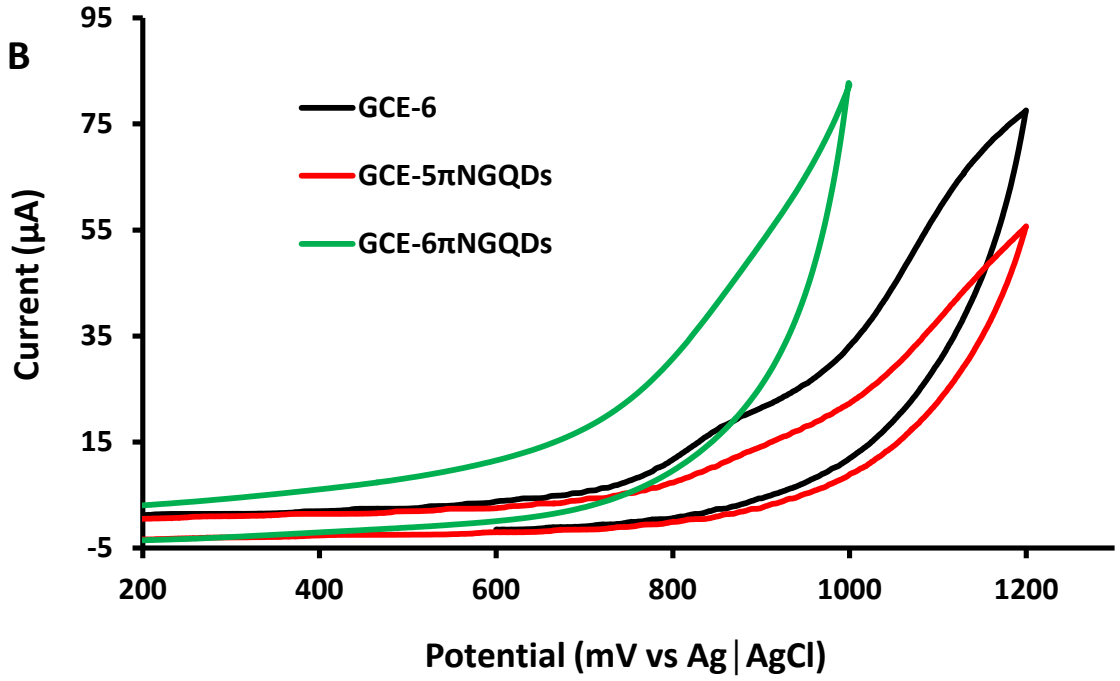

Fig. 4.3: Cyclic voltammograms of the modified electrodes in (**A**) PBS, pH 7 and (**B**) 0.1 M NaOH.

As illustrated above (**Fig. 4.3A**), with the exception of GCE-NGQDs, there is very little activity happening between the PBS solution and the electrodes hence there are no peaks associated with either reduction or oxidation within the potential window for the oxidation of nitrite to occur. The blank CV scans in 0.1 M NaOH are shown in **Fig. 4.3B**. Similar to the PBS solution, no reduction or oxidation peaks were observed for the modified electrodes with the exception of GCE-**6** (**Fig. 4.3B**). CoPcs have been reported to exhibit redox processes in solutions where the pH is 7 (Co^{III}/Co^{II} close to 0 mV) [**162**] however in this instance, this was not observed with the oxidation peak appearing at approximately 860 mV for GCE-**6** being the result of a ring-based process (**Fig 4.3B**).

4.3 Summary of chapter

Looking at all the modified electrodes, it appears that the sequential modifications, with the exception of GCE-GQDs/**1**, offer better electron movement than the asymmetric Pcs and their conjugates (**Table 4.1**). Regarding the asymmetric complexes, complex **6** in its

covalently linked form, GCE-**6**@NGQDs, is the only one with a low ΔE_p value hence it can be assumed that it enables the swift movement of electrons.

Chapter 5

Electrochemical sensing

Studies on the electrocatalytic oxidation of nitrite and hydrazine are discussed in this chapter.

5.1 Electrocatalytic oxidation of nitrite

5.1.1 Comparative cyclic voltammograms

Cyclic voltammetry (CV) was used to analyse the electrochemical responses of the modified GCE in the presence of 2.5 mM of nitrite in PBS (pH 7), **Fig. 5.1**. Of importance to note, sequential modifications were adopted in the preliminary study to establish which GQDs perform best so that they can be applied in further studies.

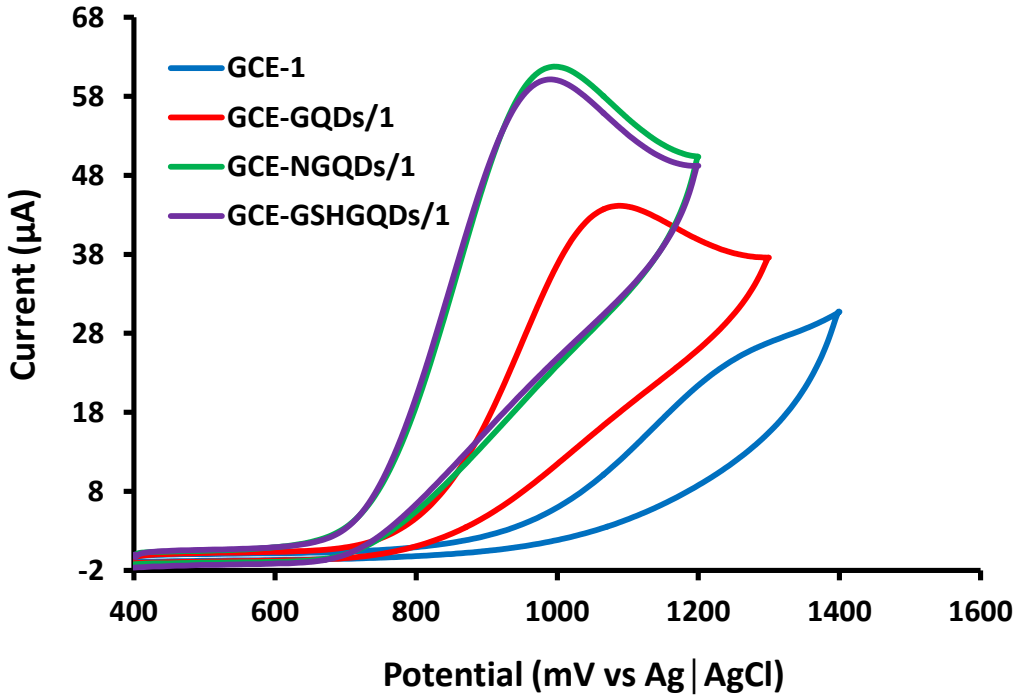

Fig. 5.1: Cyclic voltammograms of selected modified electrodes in the presence of 2.5 mM of nitrite in PBS (pH 7).

Fig. 5.1 shows a selection of comparative cyclic voltammograms of the GCE modified with the GQDs doped with various heteroatoms as well as complex **1** and how they respond in the presence of 2.5 mM of nitrite. The catalytic activity of the probes can be determined by looking at both the position of the catalytic peak potential as well as the intensity of the catalytic peak current. Ideally, signs of a good electrocatalyst include the ability to produce low oxidation potentials and high catalytic currents upon making contact with the analyte.

From the values of the nitrite oxidation potential shown in **Table 5.1**, the following conclusions can be made:

- For the GQDs alone, the GCE-GSHGQDs have the lowest oxidation potentials than the other GQDs.
- Doping of the GQDs results in lowering of the oxidation potential for complex **1** where the GSHGQDs perform the best, followed by the NGQDs, showing the importance of doping GQDS.
- When complex **1** is placed on top of all the GQDs, the potential for oxidation of nitrite is more favourable when complex **1** is placed first. This can be attributed to the orientation that the molecules assume on the electrode surface; GQDs are more likely to assume a flat position unlike the complexes because of the substituents.
- Complex **1** alone performs worse than when in the presence of the GQDS, showing the general importance of GQDs in the electrocatalytic behaviour of the Pc.
- Complex **2** paired with the NGQDs performed better than complex **1** for the same order in sequential modification.

Table 5.1: Summary of data for the electro-oxidation of nitrite acquired from the cyclic voltammetry (*all for 2.5 mM nitrite at a scan rate of 50 mV/s*).

Probe[a]	**E_p (mV) vs. Ag|AgCl**	**Background corrected I_p (µA)**	**Tafel slope (mV decade^{-1})**
GCE-GQDs (1.4 nm)	987	51.5	215
GCE-NGQDs (2.4 nm)	988	61.3	185
GCE-GSHGQDs (2.8 nm)	940	64.5	230
GCE-**1**	1230	15.2	103
GCE-**1**/GQDs	1198	30.9	138
GCE-**1**/NGQDs	1164	41.5	128
GCE-**1**/GSHGQDs	1081	36.1	310
GCE-GQDs/**1**	1070	32.4	163

GCE-NGQDs/**1**	990	53.4	205
GCE-GSHGQDs/**1**	983	53.6	180
GCE-NGQDs/**2**	940	54.4	119

[a] sizes obtained from TEM, chapter 3

In terms of the current, the following observations can be made (**Table 5.1**):

- GCE-GSHGQDs produced the largest current while GCE-**1** gave the lowest catalytic current.
- In the presence of complex **1**, the doped GQDs produced better catalytic currents than the pristine GQDs irrespective of the order of modification.
- Having complex **1** on top of the GQDs yields better results (higher currents) than having it at the bottom.
- Regarding having the complexes follow the NGQDs, complex **2** outperformed complex **1**.

Owing to its instability in ambient conditions, the use of complex **2** was restricted to the one experiment with the NGQDs.

5.1.2 Kinetic studies on electrode-nitrite interactions

The reversibility of the reaction which happens at the surface of the electrode as the analyte comes into contact with the modified GCE was assessed through varying the scan rate at a fixed concentration of nitrite (**Fig. 5.2A**, using GCE-NGQDs/**2** as an example). From **Fig. 5.2A**, it can be seen that an increase in the scan rate results in a shift of the oxidation peak (increase in oxidation potential). This serves to confirm that the reaction happening between the analyte and the modified electrode is of an irreversible nature. This trend was observed for all the probes that were investigated. Furthermore, from this information, by plotting the square root of the scan rate against the current, it was deduced that the nature of the reactions happening on the electrode surface are controlled by diffusion processes (**Fig. 5.2C**)

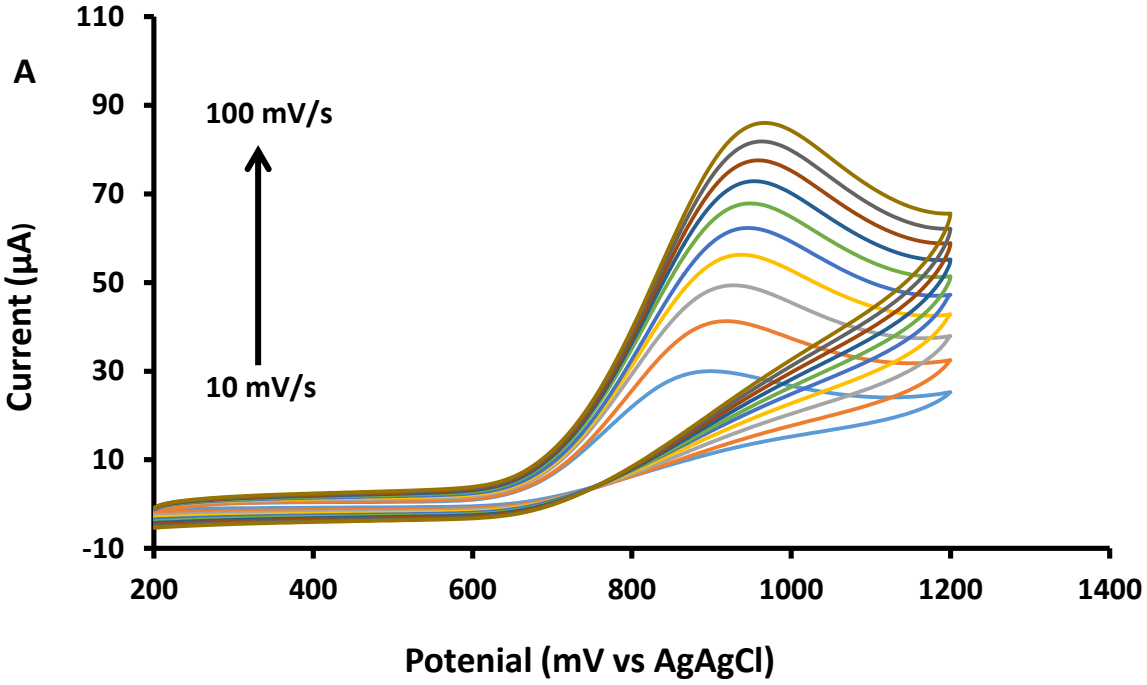
A
100 mV/s
10 mV/s
Current (µA)
110
90
70
50
30
10
-10
200
400
600
800
1000
1200
1400
Potenial (mV vs AgAgCl)

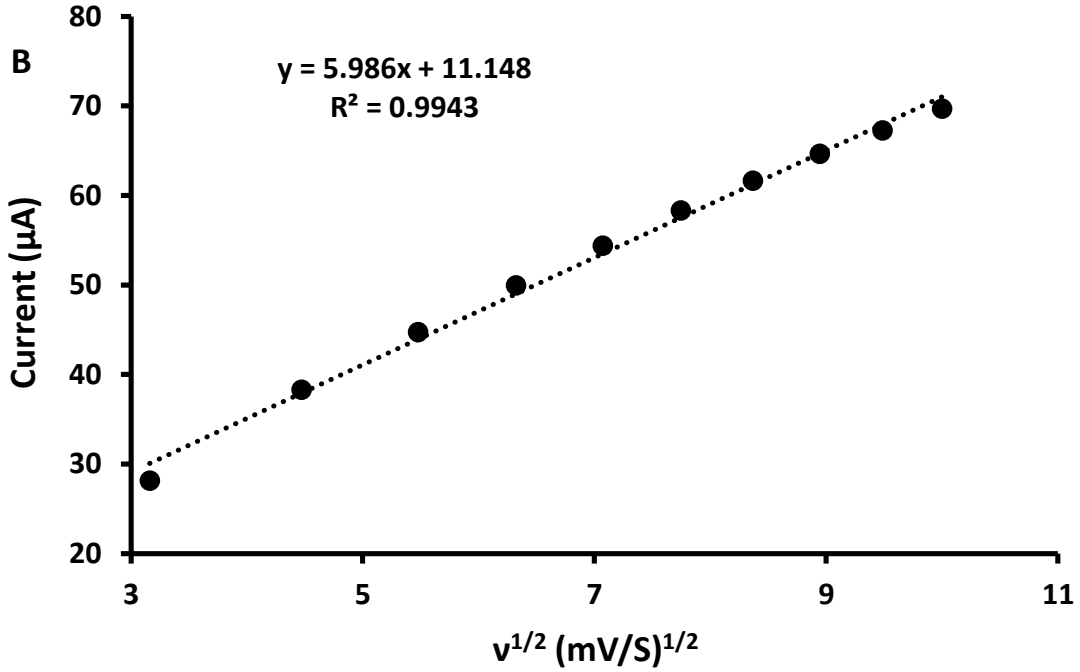
B
y = 5.986x + 11.148
R² = 0.9943
Current (µA)
80
70
60
50
40
30
20
3
5
7
9
11
v1/2 (mV/S)1/2

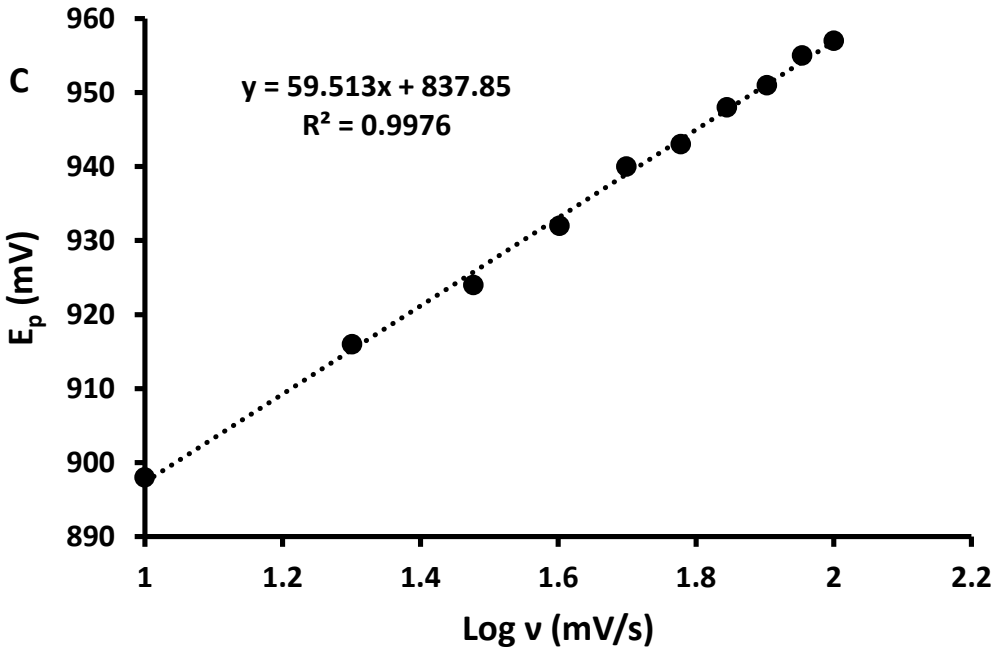

Fig. 5.2: **(A)** is an illustration of the cyclic voltammograms of GCE-NGQDs/**2** at various scan **(B)** is the plot of potential vs. log *v* and **(C)** is the plot of the current against the square root of the scan rate. (*All in the presence of 2.5 mM of nitrite in PBS (pH 7)*).

The linear relationship between E_p vs log *v*, **Fig. 5.2B**, follows equation 5.1 [**163**]:

$$E_p = \frac{b}{2} \log v + \text{constant} \qquad (5.1)$$

where b is the Tafel slope.

An ideal Tafel slope value is that which falls in between 60 – 120 mV/decade [**164**]. The values obtained for the probes range from 103 to 310 mV/decade (**Table 5.1**). Tafel slopes that exceed 200 mV/decade have been reported in literature for graphene-based materials [**165**]. GCE-**1** and GCE-NGQDs/**2** produced Tafel slope values that fell within the 60-120 mV/decade range with values of 103 mV/decade and 119 mV/decade being recorded. The general observation made was that having the GQDs on top of complex **1** produced a lower Tafel slope value than having complex **1** at the top of the GQDs. However, an anomaly in the combination of complex **1** and the GSHGQDs is observed where GCE-GSHGQDs/**1** produces a lower Tafel slope value compared to GCE-**1**/GSHGQDs. The cause of this deviation may be attributed to the GSH being adsorbed onto the graphene surface rather than being incorporated into the graphene framework. Tafel slope values that exceed 120 mV/decade

are said to have no kinetic meaning and may be attributed to the reactants or the products adsorbing onto the electrode surface rendering it inert [**166**].

5.1.3 Chronoamperometric studies

5.1.3.1 Catalytic rates

The sensitivities, limits of detection and the catalytic reaction rate constants were determined through chronoamperometry, using GCE-NGQDs/**1** as an example (**Fig. 5.3**). An increase in the concentration of nitrite produced a linear response towards the peak currents as illustrated in the inset in **Fig. 5.3A**. Plots of the ratio of catalytic currents and buffer currents (I_{cat}/I_{buf}) against the square root of time within the fast decay region gave linear plots of different slopes marked by an increase in the slopes as the concentration increased (**Fig. 5.3B**).

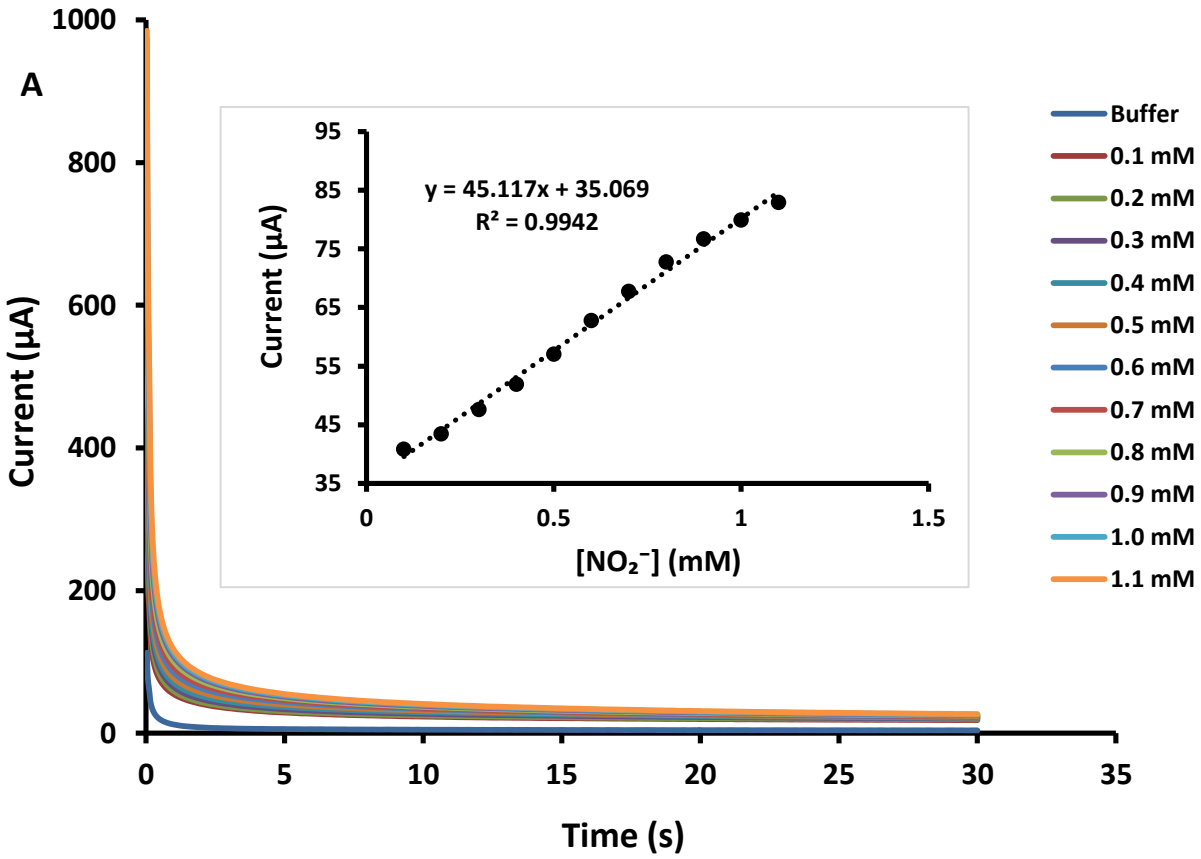

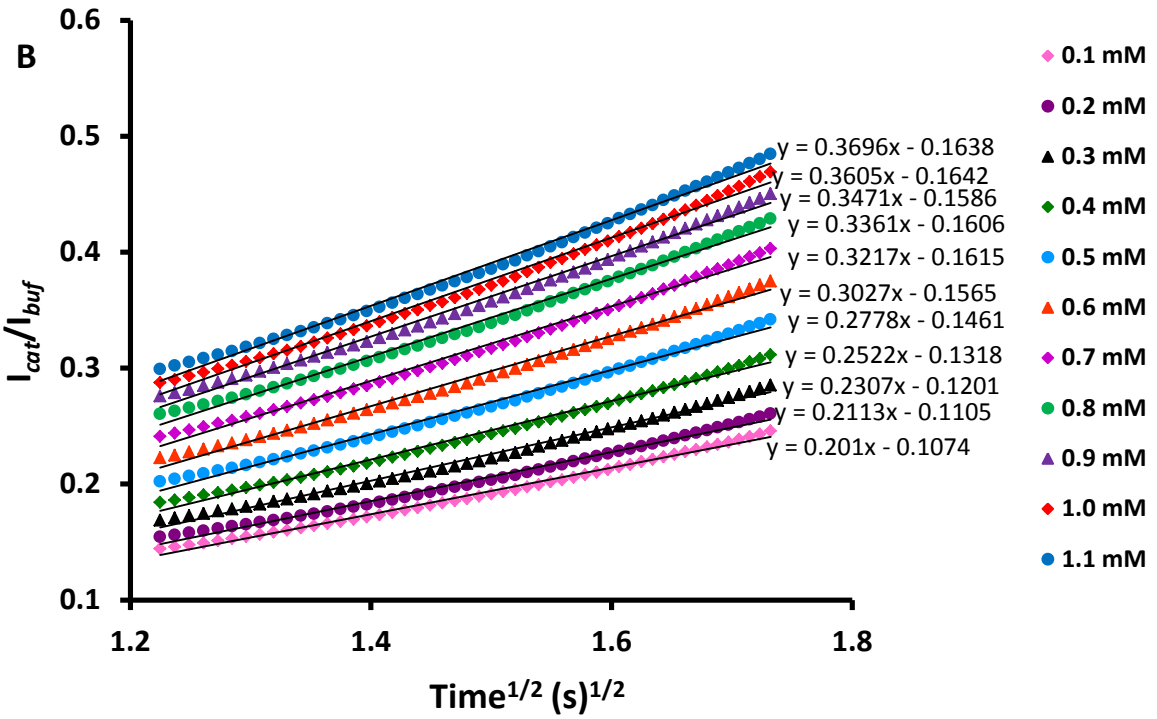

Fig. 5.3: Chronoamperogramms for GCE-NGQDs/**1** in different concentrations of nitrite. Inset: callibration curve for GCE-NGQDs/**1** (**A**) and current ratios versus the square root of time (**B**) in PBS (pH 7).

The gradients obtained from the plots in **Fig. 5.3B** were used to calculate the catalytic rate constants based on equation 5.2 [**167**]:

$$\frac{I_{cat}}{I_{buf}} = \gamma^{1/2}\,\pi^{1/2} = \pi^{1/2}\,(kCt)^{1/2} \qquad (5.2)$$

where I_{cat} and I_{buf} represent the currents in the presence and absence of nitrite, *k* being the catalytic rate constant, *C* the concentration of nitrite and *t* the time that has elapsed in seconds. Plotting the square of the slopes against the respective concentrations gave linear plots whose equations are presented in **Table 5.2** (figure not shown). From these equations, the gradient is equated to πk where *k* can be calculated through applying the appropriate mathematical operation(s) (*k* values are listed in **Table 5.3**).

Table 5.2: Linear equations obtained from the chronoamperometric sensing of nitrite.

(i)	GCE-GQDs – $y = 0.5045[NO_2^-] – 0.0678$, $R^2 = 0.9909$
(ii)	GCE-NGQDs – $y = 0.32[NO_2^-] – 0.0561$, $R^2 = 0.9930$
(iii)	GCE-GSHGQDs – $y = 8.094[NO_2^-] + 0.0064$, $R^2 = 0.9771$
(iv)	GCE-**1** – $y = 0.039[NO_2^-] – 0.0172$, $R^2 = 0.9956$
(v)	GCE-**1**/GQDs – $y = 0.1207[NO_2^-] – 6.00E\text{-}06$, $R^2 = 0.9964$
(vi)	GCE-**1**/NGQDs – $y = 0.1655[NO_2^-] – 0.0172$, $R^2 = 0.9944$
(vii)	GCE-**1**/GSHGQDs – $y = 0.1043[NO_2^-] – 0.0265$, $R^2 = 0.9795$
(viii)	GCE-GQDs/**1** – $y = 1.0589[NO_2^-] – 0.2832$, $R^2 = 0.9884$
(ix)	GCE-NGQDs/**1** - $y = 0.1045[NO_2^-] + 0.0259$, $R^2 = 0.9906$
(x)	GCE-GSHGQDs/**1** – $y = 0.1156[NO_2^-] – 0.015$, $R^2 = 0.9445$
(xi)	GCE-NGQDs/**2** – $y = 0.0027[NO_2^-] – 7E\text{-}05$, $R^2 = 0.9237$

The general observation that can be made from **Table 5.3** is that the combination of the GQDs and complex **1** results in an improvement of the catalytic rate regardless of the order of the modifications. The highest *k* value obtained was 8.59×10^4 $M^{-1}s^{-1}$ for GCE-NGQDs/**2** followed by GCE-**1**/NGQDs and GCE-**1**/GQDs with values of 5.27×10^2 $M^{-1}s^{-1}$ and of 3.84×10^2 $M^{-1}s^{-1}$ respectively. GQDs on their own have low catalytic rates in comparison to complex **1**. In terms of the sequential modifications, lower catalytic rates are observed when complex **1** is placed above the GQDs except for the GSHGQDs where GCE-GSHGQDs/**1** has a higher *k* value than GCE-**1**/GSHGQDs.

Table 5.3: Chronoamperometric summary of the probes examined in the electrochemical sensing of nitrite.

Probe	Sensitivity (μA/mM)	Catalytic rate, k ($M^{-1}s^{-1}$)	LoD (μM)
GCE-GQDs	71.5	1.61×10^1	13.8
GCE-NGQDs	58.2	1.02×10^1	10.9
GCE-GSHGQDs	76.4	2.58	17.2
GCE-**1**	27.4	1.24×10^2	37.4
GCE-**1**/GQDs	38.4	3.84×10^2	16.2
GCE-**1**/NGQDs	45.2	5.27×10^2	18.4
GCE-**1**/GSHGQDs	51.3	3.32×10^2	22.2
GCE-GQDs/**1**	56.7	3.37×10^1	14.4
GCE-NGQDs/**1**	45.1	3.33×10^2	10.0
GCE-GSHGQDs/**1**	64.9	3.68×10^2	15.5
GCE-NGQDs/**2**	51.7	8.59×10^4	20.0

5.1.3.2 Limits of detection

Table 5.4: Limits of detection for nitrite in comparison with literature values for phthalocyanine-based electrodes.

Probe	LoD (μM)	Reference
[a]Pd/CoPc-GCE	0.10	[**168**]
[b]FeMAPc/MPA/AuNPs assembly	0.21	[**169**]
[c]nano-CoTAPC SPE	9.0	[**170**]
[d]$CoPc(SCH_2Ph)_8$-SAM	300	[**171**]
GCE-NGQDs/**1**	10.0	This work

[a]cobalt phthalocyanine-supported Pd nanoparticles
[b]gold nanoparticles (AuNPs) onto glassy carbon electrodes, followed by 3-mercaptopropionic acid (MPA) self-assembly, enabling attachment of an iron(III) monoamino-phthalocyanine (FeMAPc).
[c]Cobalt tetraamino phthalocyanine(CoTAPc) Nano-Structured Modified Screen-Printed Electrodes (SPE).
[d] Self-assembled monolayer of a CoPc

The limit of detection (LoD) was calculated using 3δ/s (where δ is the standard deviation of the blank and s is the slope of the calibration curve, **Fig. 5.3A** (inset)). The limits of detection are presented in **Table 5.3** and are in some cases comparable to the LoDs reported for other phthalocyanine-based electrodes [**168-171**], **Table 5.4**.

Although there are other phthalocyanine-based electrodes which have shown lower LoDs than observed in this work, **Table 5.3,** the current work shows the importance of doping GQDs when designing electrocatalysts based on this material. In addition to that, the fact that the LoD of complex **1** improved in the presence of GQDs shows the importance of the latter in modulating the electrocatalytic activity of phthalocyanines. From **Table 5.3**, it can be deduced that it is better (lower LoD and higher sensitivity) to have complex **1** on top of the GQDs than have the GQDs on top of complex **1**.

5.1.4 Stability studies

In assessing the stability of the electrodes, 20 consecutive cyclic voltammetry scans were conducted at a fixed scan rate of 100 mV/s, at a concentration of 2.5 mM.

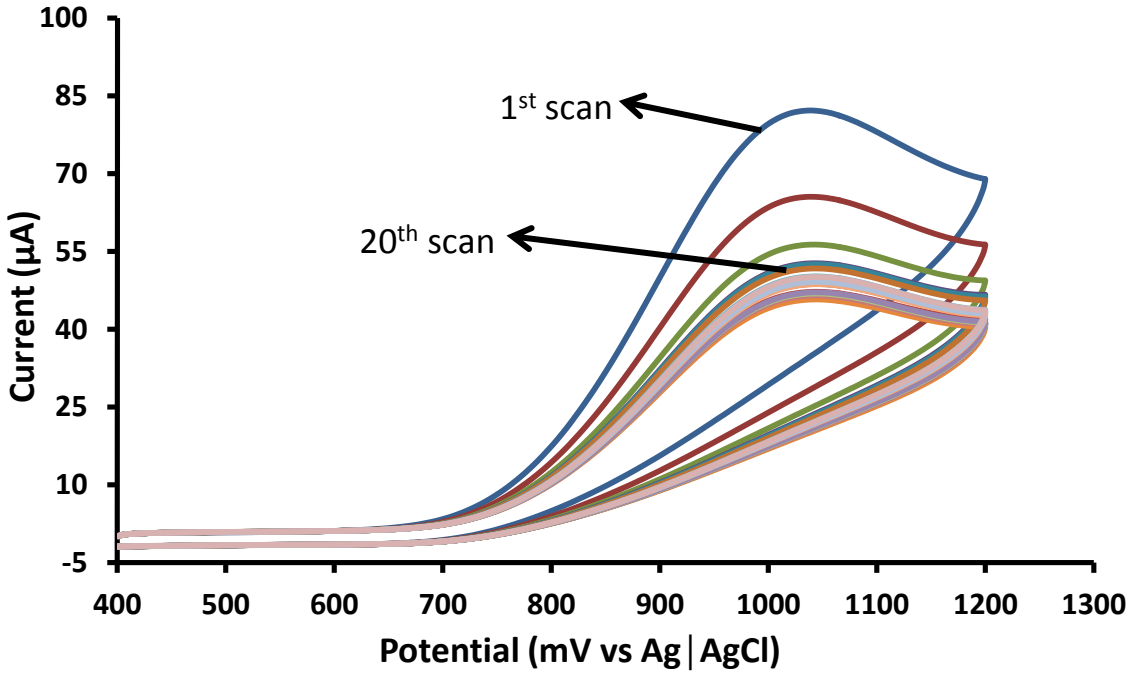

Fig. 5.4: Stability scans for GCE-NGQDs/**1** at 100 mV/s in the presence of 2.5 mM of nitrite in PBS (pH 7).

Fig. 5.4 is an example of some of the probes that were assessed (GCE-NGQDs/**1**). As single probes, none of the materials apart from the NGQDs showed any stability. In the case where the GQDs are drop-dried onto the electrode followed by complex **1**, GCE-NGQDs/**1** appeared to be the most stable (**Fig. 5.4**) as it retained its position of the oxidation potential and assumed a seemingly consistent peak current after a few scans. This was followed by GCE-GQDs/**1** and then GCE-GSHGQDs/**1**. Upon modifying with complex **1** first, none of the probes indicated any stability.

5.2 Electrocatalytic oxidation of hydrazine

5.2.1 Comparative cyclic voltammograms

Since the best limit of detection was obtained using the NGQDs for nitrite, further studies using asymmetric Pcs were carried out using the NGQDs alone. Hydrazine was used instead of nitrite in order to compare with the reported complex **3** which was also applied in the electrochemical sensing of hydrazine [**75**]. The electro-oxidation of hydrazine was carried out in the same manner as that of nitrite. The electrocatalytic behaviour of the asymmetric complexes and their respective conjugates in response to hydrazine was investigated quantitatively and qualitatively using both cyclic voltammetry and chronoamperometry.

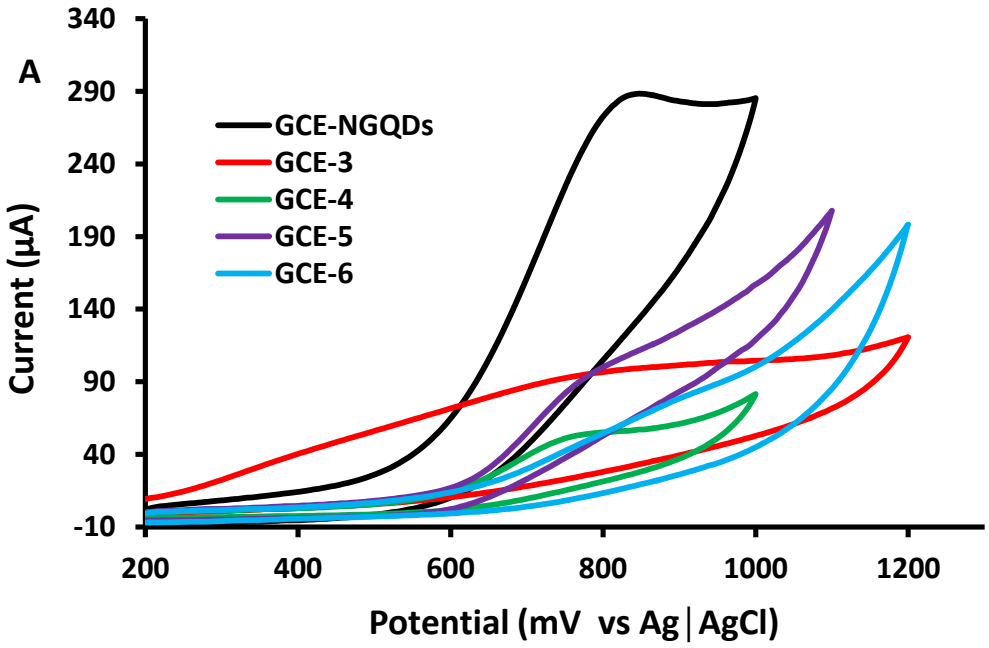

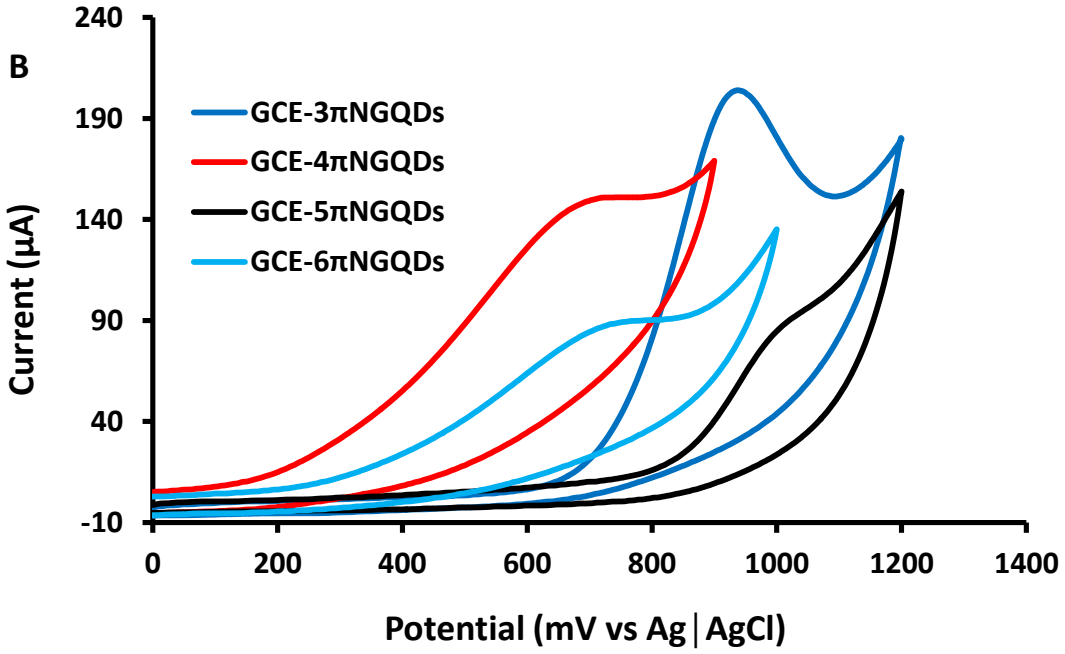

Fig. 5.5: Cyclic voltammograms of selected modified electrodes in in the presence of 1.5 mM of hydrazine in 0.1 M NaOH (**A** – complexes and GQDs (GCE-**3** in 3 mM of N_2H_4); **B** – π-π stacked conjugates).

Fig. 5.5 is an illustration of the results from some of the probes investigated. From the results displayed in **Table 5.5**, the following statements can be made regarding the oxidation potential:

- With respect to the Pc complexes alone, GCE-**3** served as the best, followed by GCE-**4**, GCE-**5** and then GCE-**6**.
    - Furthermore, complexes with the carboxylic acid group performed better than those with the amine group, comparing **3** with **4** and **5** with **6** (each pair containing the same remaining three substituents). This is due to the effect of the push-pull effect induced by the substituents.
- The oxidation potential of the complexes improved in the presence of NGQDs for GCE-**4**πNGQDs, GCE-**6**πNGQDs and GCE@**6**NGQDs, but became worse for GCE-**3**πNGQDs, GCE-**5**πNGQDs and GCE-**4**@NGQDs.
    - This result may suggest that the push-pull effect of the substituents in complexes **3** and **5** is adversely affected by π-π conjugation.

- For the two covalently linked conjugates, a low oxidation potential was obtained from GCE-**6**@NGQDs.

As expressed before, the intensity of the catalytic current also plays an important role in terms of identifying a good electrocatalyst. From **Table 5.5**, the following can be seen:

- For the Pc complexes alone, GCE-**3** produced the highest electrocatalytic current but at a high concentration of 3 mM. Please note much higher currents have been reported for complex **3** at 807 µA at a concentration of 1.0 mM [**75**], this was not observed in this case with a peak current of 89 µA being obtained at a concentration of 3.0 mM. A drastic decline in the Faradaic current may be attributed to the electrode history where continuous surface oxidation of the electrode results in the formation of a dielectric film [**172**].
    - The same electrode was employed throughout the nitrite and hydrazine studies to enable for a fair comparison in the catalytic activity of the Pcs in the absence and in the presence of the GQDs.
- The current decreased for complex **5** upon conjugation to the NGQDs, but increased for complexes **3, 4** and **6**. With complex **5** appearing to be the only anomaly in the π-stacked conjugates, it can be deduced that π-π stacking and covalent linking with NGQDs results in improved electron movement hence enhanced catalytic currents are observed. The enhanced activity of these hybrids is due to a high surface area, electron mobility of graphene and synergic electrocatalytic activity effect between Pc and the graphene layer [**173**].
- In comparing the non-covalently linked conjugates, the highest electrocatalytic current was recorded for GCE-**3**πNGQDs (with substituents that induce a push-pull effect).
- Looking at the covalently linked conjugates, GCE-**4**@NGQDs performed better than GCE-**6**@NGQDs in terms of current but not in terms of the oxidation potential.

5.2.2 Kinetic studies on electrode-hydrazine interactions

The determination of the Tafel slope values for hydrazine was achieved in the same manner as it was for nitrite. **Fig. 5.6A** is an illustration of the results obtained upon varying the scan rate at a fixed concentration of hydrazine. The increment in the current and oxidation potential as the scan rate is increased suggests that the reaction between the analyte and the electrode surface is irreversible as described earlier in the nitrite studies. The linearity observed upon plotting the square root of the scan rate against the current (**Fig. 5.6C**) suggested that the processes happening between the analyte and the electrode are largely diffusion controlled however, from a plot of the log I_p vs log v, it was established that this is not the case for all the probes (**Fig. 5.6D**). Theoretically, a gradient of 0.5 or 1.0 from a plot of the log I_p vs log v corresponds with either diffusion or adsorption controlled processes, respectively (**Fig. 5.6D**) [**174-176**]. In all the probes studied, all but two were diffusion controlled. The gradients obtained for GCE-**4** and GCE-**6** were closer to 1 suggesting that the mechanisms happening on the electrode surface are of an adsorptive nature. The cause for this may be due to the hydrazine binding directly to the central metal as the possibility of such happening has been reported for both cobalt and iron Pcs [**177**]. More so for complexes **4** and **6** in this instance because the analyte itself, hydrazine, is a base and so it is unlikely that it will react with the NH_2 group as it too, is basic.

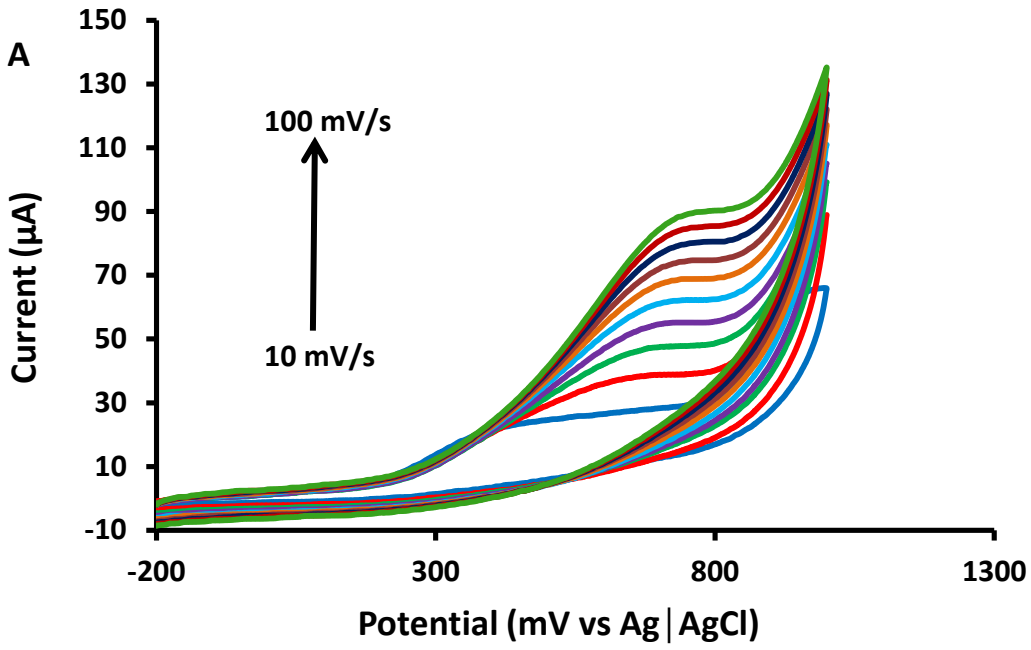

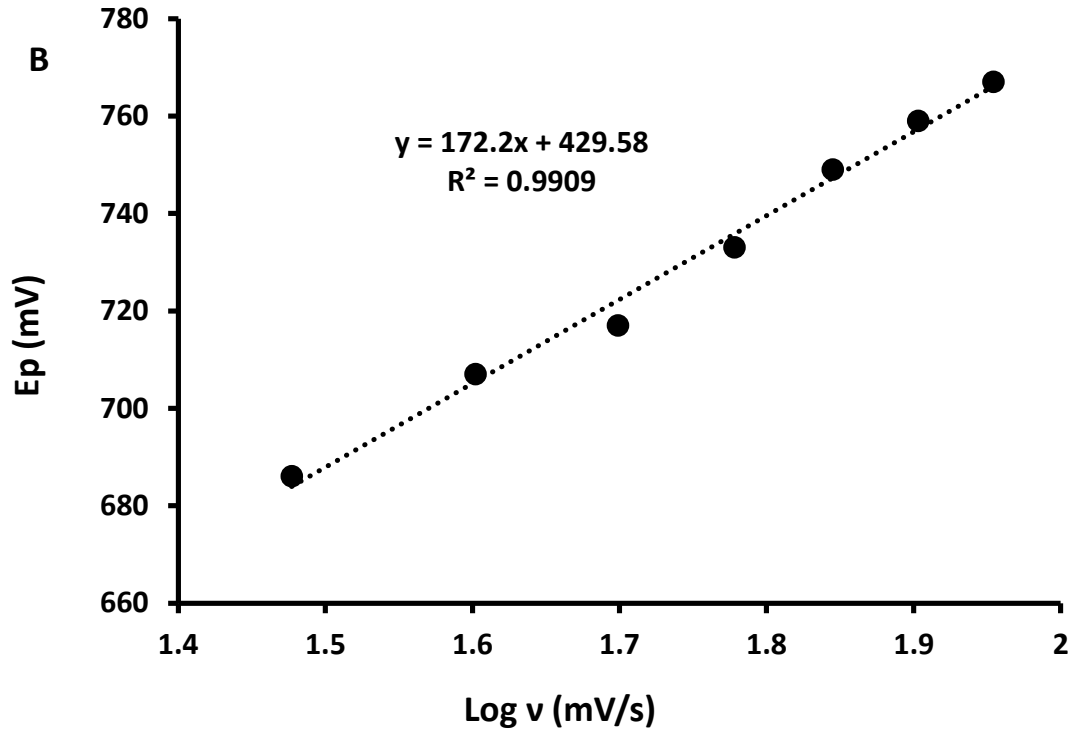
B
780
760
740
720
700
680
660
Ep (mV)
y = 172.2x + 429.58
R² = 0.9909
1.4
1.5
1.6
1.7
1.8
1.9
2
Log v (mV/s)

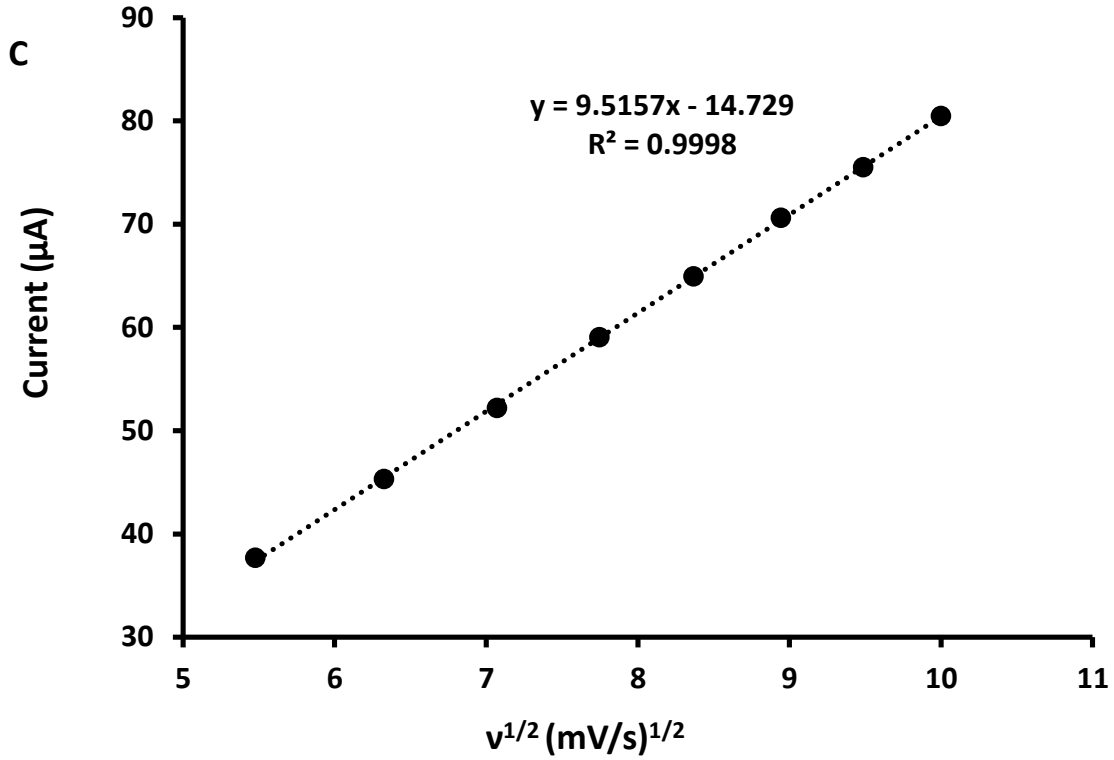
C
90
80
70
60
50
40
30
Current (µA)
y = 9.5157x - 14.729
R² = 0.9998
5
6
7
8
9
10
11
v1/2 (mV/s)1/2

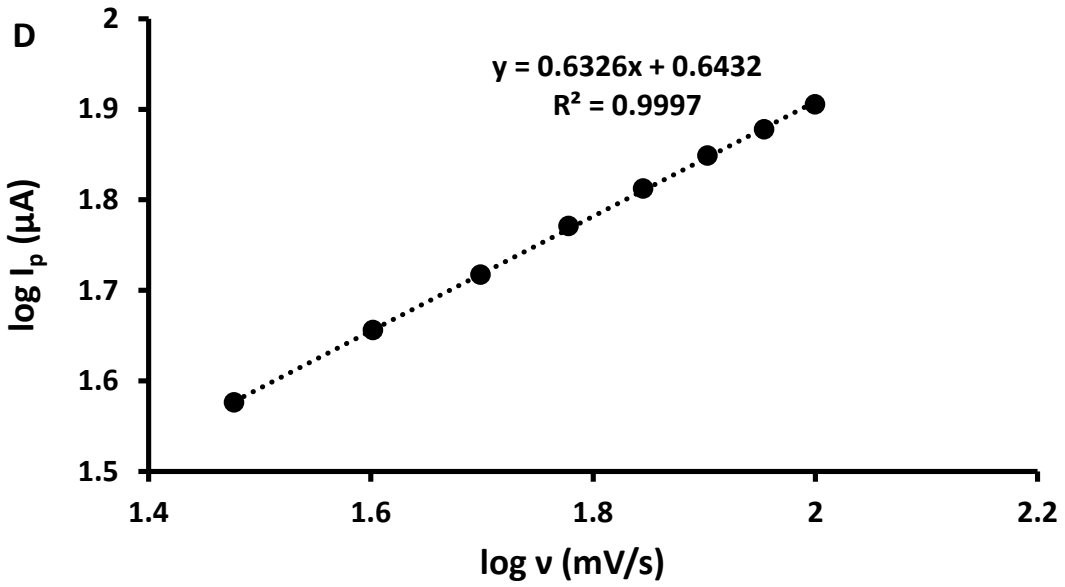

Fig. 5.6: (**A**) is an illustration of the cyclic voltammograms of GCE-**6**πNGQDs at various scan rates (**B**) is the plot of potential vs. log *v* and (**C**) is the plot of the current against the square root of the scan rate and (**D**) is the plot of the log I_p against the log v. (*All in the presence of 1.5 mM of hydrazine in 0.1 M NaOH*).

The Tafel slope values obtained range from 123 to 555 mV/decade, **Table 5.5**. The deviations resulting in the values being far from ideal range of 60 - 120 mV/decade may be attributed to adsorption of some of the oxidation by-products [**166**].

The oxidation by-products (see mechanism below) may adhere to the electrodes resulting in surface passivation as suggested by the Tafel slope values obtained.

The following reaction mechanism has been proposed for the electrocatalytic oxidation of hydrazine on CoPc derivatives [**178**] equations 5.3 to 5.6:

$$[Co(I)Pc]^{-}_{surface} \leftrightarrow [Co(II)Pc]_{surface} + e^{-} \quad (5.3)$$

$$[Co(II)Pc]_{surface} + N_2H_4 + OH^{-} \xrightarrow{rds} [Co(I)Pc \ldots N_2H_3]^{-}_{surface} + H_2O \quad (5.4)$$

$$[Co(I)Pc \ldots N_2H_3]^{-}_{surface} \rightarrow [Co(I)Pc]^{-}_{surface} + * N_2H_3 \quad (5.5)$$

$$* N_2H_3 + 3OH^{-} \xrightarrow{fast} N_2 + 3e^{-} + 3H_2O \quad (5.6)$$

This mechanism shows the involvement of the central Co metal in electrocatalysis. Using UV-Vis spectroscopy, it was illustrated that the central metal cobalt (Co^{II}) retains its oxidation state even after conjugation hence it is involved in the electrocatalysis. During the electro-oxidation process the hydrazine molecule interacts with the metal centre, causing electron drain from one of the lone pair of electrons of the nitrogen atoms of hydrazine towards the central metal forming a bond in Co(I)Pc-N_2H_3. The Co(I)Pc-N_2H_3 is decomposed, equation 5.5, with N_2H_3 released into solution to react with $^-$OH ions from the basic media to form N_2, equation 5.6. From Co(I)Pc, Co(II)Pc can be regenerated, allowing repetition of the process. The role of the GQDs is to enhance the electrocatalytic activity of the CoPc as stated above.

Table 5.5: Summary of data for the electro-oxidation of hydrazine acquired from the cyclic voltammetry (*all for 1.5 mM hydrazine at a scan rate of 100 mV/s, unless otherwise stated*).

Probe	**E_p (mV) vs. Ag|AgCl**	**Background corrected I_p (µA)**	**Tafel slope (mV decade^{-1})**
GCE-NGQDs	832	263	156
GCE-**3**[b]	780	89	250
GCE-**3**πNGQDs	936	183	123
GCE-**4**	795	47.3	155
GCE-**4**πNGQDs	704	140	346
GCE-**4**@NGQDs	936	96.3	555
GCE-**5**	801	80.8	211
GCE-**5**πNGQDs	1030	73.4	272
GCE-**6**	815	45.1	215
GCE-**6**πNGQDs	782	80.4	344
GCE-**6**@NGQDs	741	62.4	334

[b] in 3 mM.

5.2.3 Chronoamperometric studies

5.2.3.1 Catalytic rates

The chronoamperometric responses of GCE-**5**πNGQDs are illustrated in **Fig. 5.7** where the inset in **Fig. 5.7A** illustrates the linear relationship between the concentration of hydrazine and the current. Similar to the nitrite, the ratio between the catalytic currents at various concentrations of hydrazine and that of the buffer (I_{cat}/I_{buf}) against the square root of time yielded linear graphs of varying gradients (equations presented in **Table 5.6**) attributed to the increase in analyte concentration (**Fig. 5.7B**). These plots of gradient versus concentration (figure not shown) were used to determine the *k* values for hydrazine as it was done for nitrite (**Table 5.7**).

Looking at the Pc complexes alone, GCE-**4** at 3.47×10^2 $M^{-1}s^{-1}$ has the highest catalytic rate followed by GCE-**5** and GCE-**6** with values of 1.12×10^2 $M^{-1}s^{-1}$ and 6.00×10^1 $M^{-1}s^{-1}$ respectively. GCE-**3** registered the lowest catalytic rate despite the literature reporting otherwise [**75**]. The general trend observed from the conjugates is a decline in the catalytic rate constants with the exception of GCE-**4**πNGQDs and GCE-**4**@NGQDs where significant increases in the catalytic rates were observed. The decline in the catalytic rate upon conjugation may be attributed to the NGQDs as they produced a low *k* value on their own.

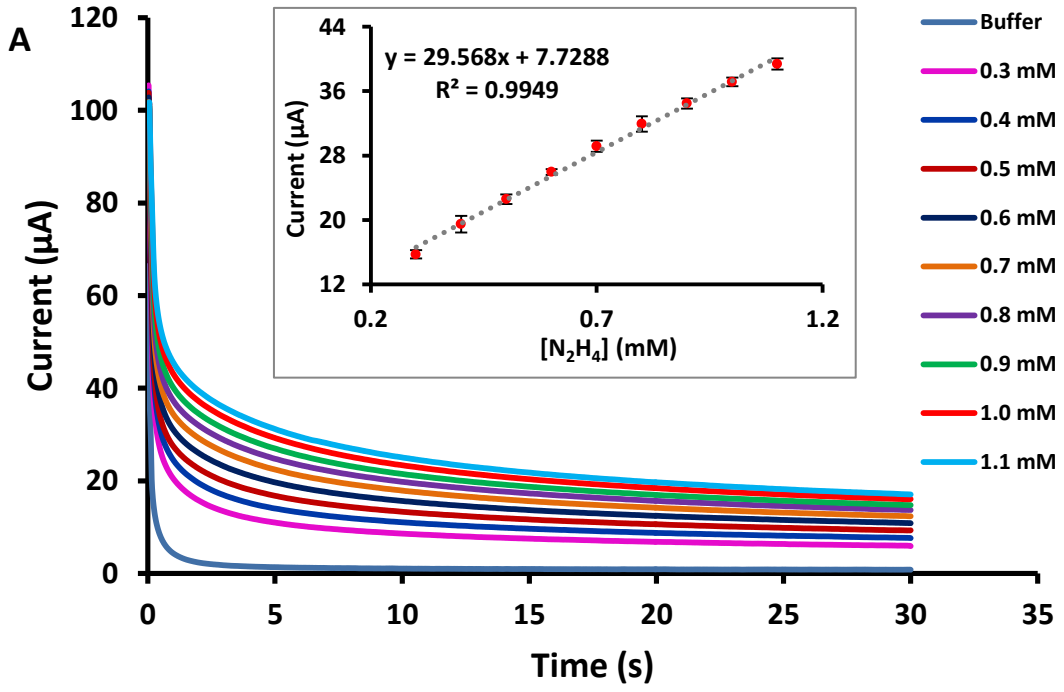

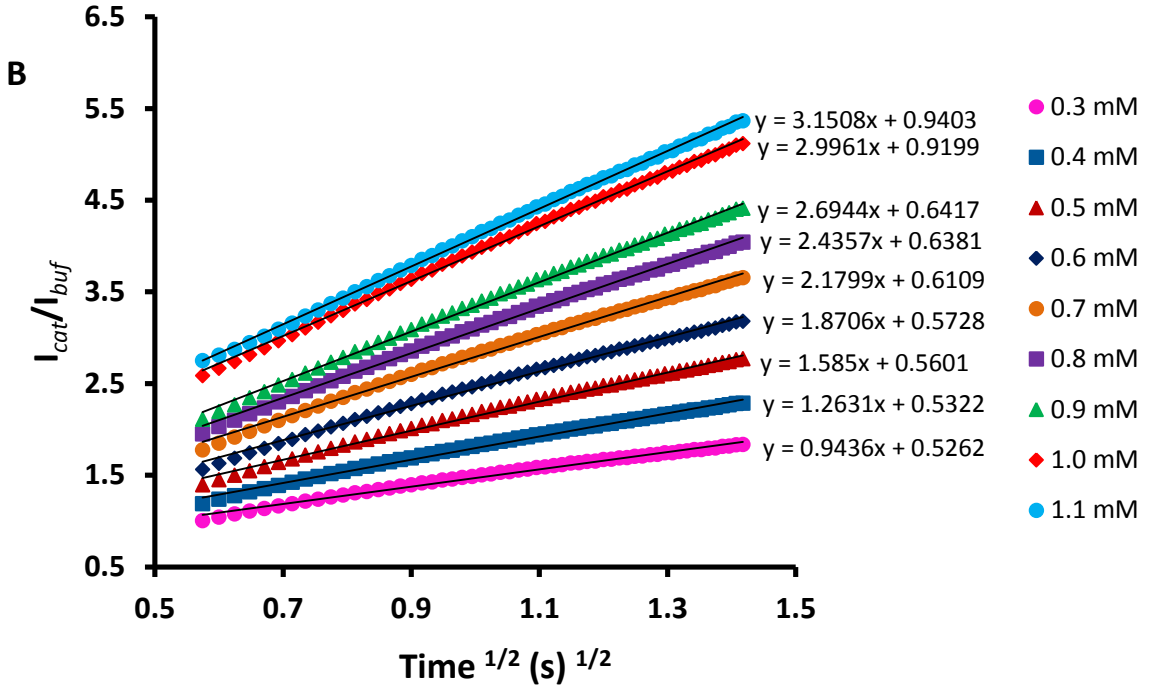

Fig. 5.7: (**A**) Chronoamperograms for GCE-**5**πNGQDs in different concentrations of hydrazine. Inset: calibration curve for GCE-**5**πNGQDs (n=4) and (**B**) current ratios versus the square root of time for hydrazine in 0.1 M NaOH.

Table 5.6: Linear equations obtained from the chronoamperometric sensing of hydrazine.

(i)	GCE-NGQDs – y = 3.8232[N_2H_4] – 1.7391, R^2 = 0.9923
(ii)	GCE-**3** – y = 5.2716[N_2H_4] – 1.9023, R^2 = 0.9921
(iii)	GCE-**3**πNGQDs – y = 3.4112[N_2H_4] – 0.8067, R^2 = 0.9931
(iv)	GCE-**4** – y = 0.1091[N_2H_4] – 0.0279, R^2 = 0.99613
(vi)	GCE-**4**πNGQDs – y = 0.011[N_2H_4] – 0.0015, R^2 = 0.9788
(vii)	GCE-**4**@NGQDs – y = 0.0056[N_2H_4] – 0.0039, R^2 = 0.9922
(viii)	GCE-**5** – y = 0.0352[N_2H_4] + 0.0638, R^2 = 0.8099
(vix)	GCE-**5**πNGQDs – y = 12.275[N_2H_4] – 3.6493, R^2 = 0.9937

(ix)	GCE-**6** – y = 1.8864[N_2H_4] – 1.1116, R^2 = 0.9906
(x)	GCE-**6**πNGQDs – y = 7.2119[N_2H_4] – 2.7872, R^2 = 0.9956
(xi)	GCE-**6**@NGQDs – y = 13.54[N_2H_4] – 3.9389, R^2 = 0.9953

5.2.3.2 Limits of detection

The same approach taken for calculating the LoDs for nitrite was adopted for calculating those of hydrazine. **Table 5.7** shows that there is a huge improvement (lowering) of the LoD when Pcs are linked (covalently or non-covalently) to GQDs with the lowest value being for GCE-**3**πNGQDs at 0.43 μM, this can be attributed to the differences in the electron-withdrawing and electron-donating abilities of the substituents that make up the molecules.

Table 5.7: Chronoamperometric summary of the probes examined in the electrochemical sensing of hydrazine.

Probe	Sensitivity (μA/mM)	Catalytic rate, *k* ($M^{-1}s^{-1}$)	LOD (μM)
GCE-NGQDs	115	1.22	11
GCE-**3**	7.58	1.68	3.81[b]
GCE-**3**πNGQDs	164	1.08	0.43
GCE-**4**	7.08	3.47×10^2	6.25
GCE-**4**πNGQDs	96.0	3.50×10^3	0.85
GCE-**4**@NGQDs	87.6	1.78×10^3	0.94
GCE-**5**	118	1.12×10^2	7.05
GCE-**5**πNGQDs	29.6	8.91	4.19
GCE-**6**	6.44	6.00×10^1	12.7
GCE-**6**πNGQDs	24.8	2.30	3.93
GCE-**6**@NGQDs	21.5	4.31	6.81

[b] literature value – 3.2 μM

The effectiveness of complex **3** is related to the push-pull effect and the addition of GQDs adds to improved catalytic activity when the two are π-conjugated in GCE-**3**πNGQDs. Complex **3** is composed of three *tert*-butyl terminals and complex **5** comprises of three diethylamino groups attached to the phenyl. Both complexes have a carboxylic acid on the fourth end as a moderate electron-withdrawing group. The *tert*-butyl group is a weak electron-donating group and the diethylamino substituent is a strong electron-donating group which may have nullified the COOH's ability to exercise its electron-withdrawing effect in complex **5**; and in turn, supressing the push-pull effect that is observed in complex **3**. The values obtained in this work for GCE-**3**πNGQDs, GCE-**4**πNGQDs and GCE-**4**@NGQDs (of the order of 10^{-7} M) are a huge improvement compared to literature values shown in **Table 5.8** [**74, 75, 170, 179, 180**]. This shows the importance of using nitrogen doped GQDs in conjunction with phthalocyanines.

Table 5.8: Limits of detection for hydrazine in comparison with literature values for CoPc derivatives.

Electrodes	LOD (μM)	Reference
Co tetracarboxyphenoxy Pc π-π stacked with GQDs	8	[**74**]
Co tetraaminophenoxy Pc π-π stacked with GQDs	43	[**74**]
Co monocarboxyphenoxy Pc π-π stacked with GQDs	10	[**74**]
GCE-**3**@rGQDs[a]	4.4	[**75**]
GCE-**3**πrGQDs[a]	2.1	[**75**]
CoPc - screen-printed electrodes	6.21	[**170**]
Co tetrahexynl Pc	6.09	[**179**]
CoPc- carbon paste electrode	73.5	[**180**]

[a] rGQDs = reduced GQDs

The LoD detection values may also be related to the Raman I_D/I_G ratio since the presence of more π bonds (low I_D/I_G ratio ratio) promotes better electron movement as there is more delocalization of electrons within the MPc/GQD system. Thus comparing push-pull complexes **3** (in GCE-**3**πNGQDs, I_D/I_G = 0.63) and **5** (in GCE-**5**πNGQDs, I_D/I_G = 0.81) a low LoD

is observed for the former with a low I_D/I_G ratio. This applies to the linked conjugates for **4** and **6** where the GCE-**4**@NGQDs (I_D/I_G = 0.33) with a very low I_D/I_G ratio has a better LoD than GCE-**6**@NGQDs (I_D/I_G = 0.91). Thus, it is not only the nature of the Pc which affects the catalytic behaviour but also the interaction between the Pc and the GQDs.

5.2.4 Stability studies

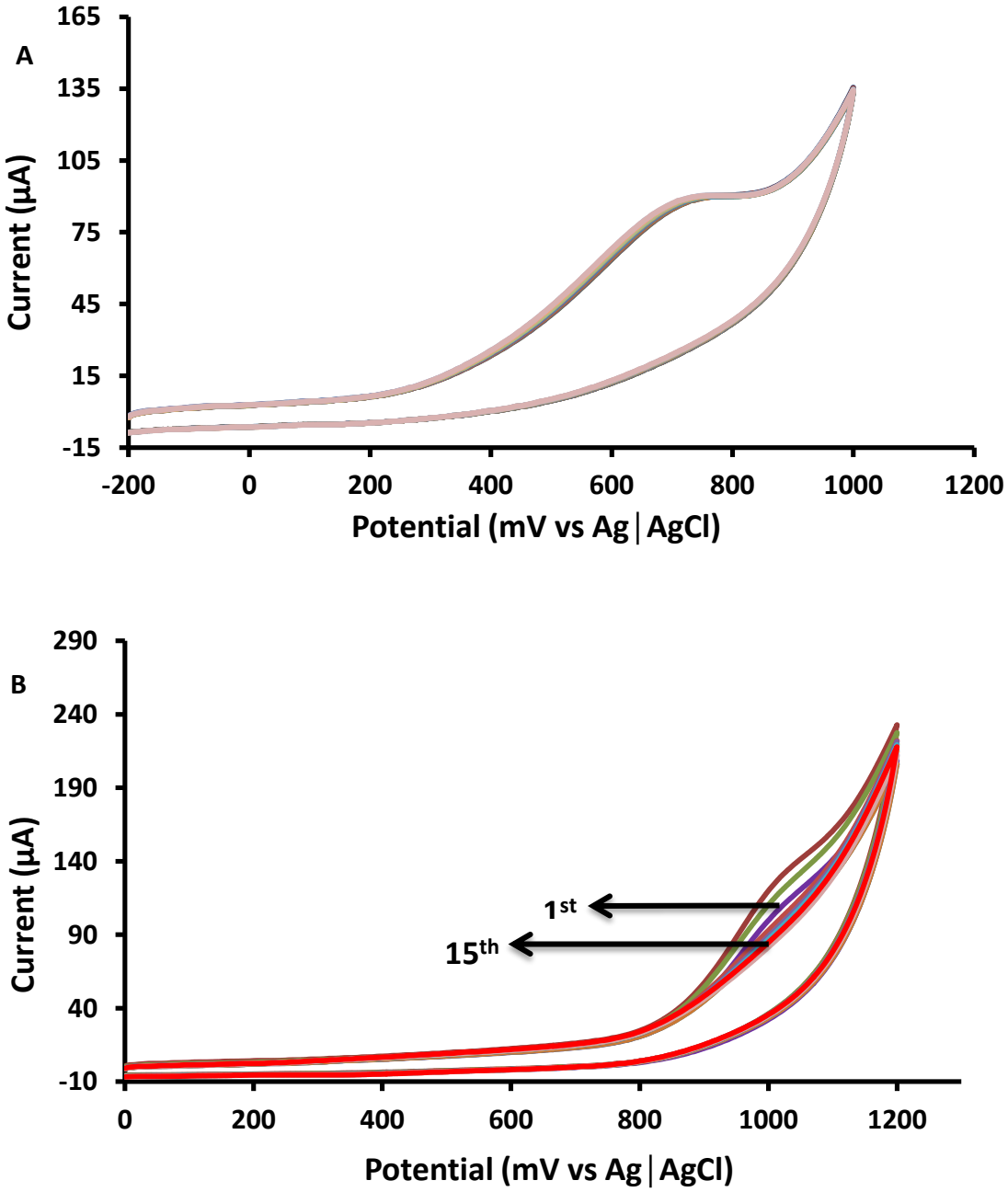

Fig. 5.8: Stability scans for GCE-**6**πNGQDs, 20 scans (**A**) and GCE-**5**πNGQDs, 15 scans (**B**) at 100 mV/s in the presence of 1.5 mM of hydrazine in 0.1 M NaOH.

Twenty consecutive cyclic voltammetry scans were recorded in the presence of the analyte at a constant scan rate of 100 mV/s to monitor the stability of the probes. As single entities, GCE-**4** was the most stable followed by GCE-**6**. Complexes **3** and **5** were unstable in both their singular forms as well as in their π-stacked conjugated systems. The cause for the instability observed in complexes **3** and **5** may be a possible result of the push-pull system that is created by the asymmetry of the molecule. The same cannot be applied for complexes **4** and **6** as the nature of the substituents do not induce a push-pull effect hence the high stability of the conjugates related to complexes **4** and **6**. An example of one of the conjugates is presented in **Fig. 5.8A** and it is evident that the electrode is highly stable as the difference between the first scan and the twentieth is of a negligible magnitude in terms of the peak current as well as the position of the oxidation potential. **Fig. 5.8B** is an illustration of an unstable electrode where the modified electrode is unable to retain a prominent oxidation peak after 15 consecutive scans.

5.3 Summary of chapter

The electrocatalytic oxidation of nitrite and hydrazine was successfully carried out using Pcs, GQDs and combinations of the two through covalent and non-covalent means. Although the sequentially modified electrodes appear to be plagued by instability, the LoD values obtained served as an important guide in terms of establishing which kind of GQDs are better suited for further exploration with Pcs.

Following up on the nitrite studies, the series of asymmetric Pcs and their NGQD-based conjugates further illustrated in the electrochemical sensing of hydrazine that stronger electrostatic forces between Pc and GQD ensure better electrocatalytic activity i.e. π-π stacking yields better results than sequential modifications. Furthermore, the interaction between the Pc and the NGQDs is important in terms of orientation; disruption of the graphene framework leads to a high I_D/I_G ratio which is detrimental to electrocatalysis as there is a reduction in delocalized electrons thus restricting electron movement.

Chapter 6

Conclusions

General conclusions and future prospects.

6.1 General conclusions

In this thesis, a series of previously synthesized and original Pc molecules are presented. These complexes, following extensive purification and characterization, are applied as electrocatalysts towards the oxidation of nitrite and hydrazine in the presence of doped GQDs. The electrochemical studies pertaining to nitrite illustrated the importance of doping in GQDs and how it is able to enhance the electrocatalytic activity of Pcs. The studies concerned with hydrazine using asymmetric Pc complexes further showed that a reduction in symmetry is highly beneficial as it enables the creation of more complex electrochemical sensing devices without compromising on the efficiency of the Pc molecules on the own. And while push-pull systems are good for electrochemical sensing, other asymmetric Pcs function just as well provided that they are coupled with the appropriate nanomaterial. Furthermore, the positions of the Pc (and its substituents if there are any) relative to the graphene network that makes up the GQDs plays a significant role in the electrocatalytic behaviour of a probe. A high I_D/I_G ratio is unfavourable as it is synonymous with defects in the graphene which in turn hinder electron movement.

6.2 Future prospects

As mentioned in the nitrite studies, the iron(III) chloride (complex **2**) showed great instability in ambient conditions but even then, the one electrochemical experiment in which it was applied showed that it is a worthy candidate in electrochemical sensing and so moving forward, it would be ideal if the complex or those similar to it could be stabilized perhaps through the insertion of a different axial ligand such that it is not easily oxidized. In addition to that, for the purpose of designing more sensitive, analyte-specific asymmetrical phthalocyanine-based electrodes, further exploration with other central metals such as nickel and manganese, paired with the highly conductive NGQDs should be undertaken.

References

1. R. Li, C. Li, *Adv. Catal*. **2017**, *60*, 1-57.
2. H. Wendt, G. Kreysa in: *Electrochemical Engineering*, Springer, **1999**, Berlin.
3. B. Bhattacharyya in: *Electrochemical Micromachining for Nanofabrication, MEMS and Nanotechnology*, Elsevier, **2015**, Oxford.
4. C. S. J. N. O'Donoghue, G. Fomo, T. Nyokong, *Electroanalysis* **2016***, 28,* 3019-3027.
5. R. Moscoso, J. Carbajo, J. A. Squella, *J. Chil. Chem. Soc*. **2014**, *59*, 2498-2501.
6. F. Crespi, *Xjenza Malta Chamber of Scientists* **2013**, *1*, 14-22.
7. K.C. Honeychurch in: *Printed Films*, Woodhead Publishing, **2012**, Cambridge.
8. Y. Wang, W. Wang, G. Li, Q. Liu, T. Wei, B. Li, C. Jiang, Y. Sun, *Microchim. Acta* **2016**, *183*, 3221-3228.
9. T. S. H. Pham, P. J. Mahon, G. Lai, A. Yu, *Electroanalysis* **2018**, *30*, 2185-2194.
10. A. Molina, C. M. Soto, J. González, *Anal. Chem*. **2009**, *81*, 6830-6836.
11. F.D. Munteanu, N. Mano, A. Kuhn, L. Gorton, *Bioelectrochemistry* **2002**, *56*, 67-72.
12. J. Grimshaw in: *Electrochemical Reactions and Mechanisms in Organic Chemistry*, Elsevier, **2000**, Amsterdam.
13. T. Shigemitsu, G. Matsumoto,S. Tsukahara, *Med. & Biol. Eng. & Comput*. **1979**, *17*, 465-470.
14. H. E. Zittel, and F. J. Miller, *Anal. Chem.* **1965**, *37*, 200-203.
15. A. J. Bard, *J. Chem. Educ*. **1983**, *60*, 302-304.
16. A. de Leon, R, C. Advincula in: *Intelligent Coatings for Corrosion Control*, edited by A. Tiwari, J. Rawlins, L. H. Hihara, Butterworth-Heinemann, **2014**, Oxford.
17. D. Bélanger, J. Pinson, *Chem. Soc. Rev*. **2011**, *40*, 3995-4048.
18. M. S. Singh, S. Chowdhury, S. Koley, *Tetrahedron* **2016**, *72*, 5257-5283.
19. National Research Council in: *Expanding the Vision of Sensor Materials*, National Academy Press**, 1995**, Washington, D.C.
20. D. Grieshaber, R. MacKenzie, J. Vörös, E. Reimhult, *Sensors* **2008**, *8*, 1400-1458.
21. K. Sakamoto, E. Ohno-Okumura, *Materials* **2009**, *2*, 1127-1179.
22. C. G. Claessens, U. Hahn, T. Torres, *Chem. Rec*. **2008**, *8*, 75-97.
23. T. Soganci, Y. Baygu, N.Kabay, Y. Gök, M. Ak, *ACS Appl. Mater. Interfaces* **2018**, *10*, 21654-21665.

24. T. A. Turkmen, L. Zeng, Y. Cui, İ. Fidan, F. Dumoulin, C. Hirel, Y. Zorlu, V. Ahsen, A. A. Chernonosov, Y. Chumakov, K. M. Kadish, A. G. Gürek, S. T. Öztürk, *Inorg. Chem*. **2018**, *57*, 6456-6465.
25. M. Liao,T. Kar, S. M. Gorun, S. Scheiner, *Inorg. Chem.* **2004**, *43*, 7151-7161.
26. D. Dini, M. J. F. Calvete, M. Hanack, M. Meneghetti, *J. Phys. Chem. A* **2008**, *112*, 8515-8522.
27. M. A. Dahlen, *Ind. Eng. Chem. Res*. **1939**, *31*, 839-847.
28. A. B. Sorokin, *Chem. Rev*. **2013**, *113*, 8152-8191.
29. J. Moan, *J. Photochem. Photobiol. B Biol*. **1990**, *5*, 521-524.
30. M. J. Cook, I. Chambrier, S. J. Cracknell, D. A. Mayes, D. A. Russell, *Photochem. Photobiol*. **1995**, *62*, 542-545.
31. J. R. Pinzon, M. E. Plonska-Brzezinska, C. M. Cadona, A. J. Athans, S. S. Gayathri, D. M. Guldi, M. A. Herranz, N. Martin, T. Torres, L. Echegoyen, *Angew. Chem. Int. Ed*. **2008**, *47*, 4173-4176.
32. Ö. Bekaroğlu, *Turk. J. Chem.* **2014**, *38*, 903-922.
33. J. Mack, N. Kobayashi, *Chem. Rev*. **2011**, *111*, 281-321.
34. D. K. MacFarland, C. M. Hardin, M. J. Lowe, *J. Chem. Educ*. **2000**, *77*, 1484-1485.
35. V. Rãdiþoiu, L. Wagner, A. Rãdiþoiu, P. Ardeleanu, V. Amãriuþei, A. Sorescu, *Rev. Chim*. **2008**, *59*, 973-978.
36. J. G. Young, W. Onyebuagu, *J. Org. Chem*. **1990**, *55*, 2155-2159.
37. P. Apostol, A. Bentaleb, M. Rajaoarivelo, R. Clérac, H. Bock, *Dalton Trans*. **2015**, *44*, 5569-5576.
38. J. Sforzini, F. C. Bocquet, F. S. Tautz, *Phys. Rev. B* **2017**, *96*, 165410-165422.
39. C. Murray, N. Dozova, J. G. McCaffrey, S. FitzGerald, N. Shafizadeh, C. Crépin, *Phys. Chem. Chem. Phys*. **2010**, *12*, 10406-10422.
40. V. N. Nemykin, S. V. Dudkin, F. Dumoulin, C. Hirel, A.G. Gürek, V. Ahsen, *ARKIVOC* **2014**, 142-204.
41. C. C. Leznoff, A. B. P. Lever in: *Phthalocyanines: Properties and Applications*, Publishers (LSK) Ltd, **1996**, Cambridge.
42. K. M. Kadish, K.M. Smith, K.M. R. Guillard in: *The Porphyrin Handbook*, Academic Press, **2003**, San Diego.
43. Y. Rio, M. S. Rodriguez-Morgade, T. Torres, *Org. Biomol. Chem*. **2008**, *6*, 1877-1894.

44. H. Isago in: *Optical Spectra of Phthalocyanines and Related Compounds*, Springer, **2015**, Tsukuba.
45. J. Mack, M. J. Stillman, *Coord. Chem. Rev*. **2001**, *219-221*, 993-1032.
46. J. Mack, M. J. Stillman in: *Porphyrin Handbook, Phthalocyanine Properties and Materials*, edited by K. M. Kadish, K.M. Smit, R. Guilard, Academic Press, **2003**, New York.
47. T. Nyokong in: *Structure and Bonding: Functional Phthalocyanine Molecular Materials,* edited by J. Jiang, D.M.P. Mingos, Springer, **2010**, Berlin.
48. E. A. Ough, Z. Gasyna, M. J. Stillman, *Inorg. Chem*. **1991**, *30*, 2301-2310.
49. H. Huang, K.E. Rieckhoff, E.M. Voight, *J. Chem. Phys*. **1982**, *77*, 3424-3441.
50. J. Obirai, T. Nyokong, *Electrochim. Acta* **2005**, *50*, 3296-3304.
51. İ. Acar, E. T. Saka, S. Topçu, Z. Bıyıklıoğlu, H. Kantekin, A. Aktaş, *J. Coord. Chem*. **2015**, *68*, 1847-1858.
52. T. Nyokong, *S. Afr. J. Chem*. **1995**, *48*, 23-29.
53. G. Ferraudi in: *Phthalocyanines, Properties and Applications*, edited by C. C. Leznoff, A. B. P. Lever, VCH, **1989**, New York.
54. T. Nyokong, *Polyhedron* **1993**, *12*, 375-381.
55. M. J. Aguirre, M. Isaacs, F. Armijo, L. Basáez, J. Zagal, *Electroanalysis* **2002**, *14*, 356-362.
56. N. Sehlotho, T. Nyokong, J. H. Zagal, F. Bedioui, *Electrochim. Acta* **2006**, *51*, 5125-5136.
57. J. F. Silva, S. Griveau, C. Richard, J. H. Zagal, F. Bedioui, *Electrochem. Comm*. **2007**, *9*, 1629-1634.
58. F. Bedioui, S. Griveau, T. Nyokong, C. John Appleby, C. A. Caro, M. Gulppi, G. Ochoa, J. H. Zagal, *Phys. Chem. Chem. Phys*. **2007**, *9*, 3383-3396.
59. B. Agboola, T. Nyokong, *Anal. Chim. Acta* **2007**, *587*, 116-123.
60. P. Tau, T. Nyokong, *J. Electroanal. Chem.* **2007**, *611*, 10-18.
61. J. Obirai, F. Bedioui, T. Nyokong, *J. Electroanal. Chem*. **2005**, *576*, 323-332.
62. K. I. Ozoemena, D. Nkosi, T. Nyokong, I. Chambrier, M. J. Cook, *Electrochim. Acta* **2007**, *52*, 4132-4143.
63. N. Nombona, P. Tau, N. Sehlotho, T. Nyokong, *Electrochim. Acta* **2008**, *53*, 3139-3148.

64. K. I. Ozoemena, J. Pillay, T. Nyokong, *Electrochem. Comm*. **2006**, *8*, 1391-1396.
65. T. Mafatle, T. Nyokong, *Anal. Chim. Acta* **1997**, *354*, 307-314.
66. K. H. Koh, S.H. Noh, T. Kim, W. J. Lee, S. Yi, T. Han, *RSC Adv*. **2017**, *7*, 26113-26119.
67. J. Yang, D. Mu, Y. Gao, J. Tan, A. Lu, D. Ma, *J. Nat. Gas Chem.* **2012**, *21*, 265-269.
68. D. A. Geraldo, C. A. Togo, J. Limson, T. Nyokong, *Electrochim. Acta* **2008**, *53*, 8051-8057.
69. V. Mani, R. Devasenathipathy, S. Chen, S. Huang, V. S. Vasantha, *Enzyme Microb. Technol.* **2014**, *66*, 60-66.
70. H.F. Cui, K. Zhang, Y.F. Zhang, Y.L. Sun, J. Wang, W.D. Zhang, *Biosens. Bioelectron*. **2013**, *46*, 113-118.
71. H. Xu, J. Xiao, B. Liu, S. Griveau, F. Bedioui, *Biosens. Bioelectron*. **2015**, *66*, 438-444.
72. S. Nyoni, T. Nyokong, *Electrochim. Acta* **2014**, *136*, 240-249.
73. S. A. Mamuru, K. I. Ozoemena, T. Fukuda, N. Kobayashi, T. Nyokong, *Electrochim. Acta* **2010**, *55*, 6367-6375.
74. S. Centane, O. J. Achadu, T. Nyokong, *Electroanalysis* **2017**, *29*, 2470-2482.
75. S. Centane, E. K. Sekhosana, R. Matshitse, T. Nyokong, *J. Electroanal. Chem*. **2018**, *820*, 146-160.
76. S. Nyoni, T. Nyokong, *Polyhedron* **2015**, *98*, 47-54.
77. M. Shumba, T. Nyokong, *Electrochim. Acta* **2016**, *196*, 457-469.
78. M. Shumba, T. Nyokong, *Electrochim. Acta* **2016**, *213*, 529-539.
79. N. W. Polaske, H. Lin, A. Tang, M. Mayukh, L. E. Oquendo, J. T. Green, E. L. Ratcliff, N. R. Armstrong, S. S. Saavedra, D. V. McGrath, *Langmuir* **2011**, *27*, 14900-14909.
80. G. G. Matlou, N. Kobayashi, M. Kimura, T. Nyokong, *New J. Chem*. **2017**, *41*, 12309-12318.
81. C. C. Byeon, M. M. McKerns, W. Sun, T. M. Nordlund, C. M. Lawson, G. M. Gray, *Appl. Phys. Lett*. **2004**, *84*, 5174-5176
82. O. J. Achadu, T. Nyokong, *Talanta* **2017**, *166*, 15-26.
83. O. J. Achadu, T. Nyokong, *New J. Chem*. **2016**, *40*, 8727-8736.
84. A. Atsay, A. Koça, M. B. Kocak, *Transition Met. Chem.* **2009**, *34*, 877-890.
85. E. M. Maya, A. W. Snow, J. S. Shirk, R. G. S. Pong, S. R. Flom, G. L. Roberts, *J. Mater. Chem*. **2003**, *13*, 1603-1613.

86. M. Kimura, K. Nakada, Y. Yamaguchi, K. Hanabusa, H. Shirai, N. Kobayashi, *Chem. Commun*. **1997**, 1215-1216.
87. R. Jasinski. *J. Electrochem. Soc*. **1965**, *112*, 526-528.
88. A. Kozawa, V. E. Zilionis, R. J. Brodd, *J. Electrochem. Soc*. **1970**, *117*, 1470-1474.
89. A. Kozawa, V. E. Zilionis, R. J. Brodd, *J. Electrochem. Soc*. **1970**, *117*, 1474-1478.
90. J.-P. Randin, *Electrochim. Acta* **1974**, *19*, 83-85.
91. J. Zagal, R. K. Sen, E. Yeager, *J. Electroanal. Chem*. **1977**, *83*, 207-213.
92. J. Zagal, P. Bindra, E. Yeager, *J. Electrochem. Soc.* **1980**, *127*, 1506-1517.
93. F. Van Den Brink, W. Visscher, E. Barendrecht, *J. Electroanal. Chem*. **1983**, *157*, 283-304.
94. F. Van Den Brink, W. Visscher, E. Barendrecht, *J. Electroanal. Chem*. **1983**, *157*, 305-318.
95. F. Van Den Brink, W. Visscher, E. Barendrecht, *J. Electroanal. Chem*. **1984**, *172*, 301-325.
96. F. Van Den Brink, W. Visscher, E. Barendrecht, *J. Electroanal. Chem*. **1984**, *175*, 279-289.
97. S. Bak, D. Kim, H. Lee, *Curr. Appl. Phys*. **2016**, *16*, 1192-1201.
98. S. Benítez-Martínez, M. Valcárcel, *Trends Anal. Chem.* **2015**, *72*, 93-113.
99. A.K. Geim, *Science* **2009**, *324*, 1530-1534.
100. M. Arvand, S. Hemmati, *Talanta* **2017**, *174*, 243-255.
101. F. Chena, W. Gaoc, X. Qiub, H. Zhang, L. Liu, P. Liao, W. Fue, Y. Luo, *Frontiers in Laboratory Medicine* **2017**, *1*, 192-199.
102. M. Zhang, L. Bai, W. Shang, W. Xie, H. Ma, Y. Fu, D. Fang, H. Sun, L. Fan, M. Han, C. Liu, S. Yang, *J. Mater. Chem*. **2012**, *22*, 7461-7467.
103. R. Ye, C. Xiang, J. Lin, Z. Peng, K. Huang, Z. Yan, N. P. Cook, E. L. Samuel, C. C. Hwang, G. Ruan, G. Ceriotti, A. R. Raji, A. A. Martí, J. M. Tour, *Nat. Commun*. **2013**, *4*, 1-6.
104. Y. Dong, H. Pang, S. Ren, C. Chen, Y. Chi, T. Yu, *Carbon* **2013**, *64*, 245-251.
105. L. Minati, S. Torrengo, D. Maniglio, C. Migliaresi, G. Speranza, *Mater. Chem. Phys*. **2012**, *137,* 12-16.
106. A. Ananthanarayanan, X. Wang, P. Routh, B. Sana, S. Lim, D. Kim, K. Lim, J. Li, P. Chen, *Adv. Funct. Mater*. **2014**, *24*, 3021-3026.
107. D.B. Shinde, V.K. Pillai, *Chem. Eur. J*. **2012**, *18*, 12522-12528.

108. Y. Li, Y. Hu, Y. Zhao, G. Shi, L. Deng, Y. Hou, *Adv. Mater*. **2011**, *23*, 776-780.
109. Y. Zhang, H. Gao, J. Niu, B. Liu, *New J. Chem*. **2014**, *38*, 4970-4974.
110. K. Habiba, V.I. Makarov, J. Avalos, M.J.F. Guinel, B.R. Weiner, G. Morell, *Carbon* **2013**, *64*, 341-350.
111. P. Russo, A. Hu, G. Compagnini, W. Duleydan, N.Y. Zhou, *Nanoscale* **2014**, *6*, 2381-2389.
112. X. Yan, X. Cui, B. Li, L. S. Li, *Nano Lett*. **2010**, *10*, 1869-1973.
113. R. Liu, D. Wu, X. Feng, K. Mullen, *J. Am. Chem. Soc*. **2011**, *133*, 15221-15223.
114. R. Gokhale, P. Singh, *Part. Part. Syst. Charact*. **2014**, *31*, 433-438.
115. J. Drbohlavova ,V. Adam, R. Kizek, J. Hubalek, *Int. J. Mol. Sci.* **2009**, *10*, 656-673.
116. C. Zhang, N. Mahmood, H. Yin, F. Liu, Y. Hou, *Adv. Mater.* **2013**, *25*, 4932-4937.
117. T. V. Tam, S. G. Kang, K. F. Babu, E. Oh, S. G. Lee, W. M. Choi, *J. Mater. Chem. A* **2017**, *5*, 10537-10543.
118. R. Vinoth, I. M. Patil, A. Pandikumar, B. A. Kakade, N. M.Huang, D. D. Dionysios, B. Neppolian, *ACS Omega*, **2016**, *1*, 971-980.
119. P. Ayala, R. Arenal, M. Rümmeli, A. Rubio, T. Pichler, *Carbon* **2010**, *48*, 575-586.
120. Q. Li, S. Zhang, L. Dai, L. Li, *J. Am. Chem. Soc*. **2012**, *134*, 18932-18935.
121. S. Bag, C. R. Raj, *J. Chem. Scie*. **2016**, *128*, 339-347.
122. Y. Zhang, C. Wu, X. Zhou, X. Wu, Y. Yang, H. Wu, S. Guo, J. Zhang, *Nanoscale* **2013**, *5*, 1816-1819.
123. H. Razmi, R. Mohammad-Rezaei, *Biosens. Bioelectron*. **2013**, *41*, 498-504.
124. L. Li, D. Liu, K. Wang, H. Mao, T. You, *Sens. Actuators B* **2017**, *252*, 17-23.
125. G. G. Matlou, D. O. Oluwole, E. Prinsloo, T. Nyokong, *J. Photochem. Photobiol. B*. **2018**, *186*, 216-224.
126. S. Mapukata, F. Chindeka, K. E. Sekhosana, T. Nyokong, *J. Mol. Cat. A: Chem* **2017**, *439*, 211-223.
127. J. Wang, Y. Zhang, J. Ye, Z. Jiang, *Luminescence* **2017**, *32*, 573-580.
128. S. Paulo, E. Palomares, E. Martinez-Ferrero, *Nanomaterials* **2016**, *6*, 157-176.
129. Z. Keivani, M. Shabani-Nooshabadi, H. Karimi-Maleh, *J. Colloid Interface Sci*. **2017**, *507*, 11-17.
130. S. A. Omar, E. Artime, A. J. Webb, *Nitric Oxide* **2012**, *26*, 229-240.

131. S. A. Omar, A. J. Webb , J. O. Lundberg,E. Weitzberg, *J. Intern. Med*. **2015**, *279*, 315-336.
132. T. Kean, J.H. Miller, G. G. Skellern, D. Snodin, *Pharmeur. Sci. Notes* **2006**, *2*, 23-33.
133. X. Song, L. Gao, Y. Li, L. Mao, J. Yang, *Anal. Methods* **2017**, *9*, 3166-3171.
134. W. J. Santos, A. L. Sousa, R. C. Luz, R. C. Luz, F. S. Damos, L. T. Kubota, A. A. Tanaka, S. M. Tanaka, *Talanta* **2006**, *70*, 588-594.
135. O. J. Achadu, T. Nyokong, *J. Fluoresc*. **2016**, *26*, 283-295.
136. M. Shehab, S. Ebrahim, M. Soliman, *J. Lumin*. **2017**, *184*, 110-116.
137. J. Liu, X. Zhang, Z. Cong, Z. Chen, H. Yang, G. Chen, *Nanoscale* **2013**, *5*, 1810-1815.
138. S. D'Souza, E. Antunes, C. Litwinski, T. Nyokong, *J. Photochem. Photobiol. A* **2011**, *220*, 11-19.
139. X. Zhang, L. Mao, D. Zhang, L. Zhang, *J. Mol. Struct*. **2012**, *1022*, 153-158.
140. J. G. Young, W. Onyebuagu, *J. Organomet. Chem*. **1990**, *55*, 2155-2159.
141. X. Xu, F. Gao, X. Bai, F. Liu, W. Kong, M. Li, *Materials* **2017**, *10*, 1328-1337.
142. Y. Luo, M. Li, L. Sun, Y. Xu, G. Hu, T. Tang, J. Wen, X. Li, *J. Nanopart. Res*. **2017**, *19*, 363-371.
143. P. Tian, L. Tang, K. S. Teng, S. P. Lau, *Mater. Today* **2018**, *10*, 221-258.
144. Q. Yang, Z. Wang, J. Weng, *Soft Matter* **2012**, *8*, 9855-9863.
145. C. Brolly, J. Parnell, S. Bowden, *Planet. Space Sci*. **2016**, *121*, 53-59.
146. D. Pan, J. Zhang, Z. Li, M. Wu, *Adv. Mater*. **2010**, *22*, 734-738.
147. L. Tang, R. Ji, X. Cao, J. Lin, H. Jiang, X. Li, K. S. Teng, C. M. Luk, S. Zeng, J. Hao, S. P. Lau, *ACS Nano* **2012**, *6*, 5102-5110.
148. B. Manoj, A.G. Kunjomana, *Int. J. Electrochem. Sci*. **2012**, *7*, 3127-3134.
149. A. B. Siddique, A. K. Pramanick, S. Chatterjee, M. Ray, *Sci. Rep*. **2018**, *8*, 9770-9779.
150. O. M. Bankole, O. J. Achadu, T. Nyokong, *J. Fluoresc*. **2017**, *27*, 755-766.
151. J. Rusanova, M. Pilkington, S. Decurtins, *Chem. Comm*. **2002**, *19,* 2236-2237.
152. L. Li, J. F. Zhao, N. Won, H. Jin, S. Kim, J. Y. Chen, *Nanoscale Res. Lett*. **2012**, *7*, 386-393.
153. X.F. Zhang, X. Shao, *J. Photochem. Photobiol. A* **2014**, *278*, 69-74.
154. M. J. Stillman, T. Nyokong in: *Phthalocyanines - Properties and Applications*, edited by A. B. P. Lever, C. C. Leznoff, VCH, **1989**, New York.
155. Z. D. Liu, H. X. Zhao, C. Z. Huang, *PLoS ONE* **2012**, *7*, e50367.

156. M. H. V. Reddy, R. M. Al-Shammari, N. Al-Attar, S. Lopez, T. E. Keyes, J. H. Rice, *Proc. SPIE* **2014**, *9172* doi: 10.1117/12.2061951.

157. O. Bajjou, M. Khenfouch, M. Baïtoul, B. Mothudi, M. Dhlamini, E. Faulques, M. Maaza, *IOP Conf. Ser.: Mater. Sci. Eng*. **2017**, 186, 012003.

158. O. Frank, M. Bouša, I. Riaz, R. Jalil, K. S. Novoselov, G. Tsoukleri, J. Parthenios, L. Kavan, K. Papagelis, C. Galiotis, *Nano Lett*. **2012**, *12*, 687-693.

159. T. G. Souza, V. S. Ciminelli, N. D. Mohallem, *J. Phys. Conf. Ser.* **2016,** *733*, 12039-12044.

160. F. J. Rawson, A, J. Downard, K. H. Baronian, *Sci. Rep*. **2014**, *4*, 5216-5224.

161. R. L. McCreery, *Chem. Rev*. **2008**, *108*, 2646-2687.

162. A. Sivanesan, S. A. John, *Electrochim. Acta* **2009**, *54*, 7458-7463.

163. A. Salimi, K. Abdi, *Talanta* **2004**, *63*, 475-483.

164. J. Zhang in: *PEM Fuel Cell Electrocatalysts and Catalyst Layers*, Springer-Verlag, **2008**, London.

165. T. Shinagawa, A.T. Garcia-Esparza, K. Takanabe, *Sci. Rep.* **2015**, *5*, 1-21.

166. J. M. Zen, A. S. Kumar, M.R. Chang, *Electrochim. Acta* **2000**, *45*, 1691-1699.

167. X. Gu, X. Li, S. Wu, J. Shi, G. Jiang, G. Jiang, S. Tian*, RSC Adv*. **2016**, *6*, 8070-8078.

168. X. Song, L. Gao, Y. Li, L. Maoa, J. Yang, *Anal. Methods*, **2017**, *9*, 3166 -3171.

169. A. A. Saeed, B. Singh, M. N. Abbas, Y. M. Issa, E. Dempsey, *Electroanalysis* **2015,** *27*, 1086-1096.

170. C. W. Foster, J. Pillay, J. P. Metters, C. E. Banks, *Sensors* **2014**, *14*, 21905-21922.

171. F. Matemadombo, T. Nyokong, *Electrochim. Acta* **2007**, *52*, 6856-6864.

172. N. R. Vettorazzi, L. Sereno, M. Katoh, M. Ota, L. Otero, *J. Electrochem. Soc.* **2008**, *155*, 110-115.

173. K. Bramhaiah, I. Pandey, V. N. Singh, C. Kavitha, N. S. John*, J. Nanopart. Res*. **2018**, *20*, 56-68.

174. S. Karim Hassaninejad-Darzi, F. Shajie, *J. Braz. Chem. Soc.* **2017**, *28*, 529-539.

175. S. N. Azizi, S. Ghasemi, E. Chiani, *Electrochim. Acta* **2013**, *88*, 463-472.
176. L. L. Okumura, A. A. Saczk, M. F. de Oliveira, A. C. C. Fulgêncio, L. Torrezani, P. E. N. Gomesa, R. M. Peixoto, *J. Braz. Chem. Soc.* **2011**, *22*, 652-659.
177. J. H. Zagal, S. Lira,S. Ureta-Zañartu, J. *Electroanal. Chem*. **1986**, *210*, 95-110.
178. D. A. Venegas-Yazigi, G. I. Cárdenas-Jirón, J. H. Zagal, *J. Coord. Chem*. **2003**, *56*, 1269-1275.
179. C. S. J. N. O'Donoghue, M. Shumba, T. Nyokong, *Electroanalysis* **2017**, *29*, 1731-1740.
180. C. D. Conceição, R. C. Faria, O. Fatibello-Filho, A. A. Tanaka, *Anal. Lett*. **2008**, *41*, 1010-1021.

Appendices

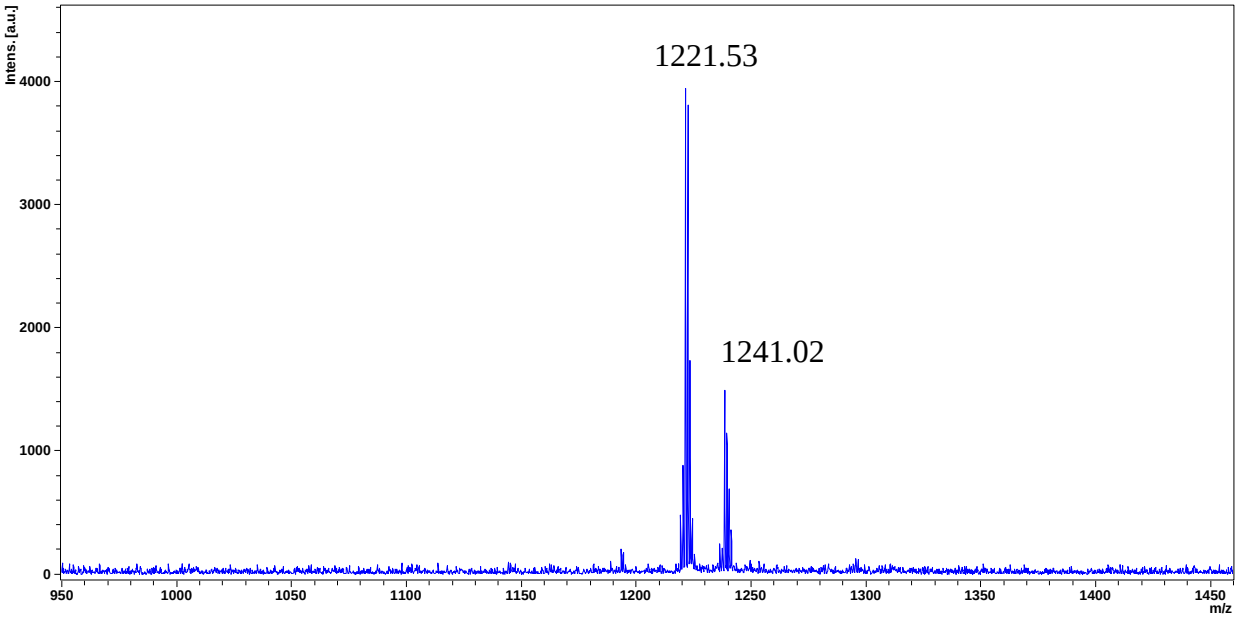

Fig. A1: Mass spectrum of complex **2**.

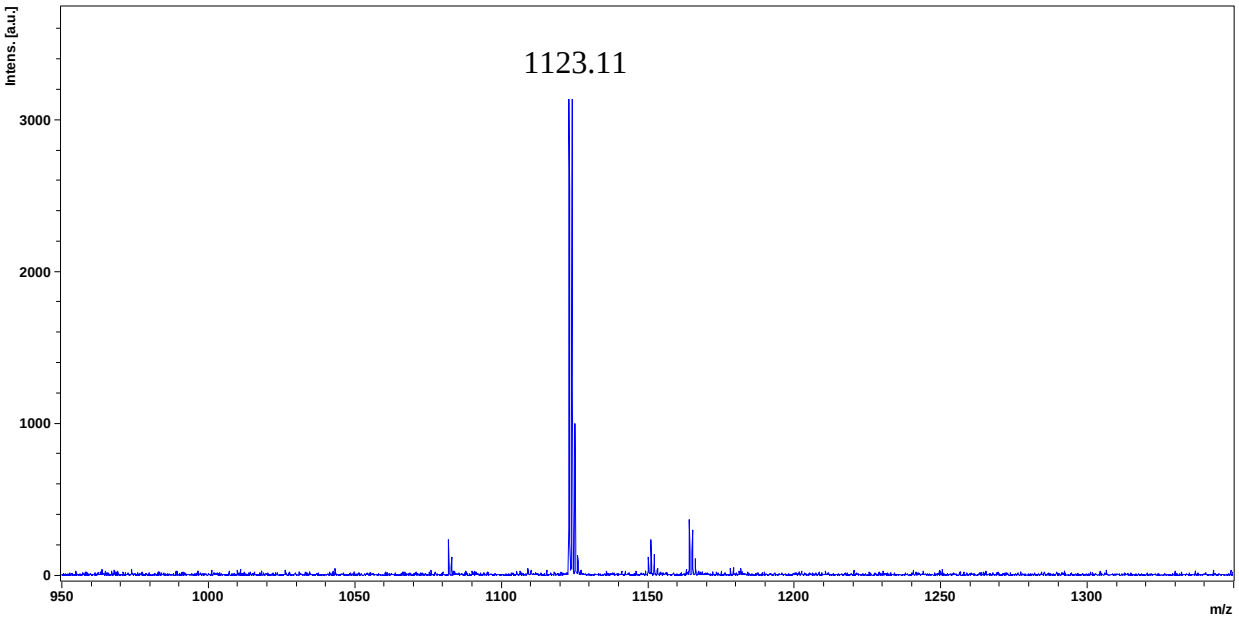

Fig. A2: Mass spectrum of complex **4**.

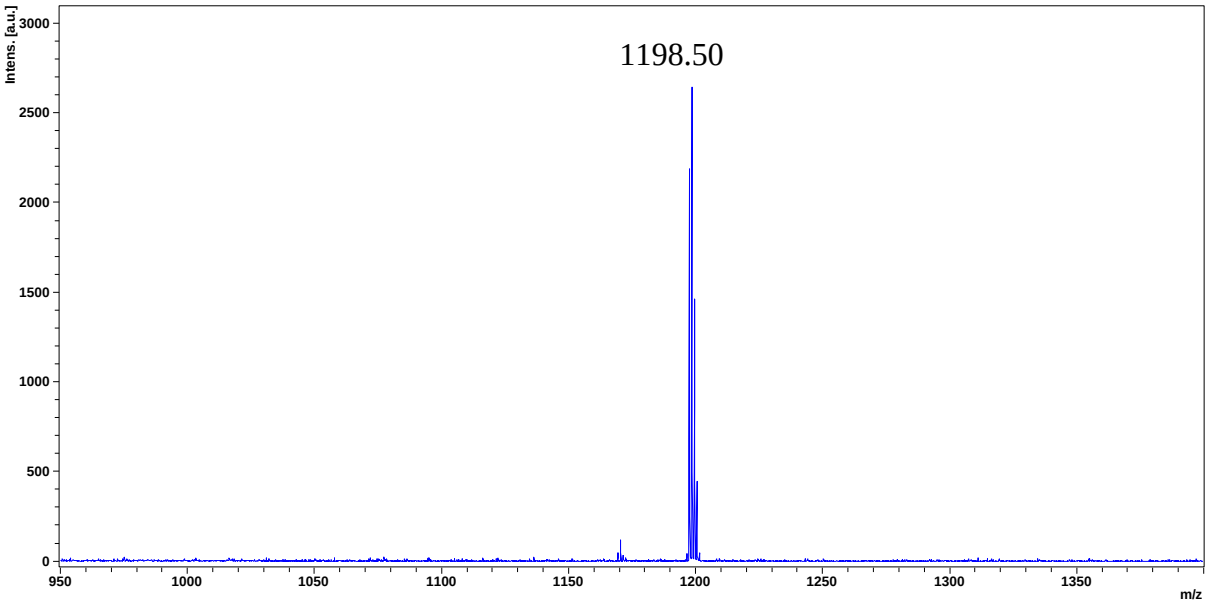

Fig. A3: Mass spectrum of complex **5**.

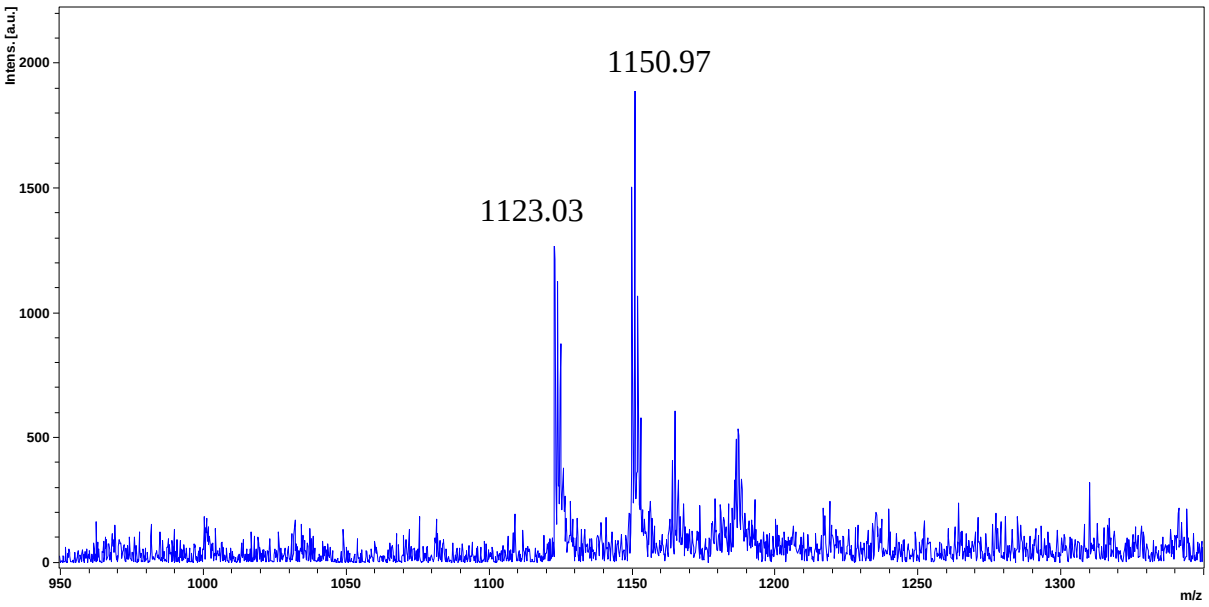

Fig. A4: Mass spectrum of complex **6**.

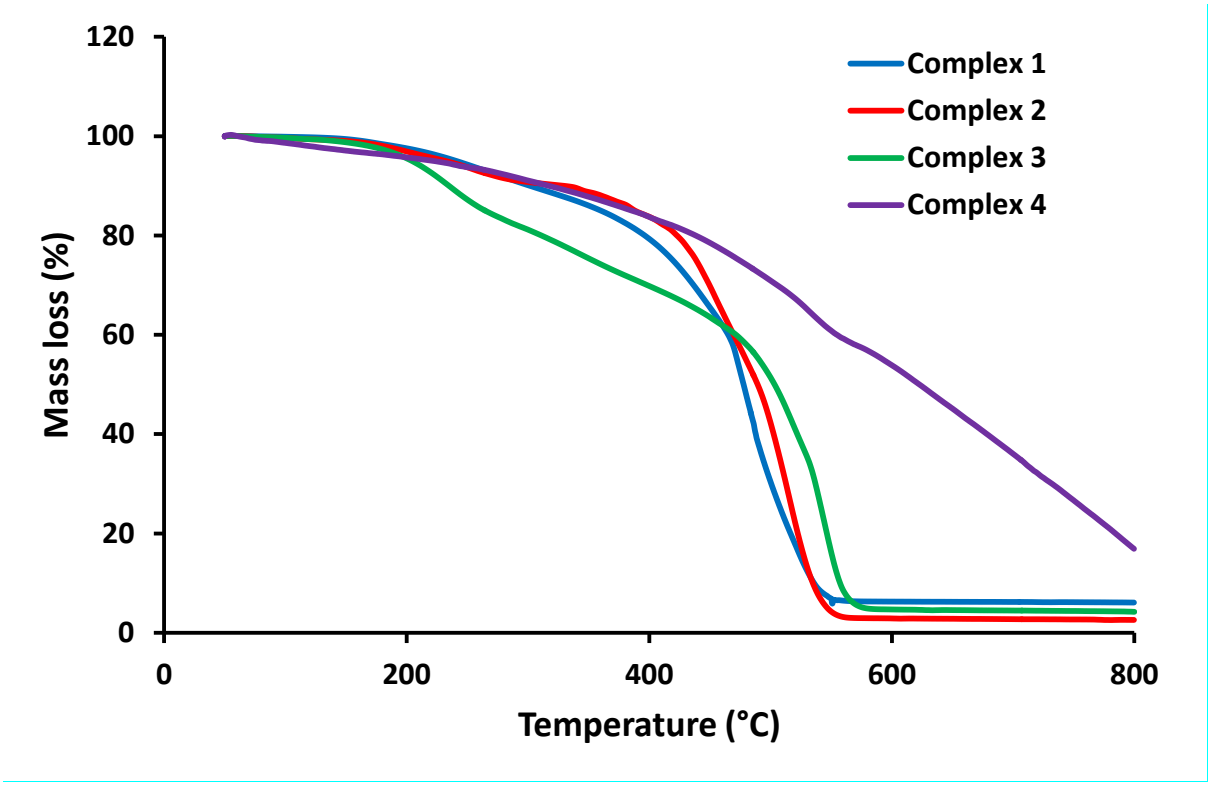

Fig. A5: Thermograms of complexes **1**-**4**.